

Diapycnal mixing in the subpolar North Atlantic

Mingming Li

Institute of Environmental Physics,
University of Bremen

Diapycnal mixing in the subpolar North Atlantic

Dissertation
zur Erlangung des akademischen Grades
Doktor der Naturwissenschaften (Dr. rer. nat.)

von

M. Sc. Mingming Li
aus Shandong, China

-
1. Gutachterin: Prof. Monika Rhein
 2. Gutachter: Prof. Richard J. Greatbatch

Eingereicht am: 16.09.2013
Tag des Promotionskolloquiums: 16.10.2013

Abstract

Model simulations of climate change and global overturning circulation are quite sensitive to the strength and distribution of mixing. However, the field observations are only sparsely available. The strength of diapycnal mixing was estimated from more than 700 profiles of hydrographic and velocity measurements in the subpolar North Atlantic (SPNA). These measurements were collected during hydrographic surveys from 2003 to 2011, ranging from 40°N to 62°N. Furthermore, 28 Micro-scale structure profiles were collected at 7 stations over the Mid-Atlantic Ridge and at the western boundary during the cruise in 2008, providing supplement of direct measurements and an agent to evaluate the overall estimation. Under the assumption of a steady state, spatial distribution and vertical structure of diapycnal diffusivity K_ρ were mapped in this area.

The inferred diffusivity is generally elevated compared to the background diffusivity in the open ocean ($O(10^{-5} \text{ m}^2 \text{ s}^{-1})$) and shows large variability in the SPNA. K_ρ larger than $10^{-4} \text{ m}^2 \text{ s}^{-1}$ can be seen nearly in the whole area several hundred of meters within seafloor. Strong mixing at mid-depth of one to two orders larger than the background value are found at western boundary, over Mid-Atlantic ridge and in the pathway of North Atlantic Current and deep currents. The possible connections between enhanced mixing and several environmental parameters including seafloor roughness, geostrophic currents and meso-scale eddies are analysed. Conversions between components of the North Atlantic Deep Water associated with mixing are estimated from vertical motion inferred from density field and turbulent diffusivity based on an advection-diffusion balance model. In vertical direction, averaged K_ρ is found to decrease with the height above seafloor within the deepest 1500 m and to

be constant with a value close to $10^{-4} \text{ m}^2 \text{ s}^{-1}$.

A transformation of around 1.6 Sv ($10^6 \text{ m}^3 \text{ s}^{-1}$) from Gibbs Fracture Zone Water to overlying Labrador Sea water is derived; the transformation between lowest Denmark Strait Overflow Water to upper Gibbs Fracture Zone Water is about 3.5 Sv.

Contents

1	Introduction	1
1.1	The Meridional Overturning Circulation	2
1.2	Circulation in the North Atlantic	5
1.3	Strength of diapycnal mixing	9
2	Theory	12
2.1	Energy balance and diffusivity	12
2.2	Advection-diffusion balance	16
2.3	Internal wave and energy cascade	18
3	Data and Method	23
3.1	Data	23
3.2	Method	27
3.2.1	Fine-scale parameterization	27
3.2.2	Spectra	31
3.2.3	Shear/strain variance ratio	35
3.2.4	Micro-scale structure profiling	37
3.3	Errors and uncertainties	42
3.3.1	Pre-process of ADCP data and instrument noise	42
3.3.2	Error propagation	44
3.3.3	Bootstrap method	45
4	Observations	47
4.1	Estimations of diapycnal diffusivity	47
4.2	Structures of diffusivity in 2 vertical sections	53
4.3	Horizontal distribution of diffusivity	56

CONTENTS

5	Discussion	61
5.1	Distribution of diffusivities	61
5.2	Possible mechanisms of the enhanced mixing	62
5.2.1	Rough topography	62
5.2.2	Geostrophic currents	66
5.2.3	Eddies	68
5.3	Vertical structure of K_ρ and shear/strain variance ratio	72
5.4	Transformation between water masses	77
6	Summary and outlook	79
	Bibliography	81

Chapter 1

Introduction

Turbulent mixing in the ocean has been a focus of oceanographic research for a couple of decades. Breaking of internal waves leads to turbulence and mixing that modifies water masses, maintains the ocean stratification, and supports the existence of the global overturning Circulation (MOC). Ocean circulation models show a sensitivity of the MOC to strength and location of mixing (e.g. Simmons *et al.*, 2004; Saenko and collaborators (2005, 2006, 2012); Jayne, 2009).

As one of the major locations of deep water formation, the northern North Atlantic receives increasing attention in the field research. Inverse box modeling of water mass conversion rates show significant diapycnal volume fluxes of several Sverdrup ($10^6 \text{ m}^3 \text{ s}^{-1}$) in the deep subpolar North Atlantic (Lumpkin *et al.*, 2008). The magnitude of the fluxes relies on the implementation of diapycnal mixing, which is not well known on basin scales a priori. First attempts to compile large-scale distributions of turbulent diffusivities have been made by, e.g., Walter *et al.* (2005) for parts of the North Atlantic, and Kunze *et al.* (2006) on WOCE lines (World Ocean Circulation Experiment, <http://www.nodc.noaa.gov/WOCE/>). A subpolar North Atlantic observing system is operated by the Oceanography department of the Bremen University with long term measurements since 1997. In the last decade, several hydrographic cruises were carried out with in situ observations of currents and hydrography. Analysis of this dataset of the whole subpolar North Atlantic made it possible to draw a map of mixing strength, deepen the understanding

of the water mass formation and transformation, contribute to the closure of ocean circulation and model studies involving the climate and ocean system.

1.1 The Meridional Overturning Circulation

The global ocean circulation is defined as the transport of water driven by density gradients created by surface heat and freshwater fluxes as well as by wind and tidal forcing (Wunsch, 2002). In former days the heat and freshwater flux driven circulation was called “Thermohaline Circulation”, with the term thermo- referring to temperature and -haline referring to salt content, which together determine the density of sea water. However, the flow driven by the wind field is less likely to be separated from the system, therefore the more appropriate term “Meridional Overturning Circulation” emerged and was getting more and more widely accepted and used by oceanographers. There is no doubt that the upper ocean circulation is driven by wind stress (the force per unit area exerted on the ocean surface), while the buoyancy plays an important role in the abyssal ocean; furthermore, ocean currents due to tides are also significant in many places, not only prominent in shallow coastal areas but also important in the deep ocean. A general sketch of the mechanisms and processes of circulation is made in Fig. 1.1 based on former illustrators and literatures (e.g. Stommel, 1958; Gordon, 1991; Speer *et al.*, 2000; Garrett, 2003a,b; Kuhlbrodt *et al.*, 2007; Stöber, 2009). The shown two-dimensional North-South vertical section mainly displays the situation along the western boundary of Atlantic Ocean.

In polar and subpolar regions, seawater at the surface loses heat to the atmosphere and thus is intensely cooled; furthermore, exceeding of evaporation to precipitation leads to an increase of salinity. The losses of heat and freshwater consequently result in an increase in density. The dense water sinks into deep basins and forms the deep or bottom water. This process occurs only in specific areas of the North Atlantic (see section 1.2 for details) and the Southern Ocean: the North Atlantic Deep Water (NADW) in the northern North Atlantic and Antarctic Bottom Water (AABW) formed at various sites

1. INTRODUCTION

on the continental shelf of Antarctic (principally in the Weddell Sea, Dickson and Brown, 1994).

These deep and bottom waters sink into the abyssal ocean and are carried equatorward by a system of deep boundary currents (Stommel, 1957). According to observations, the salty NADW moves southward across the equator to enter the intermediate layer of the Southern Ocean. A tongue of fresh Antarctic Intermediate Water (AAIW) penetrates to the northern hemisphere (see Fig. 1.1).

At low and middle latitudes, heat transfers downward across the thermocline / pycnocline, decreases the density of cold deep waters, allowing them to upwell into the upper ocean.

The circulation consists of poleward flow of warm surface water, deep water formation and flow of cold water at depth. According to Sandström's theorem for a fluid heated and cooled at the surface, if there were no additional processes, the dense cold water would fill up the basin and the circulation would be convectively driven and confined in a very shallow layer (Munk and Wunsch, 1998). However, the ocean is stratified with an obvious pycnocline stretching several hundreds of meters in the vertical direction. That is mainly because of the process of deep mixing besides lateral advection, or specifically, the diapycnal mixing which is the small-scale process allowing the downward transfer of heat.

Diapycnal mixing plays a crucial role in the dynamics of the MOC, since the strength of MOC is substantially related to the distribution and intensity of ocean mixing; and of the climate system, while diapycnal mixing transports properties related to climate. Based on studies of ocean circulation models, the meridional overturning rate was found to increase with the enhancement of mixing for a uniform mixing rate (Bryan 1987), and Marotzke (1997) further suggested that the meridional overturning strength is proportional to $K_\rho^{2/3}$. Prange *et al.* (2003) examined this exponential relation with a three-dimensional global ocean general circulation model (OGCM) and affirmed the

used more currently rather than “dianeutral”.

1.2 Circulation in the North Atlantic

The formation and spreading of North Atlantic Deep water is a major component of the global overturning circulation. It plays an important role in the balances of heat and volume of the MOC. At the same time, the northward transport and modification of warm and saline water influences the European climate, and more generally, the global climate system.

- *Surface drift*

In the North Atlantic, warm and saline tropic / subtropic water is transported by the Gulf Stream into the mid-latitude (see Fig. 1.2). At about 40°N, it splits in two: the southern stream turns southeast after passing 50°W and the northern stream turns north to become the strong warm current, which with its continuation is referred as the North Atlantic Current (NAC, Mann, 1967). The NAC flows northward offshore of the east side of the Grand Banks and is separated into several branches. Part of it turns to the east and then recirculates southward at around 50°N at both the western and eastern sides of Mid-Atlantic Ridge (MAR); the major part flows to the northwest towards the Labrador Sea, and turns sharply to the southeast at about 53°N, across the MAR into the eastern Atlantic. After that, part of it flows into the Nordic Seas, while most of the water turns to the west, forming the anticlockwise subpolar gyre (Rossby, 1996; Rhein *et al.*, 2011). The heat loss to the polar/subpolar atmosphere contributes to the relatively warm European climate (Rhines *et al.*, 2008), and buoyancy loss of surface water along the pathway of NAC leads to the formation of deep water, particularly in the Labrador Sea.

- *Deep water formation*

The NADW comprises three major water masses. The uppermost one, the Labrador Sea Water (LSW), is formed in the Labrador Sea by deep convection. The LSW can be distinguished into two modes: the upper LSW (uLSW, occupying the potential density range of $\sigma_\theta = 27.68 - 27.74 \text{ kg m}^{-3}$) is the product of the shallow convection observed since 1997 reaching depth of 1000 - 1500 m; the dense mode, or classical LSW, (sometimes called “deep” LSW, $\sigma_\theta = 27.74 - 27.80 \text{ kg m}^{-3}$) is the product of the intense convection of the early 1990s and reaching down to 2000m (e.g. Rhein *et al.*, 2002; Kieke *et al.*, 2006; Kieke *et al.*, 2007; Rhein *et al.*, 2011). Some of LSW spreads rapidly from the formation region to the northeast into the Irminger Sea; some part spreads southeastward with the deep western boundary current (DWBC), and part of it turns north and east at about 50°N and then turns eastward, flows across the Mid-Atlantic Ridge into the east basin (Talley and McCartney, 1982; Rhein *et al.*, 2002. Fig. 1.2). The middle NADW, Gibbs Fracture Zone Water (GFZW, $\sigma_\theta = 27.80 - 27.88 \text{ kg m}^{-3}$), originates from the Norwegian Sea, and then leaves the basin between Iceland and Scotland (so the water mass is also named as Iceland-Scotland Overflow Water, ISOW). While flowing southward it entrains local warm and saline Atlantic waters (much saltier than the overflow itself) and the Labrador Sea Water. Thus GFZW is marked by a salinity maximum. It spreads southward at the eastern flank of the Mid-Atlantic Ridge and enters the subpolar gyre, but part of the water passes the Charlie-Gibbs Fracture Zone and spreads northward to the Irminger Sea and then flows westward entering the DWBC (Dickson and Brown, 1994; Stramma *et al.*, 2004). It arranges in the DWBC between 2500 and 3500 m. The deepest component is the Denmark Strait Overflow Water (DSOW, $\sigma_\theta > 27.80 \text{ kg m}^{-3}$). It forms from the recirculated Atlantic Water exiting from the Arctic Ocean and mixtures of convection in the Iceland and Greenland Seas. It spreads southward and sinks to the bottom after passing the Denmark Strait. It flows along Greenland and enters the Labrador Sea as a deep boundary current after encountering the GFZW (Stramma *et al.*, 2004). It is cold and less saline than GFZW, flowing below 3500 m in the DWBC and spreading into the deep Atlantic basins (Dickson and Brown, 1994).

• *Transport southward/deep current*

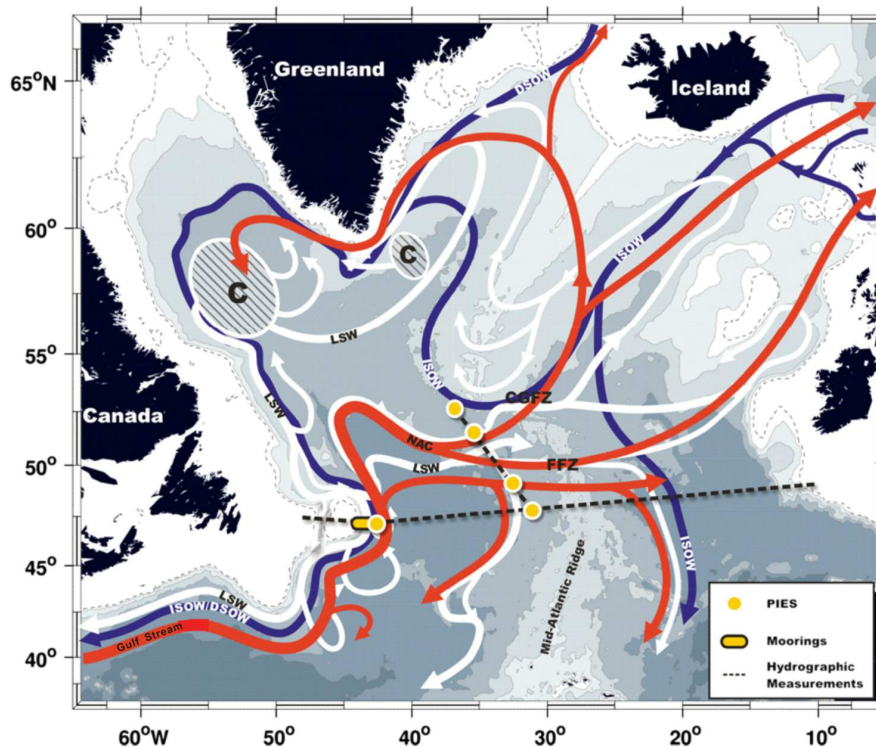


Figure 1.2: Major currents in the subpolar North Atlantic; red arrows indicate the surface current NAC (North Atlantic Current), blue ones the pathway of ISOW (Island-Scotland Overflow Water) or/and DSOW (Denmark Strait Overflow Water), white ones the pathway of LSW (Labrador Sea Water). Taken from Rhein *et al.* (2011).

A large fraction of deep water generated in polar regions is carried down the western boundaries in a Deep Western Boundary Current (DWBC). All components of deep waters are carried and modified in the DWBC, forming part of the cold limb of the meridional circulation (e.g. Stramma *et al.*, 2004; Rhein *et al.*, 2011). The DWBC leaves the Labrador Sea and flows southward passing through Flemish Pass or around Flemish Cap (Schott *et al.*, 2004, inshore of NAC), where it interacts with the NAC and underlies complicated topography thus the properties of deep water are modified. It flows to the west south of the Grand Banks and continues southward along continental slope to the Southern Atlantic. In addition to the DWBC, interior southward pathways of LSW starting at the southeast corner of Flemish Cap were also found through

1. INTRODUCTION

float observations (Bawer *et al.*, 2009). It takes around 50 years for the NADW to reach the Southern Ocean (Sun and Bleck, 2001). However, part of the deep water is entrained and circulates in the subpolar gyre. When passing the north of Flemish Cap, LSW outflow splits into different routes. Some of it stays in the DWBC to the south, some flows east across the Charlie Gibbs Fracture Zone (Rhein *et al.*, 2002) and recirculates in the subpolar region.

1.3 Strength of diapycnal mixing

Most of the turbulence and mixing is caused by an overturning instability with maximum vertical scale of 1-100 m, typically. Mixing takes place at scales of 1mm to 1m (Munk and Wunsch, 1998), therefore it is not easy to measure the overall mixing directly. There are two predominant ways to quantify mixing in the ocean: (1) through large scale balances of mass, heat and salt, for instance, with the advection-diffusion balance model used by Munk (1966); (2) through the consideration of global energy balance. They are explicated more detailed in sections 2.2 and 2.1, respectively.

After the proposition of the theoretical global average diffusivity $K_\rho = 10^{-4} \text{ m}^2 \text{ s}^{-1}$ by Munk (1966, details are referred to Section 2.2) with assumption of uniform upwelling, numerous observations were carried out with direct microstructure measurements, tracer-release observations, and indirect finescale estimates. With microstructure and tracer release measurements (e.g. Polzin *et al.* 1997), the diapycnal diffusivity in the upper ocean and thermocline was ascertained to be $10^{-5} \text{ m}^2 \text{ s}^{-1}$, an order of magnitude lower than the inferred abyssal-recipes value (e.g. Osborn and Cox, 1972; Munk, 1981; Moum and Osborn, 1986; Gregg, 1987; Toole *et al.*, 1994; Ledwell *et al.*, 1993). It appears that the advection-diffusion balance fails in the upper ocean, which was originally proposed to model the mixing in the abyssal ocean (see Section 2.2). To overcome the technical limitations, the indirect method of inferring eddy diffusivity from vertical shear of horizontal velocity via fine-scale measurements emerged and developed during the last decades. Deviating from the canonical value of Munk (1966), observations have shown smaller values of $K_\rho \sim O(10^{-5}) \text{ m}^2 \text{ s}^{-1}$ in ocean interior and throughout the full depth over smooth abyssal plains (Kunze and Sanford, 1996). The values seem too small to maintain the observed stratification in the deep ocean. However, the spatial distribution of turbulent diapycnal mixing in the deep ocean was found to be strongly localized, with enhanced mixing of 1-2 magnitude larger or even of $O(10^{-1})$ detected in specific areas. As argued by researchers, stronger mixing must exist in confined areas to elevate the average diffusion to maintain the

stratification and overturning circulation. These locations include boundary regions (e.g. Pickard *et al.*, 1989; Walter *et al.*, 2005; Nash *et al.*, 2007; Lauderdale *et al.*, 2008; Stöber *et al.*, 2008), above rough topography (e.g. Polzin *et al.*, 1997; Ledwell *et al.*, 2000), near intensified flow such as western boundary current (e.g. Pickart *et al.*, 1989; Pelegri and Csanady, 1994; Wunsch and Ferrari, 2004), in regions of internal tide generation (e.g. Kunze and Toole, 1997; Polzin *et al.*, 1997; Ledwell *et al.*, 2000; Kunze *et al.*, 2002, 2006). The eddy energy scattered into high-wavenumber internal waves is also supposed to be an important cause of the enhanced diapycnal mixing (e.g. Marshall *et al.*, 2002; Zhai *et al.*, 2010; Saenko *et al.*, 2012). The dependence of K_ρ on latitude was also well studied (e.g. Garrett, 2003; Hibiya and Nagasawa, 2004; Hibiya *et al.*, 2007); moreover, the vertical structure of diapycnal mixing are another important topic since the numerical models are very sensitive to it. It is found that the depth dependence of mixing varies from place to place and is even different in the same study region.

With the carrying out of worldwide measurements, for instance the World Ocean Circulation Experiment (WOCE) and the Argo floats program, global mapping of diapycnal mixing became possible. Researchers made such a map of spatial distribution of diapycnal mixing separately (e.g. Kunze *et al.* (2006); Wu *et al.* (2011); Whalen *et al.* (2012)), inferred from the fine-scale parameterization of shear or strain or both. Still, the estimates are sparse (hydrographic surveys with ship-track measurements) or restricted by the observation range of floats to the upper ocean, more measurements and analysis are needed.

This study aims to provide a detailed view of the diapycnal mixing in the subpolar North Atlantic (mainly at 42°N - 62°N), ranging from Labrador Sea, Newfoundland Basin, crossing the Mid-Atlantic Ridge to the eastern basin. Records of properties of water and currents collected during nine hydrographic cruises in the last decade are analysed to infer the turbulent diffusivity. Theoretical background of internal wave and mixing are displayed in Chapter 2. Measurements and method used in this study are introduced in Chapter 3. This study is mainly based on the shear parameterization, with direct microstructure measurements at several stations analysed to qualify its appli-

1. INTRODUCTION

cability in topography varying and current intensified regions. Intermediary analysis results and the spatial distribution of diffusivity are presented in Chapter 4. The possible mechanisms of the spatial variability of K_ρ are discussed in Chapter 5. The last chapter contains a summary of this study and outlook for future work.

Chapter 2

Theory

The energy supporting the turbulent mixing mainly comes from the breaking of internal waves. Comprehensions of the property of internal wave field and energy transfer are essential to understand the method of diapycnal diffusivity estimation.

2.1 Energy balance and diffusivity

Applying the Reynolds decomposition, the instantaneous velocity \tilde{u}_i is split in two parts, mean flow U_i and fluctuating part (perturbation) u_i , $\tilde{u}_i = U_i + u_i$, where $i = 1, 2, 3$ represents the east, north and upward components in Cartesian coordinates. Turbulent kinetic energy (TKE) is defined as the mean kinetic energy per unit mass associated with eddies in turbulent flow. Physically, the turbulent kinetic energy is characterised by root-mean-square (RMS) velocity fluctuations.

$$E = \frac{1}{2} \langle u_i u_i \rangle = \frac{1}{2} [\langle u_1^2 \rangle + \langle u_2^2 \rangle + \langle u_3^2 \rangle] \quad (2.1)$$

here $\langle \rangle$ indicates the temporal mean.

Pressure and density can also be decomposed in the same way as velocity, so that $\tilde{p} = P + p$ and $\tilde{\rho} = \rho + \rho'$. Substituting \tilde{u}_i , \tilde{p} and $\tilde{\rho}$ into the Navier

2. THEORY

Stokes equation and subtracting the averaged motion yields an equation for the fluctuation as:

$$\begin{aligned}
\frac{\partial}{\partial t} \langle u_i u_k \rangle + U_j \frac{\partial}{\partial x_j} \langle u_i u_k \rangle &= - \left\langle \frac{p}{\rho} \left[\frac{\partial u_i}{\partial x_k} + \frac{\partial u_i}{\partial x_k} \right] \right\rangle \\
&+ \frac{\partial}{\partial x_j} \left\{ - [\langle p u_k \rangle \delta_{ij} + \langle p u_i \rangle \delta_{kj}] - \langle u_i u_k u_j \rangle + 2\nu [\langle s_{ij} u_k \rangle + \langle s_{ij} u_k \rangle] \right\} \\
&- \left[\langle u_i u_j \rangle \frac{\partial U_k}{\partial x_j} + \langle u_k u_j \rangle \frac{\partial U_i}{\partial x_j} \right] - 2\nu \left[\langle s_{ij} \frac{\partial u_k}{\partial x_j} \rangle + \langle s_{kj} \frac{\partial u_i}{\partial x_j} \rangle \right] - \frac{g}{\rho} \langle u_i \rho' \rangle \delta_{i3}
\end{aligned} \tag{2.2}$$

This is the so-called Reynold stress equation. Here $\langle u_i u_j \rangle$ is the component of Reynold stress, δ_{ij} the Kronecker delta, ν the kinetic viscosity, s_{ij} the fluctuating strain rate, defined by:

$$s_{ij} = \frac{1}{2} \left[\frac{\partial u_i}{\partial x_j} + \frac{\partial u_j}{\partial x_i} \right]$$

Note that in the incompressibility condition $\partial U_j / \partial x_j = 0$, and the mean deformation rate tensor $\partial U_i / \partial x_j$ can be decomposed into its symmetric and antisymmetric parts:

$$\frac{\partial U_i}{\partial x_j} = S_{ij} + \Omega_{ij} = \frac{1}{2} \left[\frac{\partial U_i}{\partial x_j} + \frac{\partial U_j}{\partial x_i} \right] + \frac{1}{2} \left[\frac{\partial U_i}{\partial x_j} - \frac{\partial U_j}{\partial x_i} \right]$$

here S_{ij} is the mean strain rate. Since Ω_{ij} is antisymmetric and $-\langle u_i u_j \rangle$ is symmetric, their contraction is zero, so it follows that:

$$-\langle u_i u_j \rangle \frac{\partial U_i}{\partial x_j} = -\langle u_i u_j \rangle S_{ij}$$

Similarly,

$$\langle s_{ij} \frac{\partial u_i}{\partial x_j} \rangle = \langle s_{ij} s_{ij} \rangle$$

An equation for the fluctuating kinetic energy for stratified flow can be obtained:

$$\begin{aligned}
 \overbrace{\frac{\partial E}{\partial t}}^{\text{A}} + \overbrace{U_j \frac{\partial E}{\partial x_j}}^{\text{B}} = & \overbrace{-\frac{\partial}{\partial x_j} \left(\frac{1}{\rho} \langle p u_i \rangle \right) \delta_{ij}}^{\text{C}} - \overbrace{\frac{\partial}{\partial x_j} \langle u_i u_i u_j \rangle}^{\text{D}} + \overbrace{\frac{\partial}{\partial x_j} (2\nu \langle s_{ij} u_i \rangle)}^{\text{E}} \\
 & - \underbrace{\langle u_i u_j \rangle \frac{\partial U_i}{\partial x_j}}_{\text{F}} - \underbrace{2\nu \langle s_{ij} s_{ij} \rangle}_{\text{G}} - \underbrace{\frac{g}{\rho} \langle u_i \rho' \rangle \delta_{i3}}_{\text{H}}
 \end{aligned} \tag{2.3}$$

The physical meanings of the terms in the above equation are as following:

- A: rate of change of kinetic energy (KE) per unit mass due to non-stationarity;
- B: rate of change of KE due to advection;
- C: transport of KE due to pressure fluctuations;
- D: transport of KE due to turbulence itself (turbulent velocity fluctuation);
- E: transport of KE due to the viscous stresses;
- F: rate of production of TKE from the mean flow P ;
- G: rate of dissipation of KE per unit mass due to viscous stresses;
- H: work done against the buoyancy flux.

In a steady, homogenous, incompressible pure shear flow, the turbulent kinetic energy does not change with time; all averaged quantities except for U_i are independent of position and S_{ij} is constant, so the terms A, B sum up to zero and C, D, E are generally neglected:

$$-\langle u_i u_j \rangle S_{ij} - 2\nu \langle s_{ij} s_{ij} \rangle - \frac{g}{\rho} \langle w \rho' \rangle = 0 \tag{2.4}$$

$$P - \varepsilon - B = 0 \tag{2.5}$$

Thus for a steady-state situation, the turbulent energy is balanced between the turbulent production P , the dissipation ε and the work against buoyancy (Osborn 1980), i.e. the negation of buoyancy flux B . The ratio of buoyancy flux (potential energy gained by mixing) and the turbulent production (kinetic energy required for mixing) is defined to be the flux Richardson number R_f . Then Eq. 2.5 is reduced to $B/R_f - \varepsilon - B = 0$. The buoyancy flux, B , is often described as the product of the density gradient and the diapycnal diffusivity

2. THEORY

K_ρ , a scalar eddy coefficient for density:

$$B = \frac{g}{\rho} \langle w\rho' \rangle = -\frac{g}{\rho} K_\rho \frac{\partial \rho}{\partial z} = K_\rho N^2 \quad (2.6)$$

where $N (= \sqrt{-\frac{g}{\rho} \frac{\partial \rho}{\partial z}})$ is the buoyancy frequency. Thus the diapycnal diffusivity K_ρ can be expressed by the energy dissipation ε and buoyancy frequency N :

$$K_\rho = \frac{R_f}{1 - R_f} \frac{\varepsilon}{N^2} = \frac{\Gamma \varepsilon}{N^2} \quad (2.7)$$

In steady states, the value of R_f must be less than 1. Osborn suggested a critical value of 0.15, i.e., $R_f \leq R_{f\text{crit}} = 0.15$, so that the mixing efficiency $\Gamma \leq 0.2$ (Osborn, 1980). In studies of inferring K_ρ from dissipation, the upperbound $\Gamma = 0.2$ is widely used, assuming that 20% of the energy dissipate is used to mix the ocean, to drive the overturning circulation in the abyssal ocean.

2.2 Advection-diffusion balance

The modern theory of the abyssal circulation is traced to a series of remarkable papers in the 60s by Stommel and his collaborators (Stommel, 1958; Stommel and Arons, 1960a, b; Stommel *et al.*, 1958).

Prior to the late 1950s, estimates of overturning in the Atlantic based on hydrographic data suggested only a number of 6-8 Sv of overturning or inter-hemispheric exchange; then Stommel, Arons and Faller suggested 15-25 Sv on theory of deep circulation (Stommel and Arons, 1960a,b) and assumption on account of lab experiment (Stommel *et al.*, 1958).

Stommel and Arons developed a theory analogous to Sverdrup theory in the context of the abyssal circulation. The fundamental assumption of this theory includes: (1) deep water is supplied by convection in the North Atlantic, and in Weddell Sea in the South; (2) cold water is brought by uniform upwelling back toward surface; (3) deep circulation is geostrophic in the interior. The downward diffusion of heat from the surface and the upward advection of cold water from the abyss are in balance:

$$\vec{u} \cdot \nabla T + w \frac{\partial T}{\partial z} = \kappa \frac{\partial^2 T}{\partial z^2} \quad (2.8)$$

the first term represents horizontal advection of the temperature, κ the diffusivity of heat. The sinking of surface water occurs in local regions of the polar ocean, which must be balanced by rising of deep water somewhere. Supposing the compensation upwelling is similarly confined in local, the specific regions could be observed easily as the source regions. Nevertheless, such regions have not been observed, suggesting that the upwelling should be widespread and thus too slow to be detected directly (Pedlosky, 1996).

Munk further developed the simple model used by Wyrтки (1962) to estimate the oxygen minimum, a vertical model involving “advection and mixing” (Munk, 1966), which was then widely referred and discussed by later researchers. He assumed a one-dimensional (vertical) advection-diffusion bal-

2. THEORY

ance in a steady state with the form of:

$$w \frac{\partial \rho}{\partial z} = \frac{\partial}{\partial z} \left(K_\rho \frac{\partial \rho}{\partial z} \right) \approx K_\rho \frac{\partial^2 \rho}{\partial z^2} \quad (2.9)$$

In this model, a simplified uniform upwelling is applied over the entire abyssal ocean, thus w is constant. The coordinate z is normal to the isopycnals. This “conventional” view assumes quasi-uniform mixing everywhere in the ocean, at a rate roughly proportional to $K_\rho \rho_z / \rho_{zz}$, with either constant K_ρ or one varying only in the vertical direction. This model is similar to Stommel-Arons’ outcome of horizontal circulation in the deep ocean, and similar numerical outcomes was also inferred based on analysis of observations from the central Pacific. For a deep water formation rate of 25 Sv, the uniformly distributed upwelling velocity is $w \approx 0.5 - 1 \text{ cm day}^{-1} \sim 10^{-7} \text{ m s}^{-1}$; the scale height, $z_0 = K_\rho / w \sim 1000\text{m}$, based on the observed stratification ratio. These values led to an eddy diffusivity of $K_\rho \sim O(10^{-4} \text{ m}^2 \text{ s}^{-1})$.

In practice, one can also infer the transformation rate between adjacent water masses $R = w \cdot A$, with observed stratification structure and estimated diffusivities. Here A is the area of the interface of water masses; w is vertical velocity derived according to the advection/diffusion balance (2.9): $w = K_\rho \rho_{zz} / \rho_z$. It provides another perspective to evaluate the deep water formation and transformation between water masses, despite being cursory somehow, in addition to the traditional method of inferring the strength of transformation from surface buoyancy forcing. Estimation of transformation rate between major constituents of NADW is included in Section 5.4.

2.3 Internal wave and energy cascade

Away from the direct influence of boundary processes, most ocean mixing is driven by breaking of internal gravity waves (MacKinnon *et al.*, 2010). Internal waves, which arise in a stably stratified ocean interior (e.g., Gerkema and Zimmerman, 2008), are normally with typical scales from meters to kilometers (horizontal wavelength range) and have frequencies between the inertial frequency f and the buoyancy frequency of the background stratification N . The internal waves provide an important pathway of energy transfer from large scales to small scales.

Garrett and Munk (1972, 1975) patched a simple model of an universal internal wave spectrum in wavenumber-frequency spaces based on data of power and cross spectra from various sources available at that time (Fig. 2.1). Unavoidably, simplifications and assumptions are used: the internal wave field is assumed to uniformly distribute in horizontal directions, so only one horizontal wavenumber need to be considered; the energy is smeared over all horizontal or vertical wavenumbers rather than confined to discrete values (Garrett and Munk, 1979). This model is adequate for most purpose use, but only provide a general frame of the internal wave field. In situ observations are needed for definite conditions. The energy-containing large scales are well presented by the GM model, nevertheless, the small, shear-containing scales are too intermittent to be described by a universal spectrum (Müller, 1986). Fig. 2.2 gives an practical example of mean power spectra measured over the continental slope in the Bay of Biscay (van Aken *et al.*, 2007)). The internal waves, as we can perceive from the theoretical and observed equilibrium spectra, represent a random superposition of various waves with different amplitudes, wave numbers, and frequencies (Munk, 1981; Müller, 1986).

Internal waves are generated mainly either by wind stress (Alford, 2001) through the atmospheric disturbance of the ocean's upper mixed layer (approximately 0.5 TW), or by the flow of barotropic tides over sloping bottom (approximately 1 TW, from Wunsch and Ferrari, 2004). Both generate

low-frequency waves. The wind-induced internal waves are predominantly at frequencies close to the inertial frequency f ; internal tides scattering from topography (generated from barotropical tides) maintain the forcing frequency (clear peaks around f, D_2 and so forth in internal wave spectra in Fig. 2.2).

Some of the baroclinic energy inputted by tidal currents dissipates locally, but most of that radiates away in low mode waves (St. Laurent and Garrett, 2002). Unlike surface waves, the energy of internal waves propagates both horizontally and vertically. As the internal waves propagate from their generation locations, energy is transferred through wavenumber space to the intermittently unstable finescales by nonlinear wave-wave interactions and other scattering processes, until they break and dissipate. (Sun and Kunze, 1999; Ferrari and Wunsch, 2009)

Assuming the nonlinear interactions are weak, McComas and his collaborators proposed the **resonant triad interaction theory**: a triad of internal waves can transfer energy among themselves through nonlinear interactions if their frequencies satisfy the condition that $\omega_1 \pm \omega_2 \pm \omega_3 = 0$ and wavenumbers $k_1 \pm k_2 \pm k_3 = 0$ (McComas and Bretherton, 1977; McComas, 1977; McComas and Müller 1981a,b). McComas and Müller (1981a) concluded that the cascade of energy down to small dissipation scales is dominated by two resonant mechanisms: (i) parametric subharmonic instability (PSI) in which energy is transferred from low to high wavenumbers of half the basic frequency; (ii) induced diffusion (ID) scatters a wave with high wavenumber and high frequency by a low-wavenumber, low-frequency wave into another nearby high-wavenumber, high-frequency wave. The nonlinear interaction among internal waves redistributes energy and momentum among various components and determines the spectral shape of the internal wave field.

In a steady state, the transfer rate of spectral energy from low to high vertical wavenumber is supposed to equal the turbulence production rate P (see section 2.1 for details of P) and is independent of wavenumber (Sun and Kunze, 1999). Employing this equivalence, Gregg (1989) derived a semiempirical relation in which the dissipation rate caused by internal waves ε_{INT} , is expressed

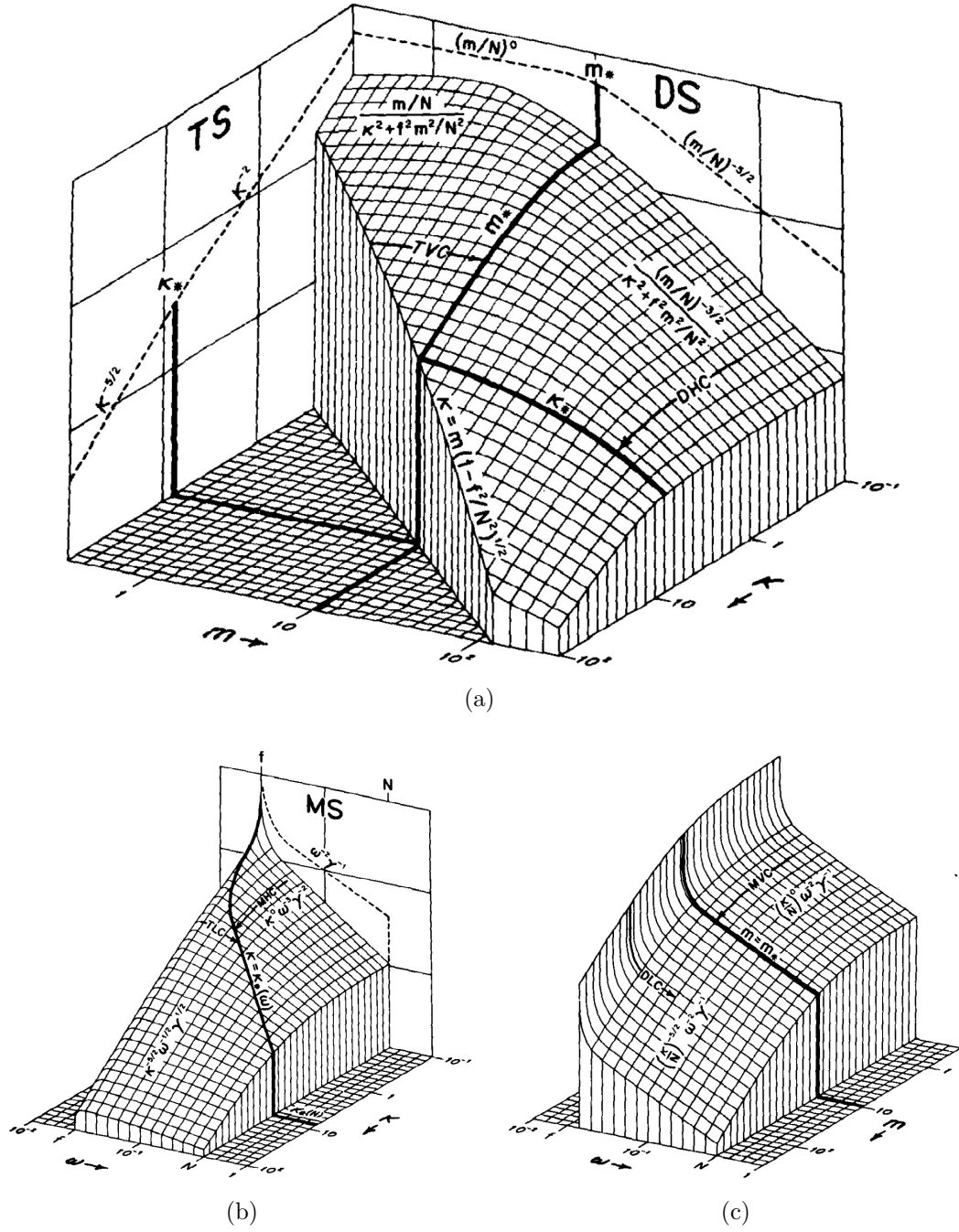


Figure 2.1: Distribution of internal wave energy in wavenumber-frequency spaces: (a) in the wavenumber space, m the horizontal and k the vertical wavenumber; (b) in the vertical wavenumber-frequency space, with ω being the frequency; (c) in the horizontal wavenumber-frequency space. Figures from Garrett and Munk(1979).

2. THEORY

in terms of the observed shear at 10-m scales in relation to the empirical GM model of the internal wave spectrum (Ferrari and Wunsch, 2009):

$$\varepsilon_{int} = 7 \times 10^{-10} \left\langle \frac{N^2}{N_0^2} \right\rangle \left\langle \frac{S_{10}^4}{S_{GM}^4} \right\rangle \text{W kg}^{-1} \quad (2.10)$$

where $N_0 = 5.2 \times 10^{-3} \text{ s}^{-1}$ is a reference buoyancy frequency, S_{10} is the observed shear variance at scales greater than 10m, and S_{GM} is the corresponding variance in the GM spectrum. Eq. (2.10) is the principal foundation which the estimation in this work is based on. Eq. 2.10 and its modifications (Polzin *et al.*, 1995; Gregg *et al.*, 2003; Kunze *et al.*, 2006) are confirmed to be consistent with the observed dissipation rates away from ocean boundaries within a factor of two, suggesting that internal waves are a major pathway to energy dissipation in the global ocean (Ferrari and Wunsch, 2009).

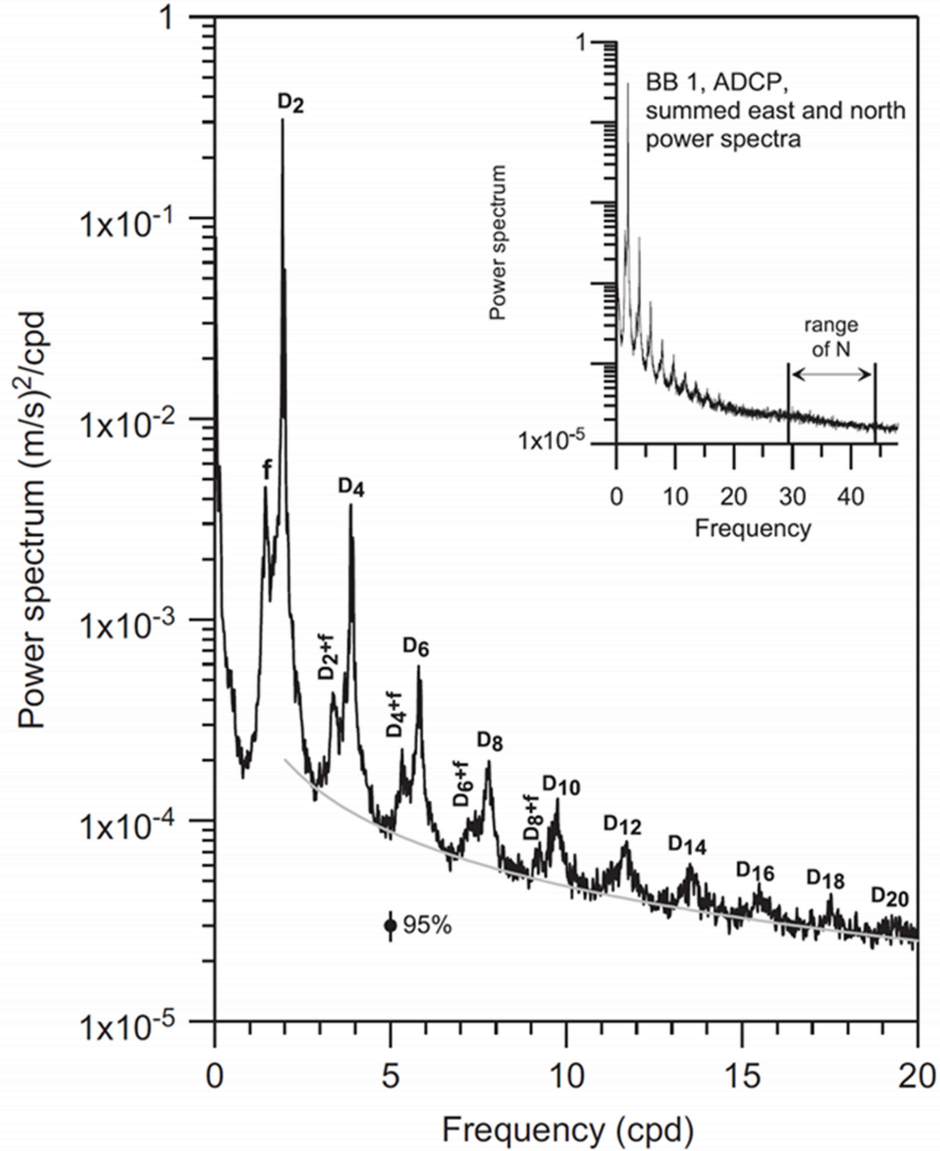


Figure 2.2: A practical example of mean power spectra of the horizontal velocity, obtained by summing the power spectra of the east and north velocity components. The entire internal-wave band is shown in the inserted figure in the upper right corner. The main figure shows the low-frequency part, containing the inertial and tidal peaks; D_2 refers to the semi-diurnal frequencies (M_2 and S_2) and so forth. From van Aken *et al.*, 2007.

Chapter 3

Data and Method

3.1 Data

During the years from 2003 to 2011, 9 hydrographic research cruises were carried out in the subpolar North Atlantic (Tab. 3.1), with a total of 737 stations (black dots in Fig. 3.2) observed with high - quality simultaneous CTD (conductivity - temperature - depth) and LADCP (lowered acoustic Doppler current profiler) measurements.

During these cruises, temperature T , conductivity C and pressure P (inferred as depth D) were measured with a Seabird SBE 911plus CTD system, which was connected to a water sampler carousel with 22 10L bottles. The accuracy for temperature is 0.002 K and that for salinity is 0.002 - 0.003 psu.

Currents were measured by a LADCP system. Two RDI 300 kHz Workhorse Monitor LADCPs were attached to the carousel, one on the top looking upward, and the other one attached to the bottom and looking downward. They were used in a synchronized Master - and - Slave mode, where the lower Master (lower one) triggers the upper Slave (see Fig. 3.1). The instruments were powered by an external battery supply, consisting of 35 commercial quality 1.5V batteries assembled in a pressure resistant Aanderaa current meter housing. The system was set to a ping rate of 1 ping s^{-1} and a vertical resolution of 10 m, resulting in an accuracy of 2 cm s^{-1} for the horizontal velocity of each

3. DATA AND METHOD

individual bin (Visbeck, 2002). The total range of the package reached from 100m to 300m, with larger range in the upper parts of the water column. With typical lowering (1 m s^{-1}) and heaving (1.2 m s^{-1}) velocities of the instrument package, this range allowed 100 to more than 200 shear estimates per depth bin (10m) in the deep water, and up to 500 estimates in the upper layers, depending on the abundance of backscatters. The velocity is inferred with the inverse method. For the details of LADCP data processing, the reader is referred to Fischer and Visbeck (1993), Visbeck (2002).



Figure 3.1: Instrument package

In addition, during cruise MSM-09/1, 7 stations were included accompanying microstructure measurements using loosely-tethered MSS90D profiler manufactured by Sea&Sun Technology in cooperation with ISW - Wassermesstechnik. The MSS stations are shown with red dots in Fig. 3.2: three stations were

3. DATA AND METHOD

Table 3.1: Cruises

Cruise	Time	Ship	latitude range (°N)	Profiles
M59/2	21.07 - 25.08.2003	RV Meteor	46.5 - 61.8	133
SUBPOLAR	02.06 - 12.07.2005	N/O Thalassa	46.5 - 62.4	110
MSM-05/1	05.04 - 15.05.2007	RV Maria S. Merian	42.0 - 47.7	35
64PE278	26.10 -18.11.2007	RV Pelagia	43.2 - 59.9	47
MSM-09/1	23.07 -18.08.2008	RV Maria S. Merian	46.5 - 52.6	78
SUBPOLAR-08	25.08 -15.09.2008	N/O Thalassa	52.3 - 60.3	63
MSM-12/3	15.07 - 12.08.2009	RV Maria S. Merian	47.0 - 62.0	85
M82/2	05.08 - 01.09.2010	RV Meteor	47.0 - 53.0	73
M85/1	24.06 - 02.08.2011	RV Meteor	47.0 - 60.3	113

located to the west of Mid-Atlantic Ridge (MAR) with repeated cast of MSS profiles; four in the centre of the Deep Western Boundary Current (DWBC) off Flemish Cap (around 47°N, 45°W). Stations over MAR were measured with single cast of CTD/LADCP profiles but repeated MSS casts. Among stations at the western boundary, one was measured with both single MSS cast and CTD/LADCP profiles, one with repeated MSS casts and single CTD/LADCP profile, and the other two stations with both repeated MSS and CTD/LADCP profiles. The MSS profiler was equipped with two shear sensors (airfoil), a fast temperature sensor (FP07), an acceleration sensor, tilt sensors and standard CTD sensors. (see Prandke and Stips (1998) for details of the instrument). The profilers were adjusted to descent at 0.5 - 0.6 m s⁻¹. Altogether, 28 profiles of direct measurements of microstructure shear and temperature were collected from the surface down to a maximum depth of 1265 m (from cruise report of MSM 09-1[78]). Dissipation rate of turbulence is computed at these stations, and accordingly K_ρ is inferred (see Section 3.2.4 for details). Despite the lack of shear observations at depth, the direct estimation of K_ρ are valuable to qualify the accuracy and the applicability of the fine - scale parameterization. This part of work is further explained in Section 3.2.4.

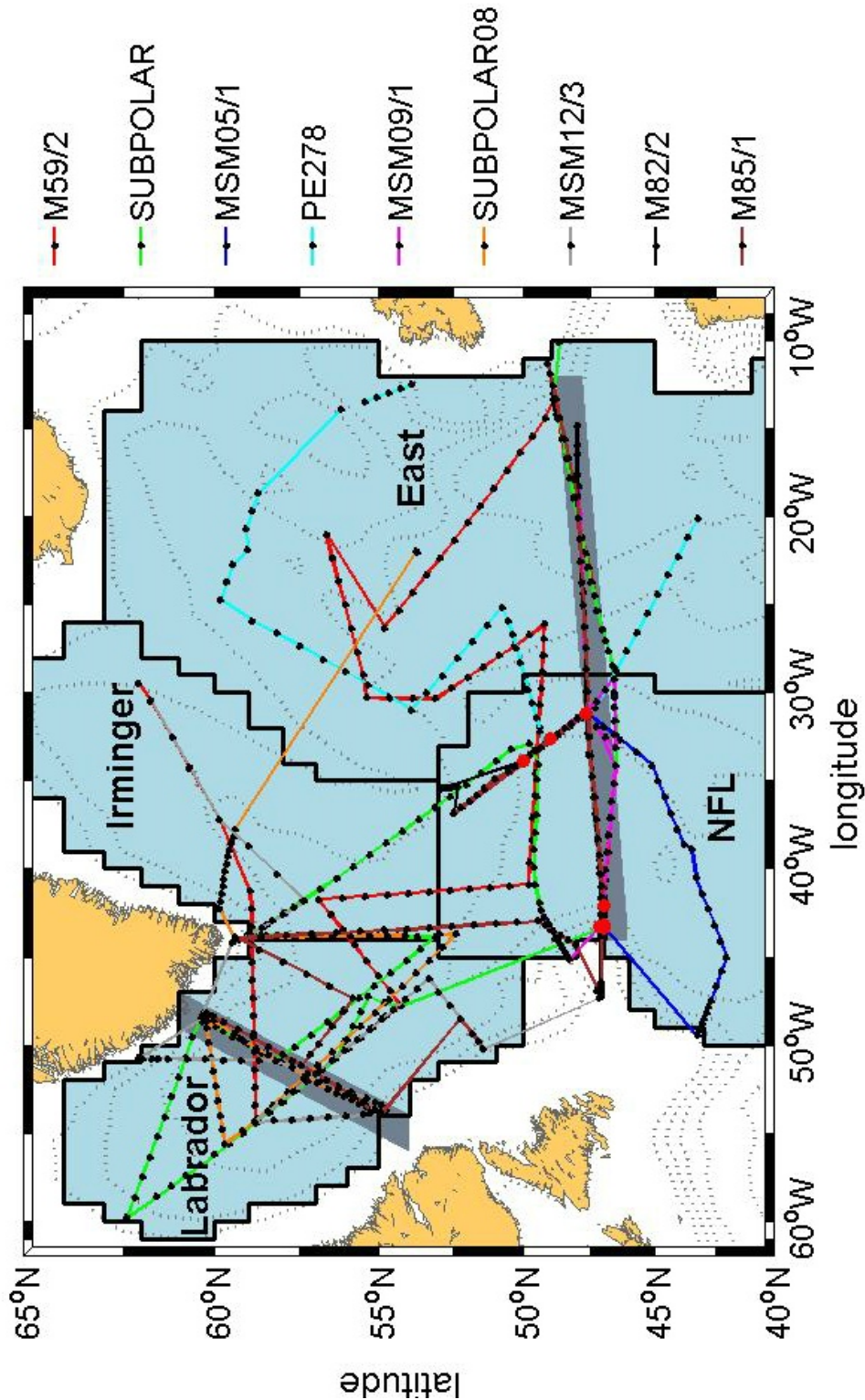


Figure 3.2: Map of all cruises. Black dots indicate stations with ADCP and CTD data, red dots stations with both ADCP, CTD data and microstructure measurements. Isobaths are shown with light gray lines with intervals of 1000m; gray shadings indicate areas of two sections that are analyzed in section 4.2; bluish shadings with black frames indicate the locations of 4 regions: inner Labrador Sea (Labrador), Irminger Sea (Irminger), Newfoundland Basin (NFL) and East Basin (East).

3.2 Method

3.2.1 Fine-scale parameterization

The dissipation rate of turbulent kinetic energy ε is estimated from the fine-scale velocity observations using the parameterization depending on shear variance $\langle V_z^2 \rangle$ (Gregg *et al.*, 2003):

$$\varepsilon = 6.73 \times 10^{-10} \frac{\text{W}}{\text{kg}} \frac{N^2}{N_0^2} \frac{\langle V_z^2 \rangle^2}{\langle V_z^2 \rangle_{\text{GM}}^2} h(R_\omega) j(f, N) \quad (3.1)$$

where N is buoyancy frequency, $N_0 = 5.2 \times 10^{-3} \text{ rad s}^{-1}$ is the assumed background stratification in the GM model, $\langle V_z^2 \rangle$ is the mean variance of velocity shear with $\langle \rangle$ represents the spatial average in the profile segments, and parameters with subscript ‘GM’ represent the reference values from the Garrett-Munk (GM) internal wave model. $h(R_\omega)$ is a function of shear-strain variance ratio R_ω accounting for distortions in the frequency content and $j(f, N)$ is a correction term that contains the latitudinal variation of the inertial frequency f . H and j are given by

$$h(R_\omega) = \frac{3(R_\omega + 1)}{2\sqrt{2}R_\omega\sqrt{R_\omega - 1}} \quad (3.2)$$

$$j(f, N) = \frac{f \operatorname{arccosh}(N/f)}{f_{30} \operatorname{arccosh}(N_{30}/f_{30})} \quad (3.3)$$

$$R_\omega = \frac{\langle V_z^2 \rangle}{\bar{N}^2 \langle \xi_z^2 \rangle} \quad (3.4)$$

here f_{30} , N_{30} are inertial and buoyancy frequencies at the 30 °N GM model reference latitude, $\langle \xi_z^2 \rangle$ is strain variance, and \bar{N} represents the mean buoyancy frequency in each sub-profile.

The reference GM shear variance is derived following Gregg and Kunze (1991):

$$\frac{\langle V_z^2 \rangle_{\text{GM}}}{\bar{N}^2} = \frac{3\pi E_0 b j_*}{2} \int_{2\pi/160}^{2\pi/60} \frac{k_z^2 dk_z}{(k_z + k_{z*})^2} \quad (3.5)$$

3. DATA AND METHOD

where $E_0 = 6.3 \times 10^{-5}$ is a dimensionless energy level, $b = 1300\text{m}$, $j_* = 3$, and $k_{z*} = (\pi j_*/b)(N/N_0)$.

The turbulent diffusivity is determined from the dissipation rate ε applying the relation (Osborn, 1980)

$$K_\rho = \frac{\Gamma \varepsilon}{N^2} \leq \frac{0.2\varepsilon}{N^2} \quad (3.6)$$

here the mixing efficiency Γ is set to the upper limit value of 0.2. Substituting 3.6 into 3.1, turbulent diffusivity K_ρ is derived (Kunze *et al.*, 2006)

$$K_\rho = 0.05 \times 10^{-4} \frac{\text{m}^2}{\text{s}} \frac{\langle V_z^2 \rangle^2}{\langle V_z^2 \rangle_{\text{GM}}^2} h(R_\omega) j(f, N) \quad (3.7)$$

The parameterization here explicitly uses the Osborn relation 3.6. The validity of the relation is checked with the MSS data in section 3.2.4. Note that the parameterization with the finescale data (10 m - interval of velocity measurements) is not suitable in the lower part of mixed layer due to the contamination of sharp density change; this study focuses on the deep ocean, i.e., below mixed layer.

For shear variance estimates $\langle V_z^2 \rangle$, velocity records were binned into 320 m half-overlapped sub-profiles from the bottom to top, yielding more than 10,000 sub-profiles. In every sub-profile, a linear fit was removed firstly and a Tukey window with 10% tapers was applied at both ends. These sub-profiles were then Fourier transformed individually (32 points) to get shear spectra $S[V_z](k_z)$. In the pre-process of ADCP data, biases arise due to the smoothing by range averaging, depth binning, instrument tilting, and from the use of velocity inversion method. Therefore a transfer function for correcting shear spectral S_{correct1} was applied as suggested by Polzin *et al.* (2002) and Thurnherr (2012):

$$S_{\text{correct1}} = \frac{1}{\text{sinc}^4\left(\frac{k_z \Delta z_r}{2\pi}\right) \text{sinc}^2\left(\frac{k_z \Delta z_g}{2\pi}\right) \text{sinc}^2\left(\frac{k_z d_r}{2\pi}\right) \text{sinc}^2\left(\frac{k_z \Delta z_s}{2\pi}\right)} \quad (3.8)$$

in which Δz_r is the ADCP bin length, Δz_g the vertical resolution, Δz_s the superensemble pre-averaging interval with the velocity inverse method ($\Delta z_r =$

3. DATA AND METHOD

$\Delta z_g = \Delta z_s = 10$ m), and d_r is a length scale that depends on the instrument tilts statistics and on the maximum range r_{\max} of ADCP measurements: $d_r = -1.2 + 0.0857 r_{\max} - 0.000136 r_{\max}^2$. For the instrument in this study, the maximum range in which most of the ensembles have valid velocities is $r_{\max} \approx 200$ m, yielding $d_r = 10.5$ m.

The spectra of buoyancy normalized shear $S[V_z/N^2](k_z)$ are displayed in Figure 3.3 (solid lines), compared to the spectra of noise (dotted lines). Here the noise level spectra are estimated following Kunze *et al.* (2006) and corrected with Eq. 3.8. Following Polzin *et al.* (2002) the rms noise level under optimal conditions is about $2 \text{ cms}^{-1}/n_{\text{ping}}$ for the 300 kHz ADCP, where the number of pings n_{ping} per shear estimate is typically $O(100)$ for this study. The spectra are block-averaged according to the GM normalized strain variance $\langle \xi_z^2 \rangle / \langle \xi_z^2 \rangle_{\text{GM}}$ (see the following strain variance part) for display in the figure. The resulting spectra of the horizontal velocity are larger than in the GM model and presenting higher energy density with larger scaled strain variance value. The strong rise at high wavenumbers is clearly from due to the contamination of instrument noise, and the significant decrease at lower wavenumbers is due to the application of the Tukey taper. The shear variance $\langle V_z^2 \rangle$ was determined by integration of the shear spectra with respect to vertical wavenumber corresponding to wavelength $\lambda_z = 160 - 60$ m. The selection of integration intervals on the one hand includes as large a band as possible, and on the other hand excludes wavenumber intervals contaminated by instrument noise.

To estimate the strain variance $\langle \xi_z^2 \rangle$, the buoyancy frequency N inferred from temperature T , pressure P , and salinity S (all averaged onto 1db grid) was binned in the same way as velocity profiles. 256 data points were included in every single sub-profile, starting from the deepest points. Strain was estimated from buoyancy frequency using equation $\xi_z = (N^2 - \bar{N}^2)/\bar{N}^2$, where \bar{N}^2 is the quadratic fit of low-passed buoyancy frequency of each sub-profile (Polzin *et al.*, 1995). The strain spectra $S[\xi_z]$ were produced in the same way as the shear spectra, but with a 256-point Tukey window. The spectral correction

term required for the first differencing inherent in the gradient is:

$$S_{\text{correct2}} = \text{sinc}^2 \left(\frac{1\text{m} \times k_z}{2\pi} \right) \quad (3.9)$$

The spectra of the strain of density field roll off at wavelength less than around 10 m due to the saturation (Fig. 3.3). However, according to Gargett (1990), the strain variance would be underestimated if the spectrum becomes saturated at wavelength larger than 10m. So the integration of strain is confined to $\langle \xi_z^2 \rangle \leq 0.1$, corresponding to an upper limit of wavelength around 20m. Strain variance was then obtained by integration of strain spectra with respect to wavenumbers corresponding to $\lambda_z = 128 - 25$ m. The integration limits were chosen such that they exclude possible contamination by the filter method, but covers much of the wave band (with flat shape that is the same as the GM model) as possible. Note that due to the inconsistency of the integration intervals between shear and strain, the variances were scaled by the length of integrations respectively to eliminate the possible bias.

3.2.2 Spectra

The averaged spectra of strain $S[\xi_z]$ (dash-dotted lines) and shear $S[V_z](k_z)$ (solid lines) are shown in Figure 3.3. To get an overall impression, more than 10,000 subprofiles go into the average. As a quality check, the spectra of instrument noise estimates are also included. They were computed similar to shear spectra, with the accuracy of LADCP (2 cm s^{-1}) instead of observational horizontal velocity, and corrected by S_{correct1} , but not windowed as $S[V_z](k_z)$.

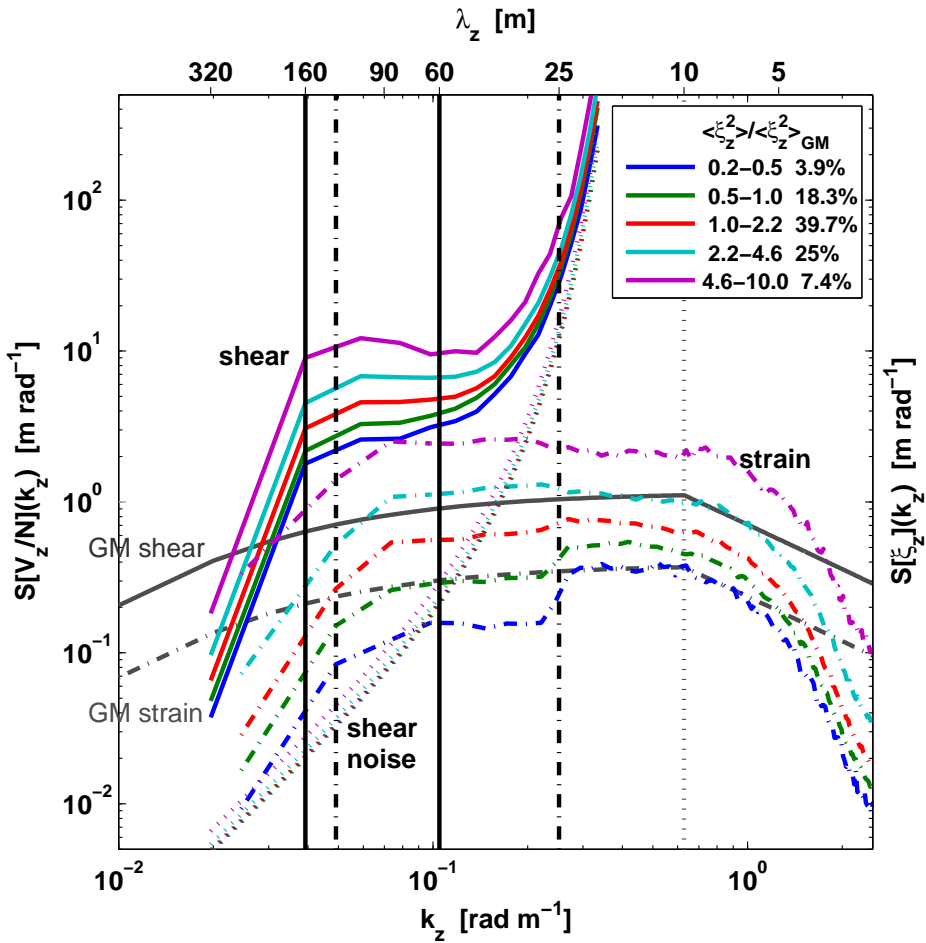


Figure 3.3: Mean spectra of shear (solid lines, normalized by the buoyancy frequency), strain (dash-dotted lines) and instrument noise (dotted lines). These spectra are binned and averaged according to the corresponding GM scaled strain variance $\langle \xi_z^2 \rangle / \langle \xi_z^2 \rangle_{\text{GM}}$, but only groups between 0.2-10.0 are shown here. The solid and dash-dotted lines in gray are spectra of GM shear and strain shown as reference.

3. DATA AND METHOD

The spectra are binned and averaged according to the GM-normalized strain variance $\langle \xi_z^2 \rangle / \langle \xi_z^2 \rangle_{\text{GM}}$ following Kunze *et al.* (2006), into seven groups, < 0.2 , $0.2-0.5$, $0.5-1.0$, $1.0-2.2$, $2.2-4.6$, $4.6-10.0$ and > 10 . The averaged spectra of five groups in the middle are shown in Figure 3.3, adding up to 90.6% of the total sub-profiles. The energy density of horizontal velocity is apparently larger than GM model. The shear spectra increase sharply at high wavenumbers, which is possibly due to the contamination of instrument noise, and decreases significantly in lower wavenumbers due to the usage of the Tukey taper. Three types of windowing methods are shown in Fig. 3.4, and their impacts on shear/strain spectra are displayed in Fig. 3.5.

The spectra of strain are generally white for small wavenumbers, and then fall off above wavenumber corresponding to around $\lambda = 10$ m. The spectra do not roll off as supposed due to the saturation, similar to the GM strain spectrum. This is possibly due to the contamination of suspicious minority of sub-profiles with high energy density at large wavenumbers.

The vertical lines establish the integration intervals of the variances for shear (dotted lines) and strain (solid lines). This selection on the one hand excludes the possible contamination by instrument noise or filter method, and on the other hand covers as many wavenumber bands as possible.

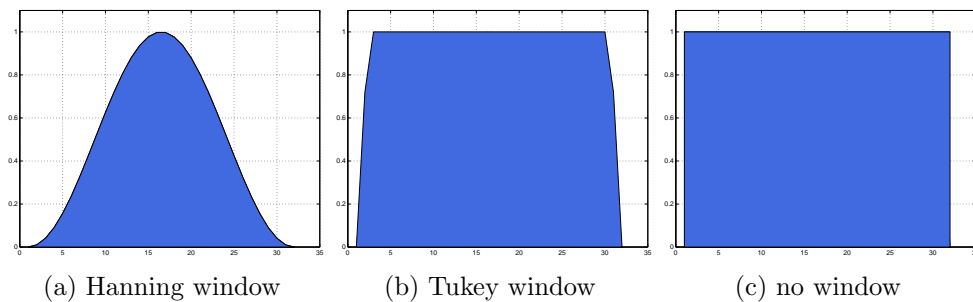


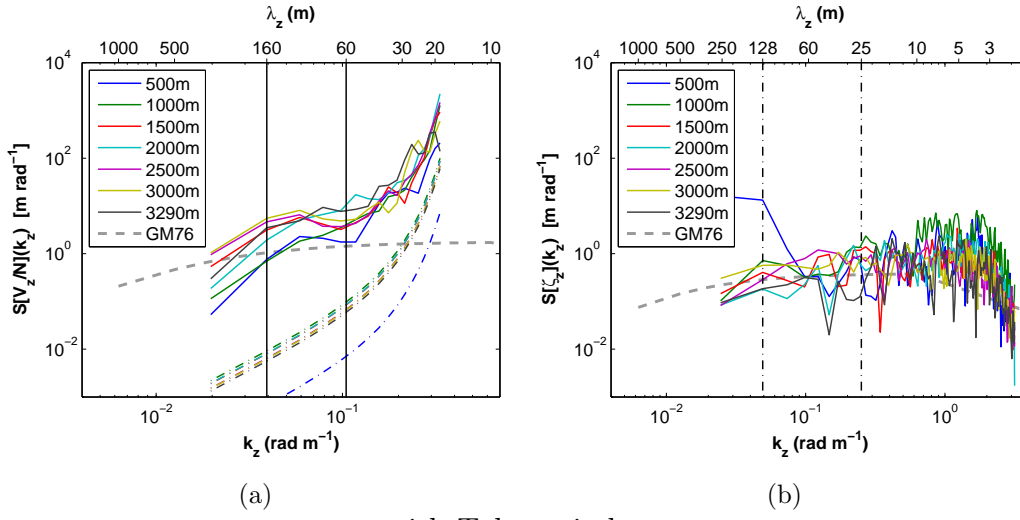
Figure 3.4: Different window types applied before FFT.

Here the shear and strain spectra are both averages of more than 10,000 sub-profiles, accordingly the lines in Fig. 3.3 just show a trend of the forms. They can be influenced by several spectra with sparse extremely large values,

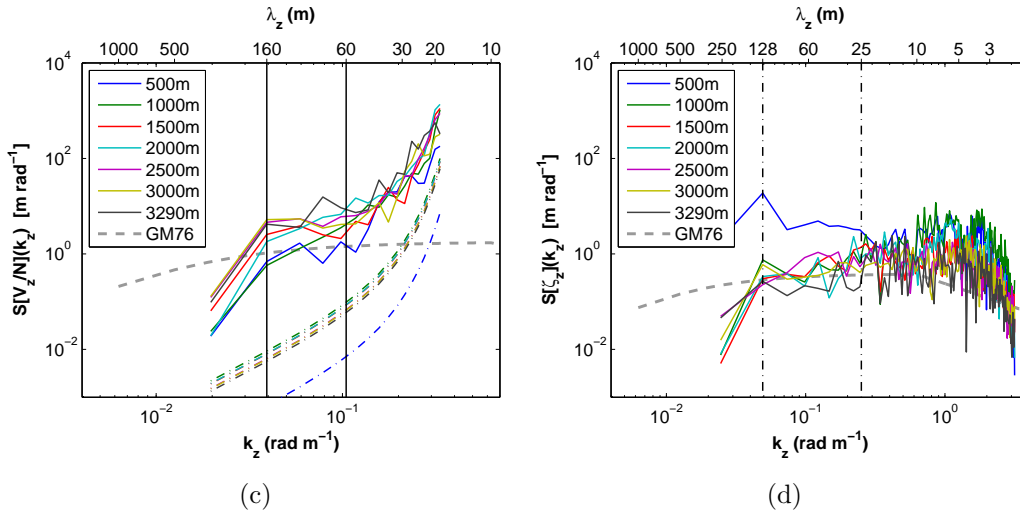
even just tens out of ten thousand, through being pulled up by extremely large values. However, most of these spectra are only with one or two anomalous points, which makes it hard to exclude all the biased spectra. Additionally, the method of taper before Fourier transform also affects their shapes. The resulting spectra of shear and strain with distinct windowing methods at a common station are shown in Fig. 3.5. The selected station is from the cruise M 59/2, locating to the east of MAR (at around 55°N , 45°W). Water depth of this location is 3456m. We can see the windowing methods affect most at small wavenumber bands, i.e., to long waves. The usage of window prior to Fourier transform (no matter Hanning or Tukey window) slightly spreads the spectra in the wavenumber domain, keeps the consistency of energy spectrum, reduces leakage from inertial and tidal peaks into the higher frequencies of the internal wave range; meanwhile it provides a small amount of spectral smoothing (smearing) (Briscoe, 1975). The severe “dive” of the spectra form at lower wavenumber end (see Fig. 3.5e and Fig. 3.5f) is mainly caused by the procedure removing linear trends of the sub-profile data. This inconsistency is smoothed better by application of Hanning window than Tukey window, but the choice of Tukey window (after Kunze *et al.*, 2006) does not influence the subsequent estimate of diffusivity since the diving parts are exclusive from the integration intervals.

3. DATA AND METHOD

with Hanning window



with Tukey window



with no window

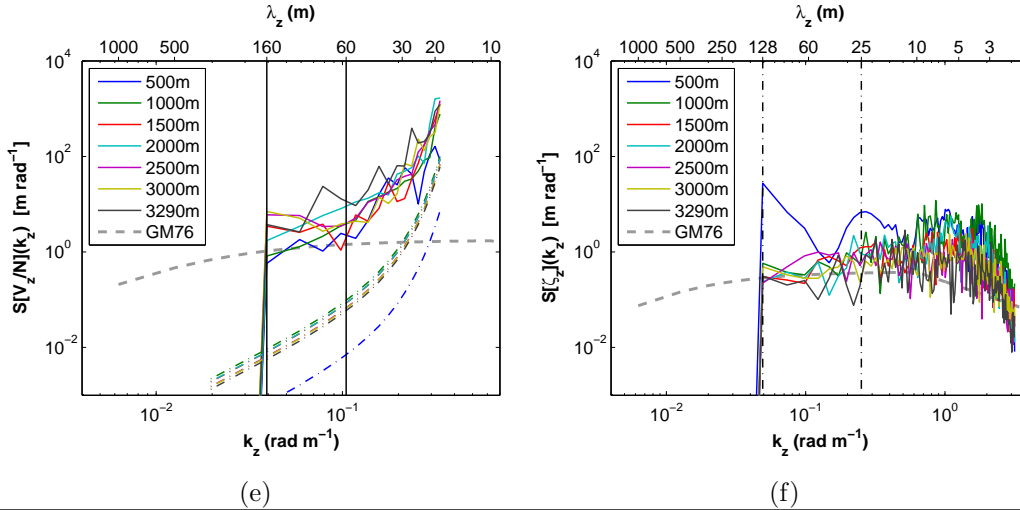


Figure 3.5: Impacts of different windows on spectral shapes, illustrated by measurements at a station around 55 °N, 45 °W in cruise M 59/2. a, c, e are spectra of shear; b, d, f are spectra of strain.

3.2.3 Shear/strain variance ratio

The corresponding shear/strain variance ratio R_ω was calculated for every sub-profile. As shown in Figure 3.6, at $N < N_{err} (\approx 5.2 \times 10^{-4} \text{s}^{-1})$, R_ω increases sharply with the decrease of buoyancy frequency; here the main source of error, instrument noise from the ADCP, becomes much more severe when the stratification is weaker, so that R_ω at $N < N_{err}$ is unusable. At $N > N_{err}$, R_ω varies between 3 - the theoretical estimate from the GM model, and 7 - the value suggested by Kunze et al. (2006). Taking into account only the sub-profiles with $\langle \xi_z^2 \rangle / \langle \xi_z^2 \rangle_{GM}$ between 0.2 and 10.0 and $N > N_{err}$, the shear/strain variance ratio has a mean value $R_\omega = 5.1 \pm 0.04$.

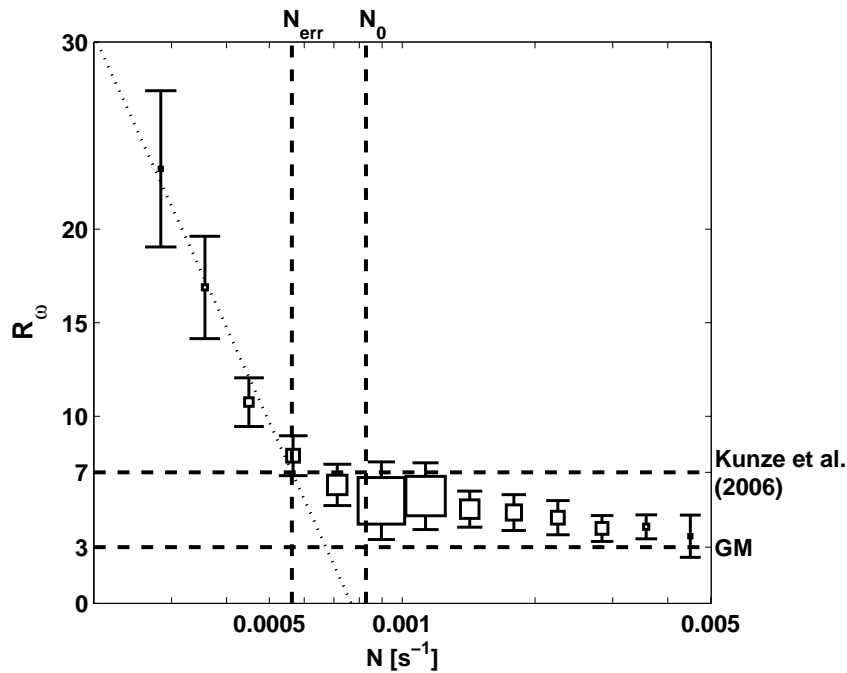


Figure 3.6: Shear/strain variance ratio averaged according to buoyancy frequency. The size of the boxes is proportional to the number of sub-profiles going into the average (6439 maximum), with a total number of 11609. Only sub-profiles with values of $\langle \xi_z^2 \rangle / \langle \xi_z^2 \rangle_{GM}$ in the range 0.2 - 10.0 are included. Errorbars indicate the standard deviation of R_ω calculated using the bootstrap method.

3. DATA AND METHOD

For a single internal wave, the variances of strain and buoyancy frequency normalized shear can be expressed as functions of its frequency ω and horizontal wavenumber k_x or vertical wavenumber k_z . Together with the dispersion relationship of internal gravity wave, another expression of shear/strain ratio is derived (Fofonoff, 1969; Kunze *et al.*, 1990):

$$\begin{aligned}
 \text{shear variance } \frac{\langle V_z^2 \rangle^2}{N^2} &= \frac{(\omega^2 + f^2)(k_z u)^2}{(\omega N)^2} \\
 \text{strain variance } \langle \xi_z^2 \rangle^2 &= \left(\frac{k_z w}{\omega} \right)^2 = \left(\frac{k_x u}{\omega} \right)^2 \\
 \text{dispersion relation } \left(\frac{k_z}{k_x} \right)^2 &= \frac{N^2 - \omega^2}{\omega^2 - f^2} \\
 \implies \text{ratio } R_\omega &= \frac{\langle V_z^2 \rangle^2}{N^2 \langle \xi_z^2 \rangle^2} = \frac{\omega^2 + f^2}{f^2} \left(\frac{f k_z}{N k_x} \right)^2 = \frac{(\omega^2 + f^2)(N^2 - \omega^2)}{N^2(\omega^2 - f^2)}
 \end{aligned} \tag{3.10}$$

This deduction is based on the linear theory and the assumption of the absence of mean flow. Thus for a single internal wave, R_ω equals the ratio of horizontal kinetic energy to available potential energy (Polzin *et al.*, 1995). The available potential energy (APE) means the excess potential energy of a stratified ocean due to an adiabatic perturbation of the background stratification. When the system returns to undisturbed state, the APE is converted into kinetic energy of fluid motion. For the GM spectrum, $R_\omega = 3$. Kunze *et al.* (2006) suggested an average value of $R_\omega = 7 \pm 3$ for world abyssal ocean based on similar CTD/LADCP measurements. This study gave an intermediate value, suggesting that in the subpolar North Atlantic, internal waves may contain more kinetic energy than GM model to dissipate, but not so much as supposed by Kunze *et al.* (2006).

3.2.4 Micro-scale structure profiling

During the cruise MSM-09/1 in 2008, 28 MSS micro structure profiles (MSS) were collected prior or following CTD / LADCP profiling, providing a possibility to examine the accuracy of the parameterization (3.7). The dissipation rate of turbulent kinetic energy ε was estimated from the microstructure measurements by integrating shear wavenumber spectra and assuming isotropic turbulence:

$$\varepsilon = 7.5\nu \int_{k_{min}}^{k_{max}} E_{du'/dz}(k) dk \quad (3.11)$$

ν being the dynamic viscosity of seawater. Shear spectra $E_{du'/dz}$ were calculated from one - second ensembles (1024 values) corresponding to a vertical interval of 0.5 - 0.6 m and integrated between a lower = 3 cpm and an upper wavenumber, which varied between 14 cpm and 30 cpm depending on the Kolmogorow wavenumber. Unresolved shear variance due to the limit wavenumber band used in the integration was accounted for by fitting the shear spectra to the universal Nasmyth spectrum using the function provided by Wolk et al. (2002). Additionally, corrections for the loss of variance due to finite sensor tip of the air foil probes were applied. For a detailed description of the algorithm used the reader is referred to Schafstall et al. (2010).

Turbulent diapycnal diffusivities K_ρ were inferred according to the relation of Eq. 3.6. The dissipation rate ε and inferred K_ρ at each station are displayed in Fig. 3.9 in 10 - m average. The stations are separated into two groups: over MAR and in western boundary region. Note profiles at stations of 57, 61 - 65 are repeated (yoyo) at the same location and are combined together as stn. 57, and stations of 67 - 69 are the same. Within the upper 20 - 30 m the dissipation rates at nearly all stations (except stn. 42) are extremely large, maybe due to the large velocity shear resulting from the influence of wind stress over ocean surface, and the instrument biases when entering the water from air. The uppermost boxes (0 - 320m deep) are not shown in the following comparison with fine-scale estimates (Fig. 3.8). It can be seen the diffusivity of 600 - 1000 m at the western boundary is obviously larger than

3. DATA AND METHOD

that over MAR, but the dissipation rate is relatively smaller. The stations at the western boundary are located at an energetic region, where NAC and DWBC flows in opposite directions and interact with each other, water at different depth there is mixed well, resulting in weaker stratification and thus higher diffusivity than over MAR.

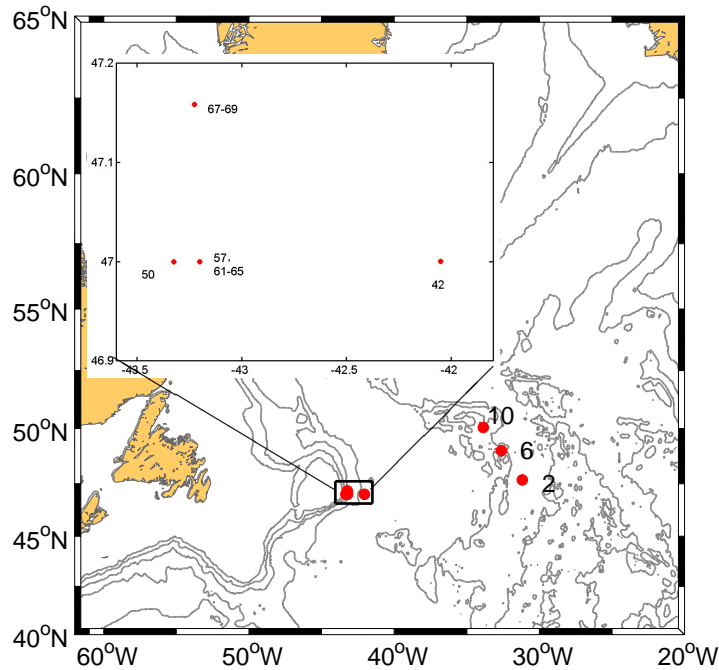


Figure 3.7: Stations in cruise MSM-09/1 with MSS profiles.

To make a comparison with finescale measurements, estimates of K_ρ from MSS profiles were binned into half - overlapped 320m boxes from top to bottom as fine-scale estimates and averaged accordingly. Prior to the calculation, the estimations of dissipation rate was examined to exclude suspicious measurements ranging at noise level. Note that due to the vibration of the instrument and the limitation of data resolution, the noise level of the dissipation rate of this MSS system is about $1.0 \times 10^{-9} \text{ W kg}^{-1}$, namely, turbulence lower than this level cannot be detected. In more energetic turbulence environments, the noise level does not influence the average dissipation rates as the mean is dominated by the energetic turbulent patches. But in low - turbulence environments (often $O(10^{-10} \text{ W kg}^{-1})$ or even lower), MSS estimations could be way too biased. To minimize the influence of noise levels in the ensemble average (within

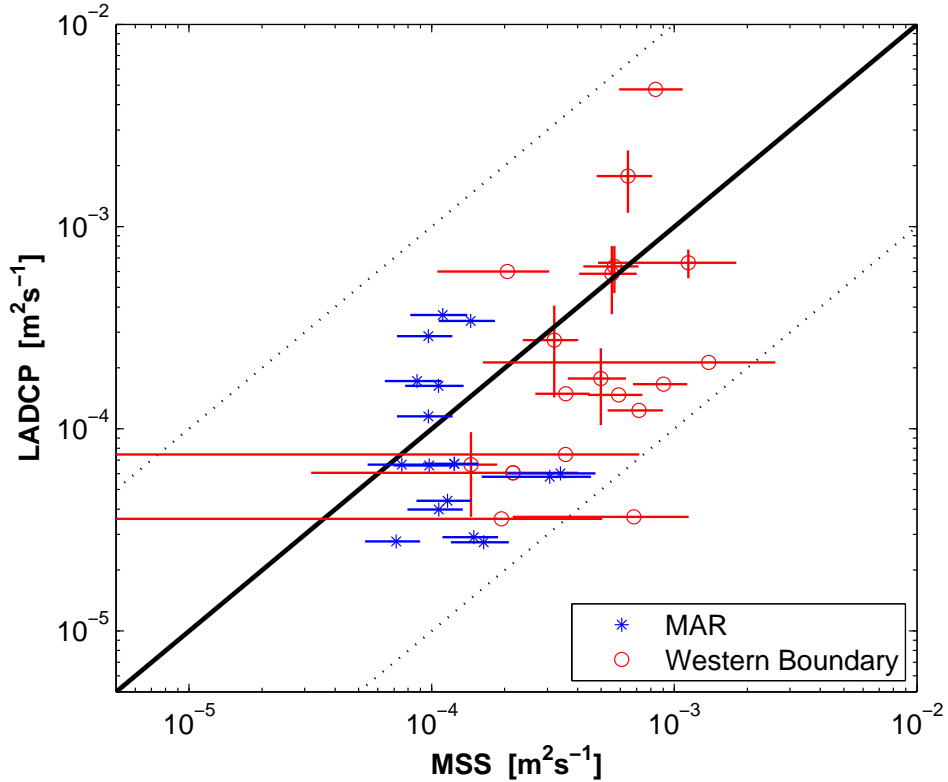


Figure 3.8: Scatter-plot of K_ρ from MSS and ADCP estimates at all stations. Blue stars for stations on the west side of the MAR, red circles for stations in the core of DWBC around 47°N . MSS estimates at stations with repeated measurements are averaged corresponding to depth bins. The black - solid line in the center indicates the case that estimates from the two observations are identical, black - dotted lines show the deviations of an order of magnitude.

320m boxes), a significant test was applied to each ensemble following Gregg (1989) and Hummels *et al.* (2013). The dissipation rate estimates at the noise level ($< 1.5 \times 10^{-9} \text{ W kg}^{-1}$) are set to the constant value of $1 \times 10^{-10} \text{ W kg}^{-1}$ and a data - modified average of the ensemble is calculated. If the modified average is similar to the average value of the original data set, the ensemble average is significant; if the modified average is much smaller than the original one, the ensemble is unused in the following comparison.

The inferring of K_ρ from dissipation rate with the Osborn relation (Eq. 3.6) is under the assumption of efficient mixing. However, it is not always the

3. DATA AND METHOD

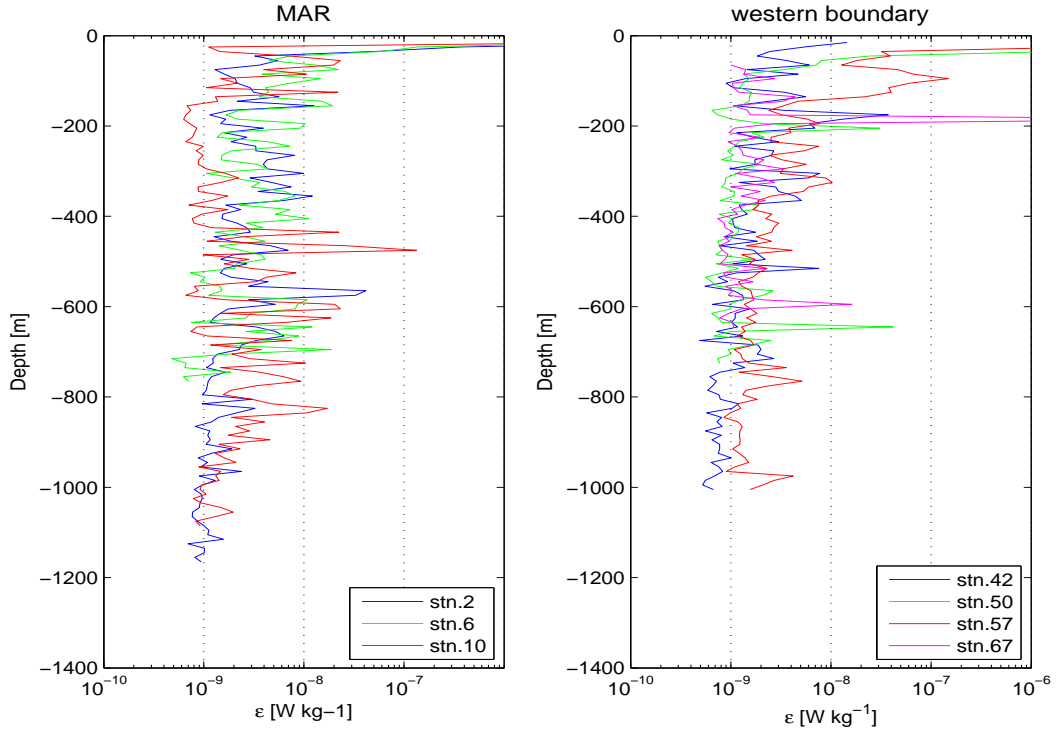
case, i.e., sometimes turbulences are detected but the mixing does not exist or not “adequate” (Ivey *et al.*, 2008). The mixing efficiency R_f strongly depends on the stratification of the ocean (Rehmann and Koseff, 2004) and the turbulence intensity (expressed by the turbulence activity parameter $\varepsilon/\nu N^2$) (Gargett, 1988; Shih *et al.*, 2005). The Osborn relation is well - grounded when the turbulence activity varies between 1 and 100. In energetic regime where $\varepsilon/\nu N^2 > 100$, R_f decreases with the increase of turbulent activity parameter (Shih *et al.*, 2005), the parameterization (3.7) generally overpredicts the computed diffusivity. In the case of this study, over 50% of the turbulence activity parameter at the western boundary exceeds 100, mostly at depths larger than 500 m, thus overestimation of K_ρ from Osborn’s relation is supposed due to the usage of a fixed mixing efficiency.

For stations with repeated casts of MSS profiling, K_ρ is set to be the mean of all profiles at the same station. The comparison between estimates derived from the microstructure measurements and the near - simultaneously collected LADCP/CTD profiles is displayed in Fig. 3.8. To evaluate the standard error of average diffusivity (shown by horizontal bars in Fig. 3.8), we used Gaussian error propagation following Schafstall *et al.* (2010):

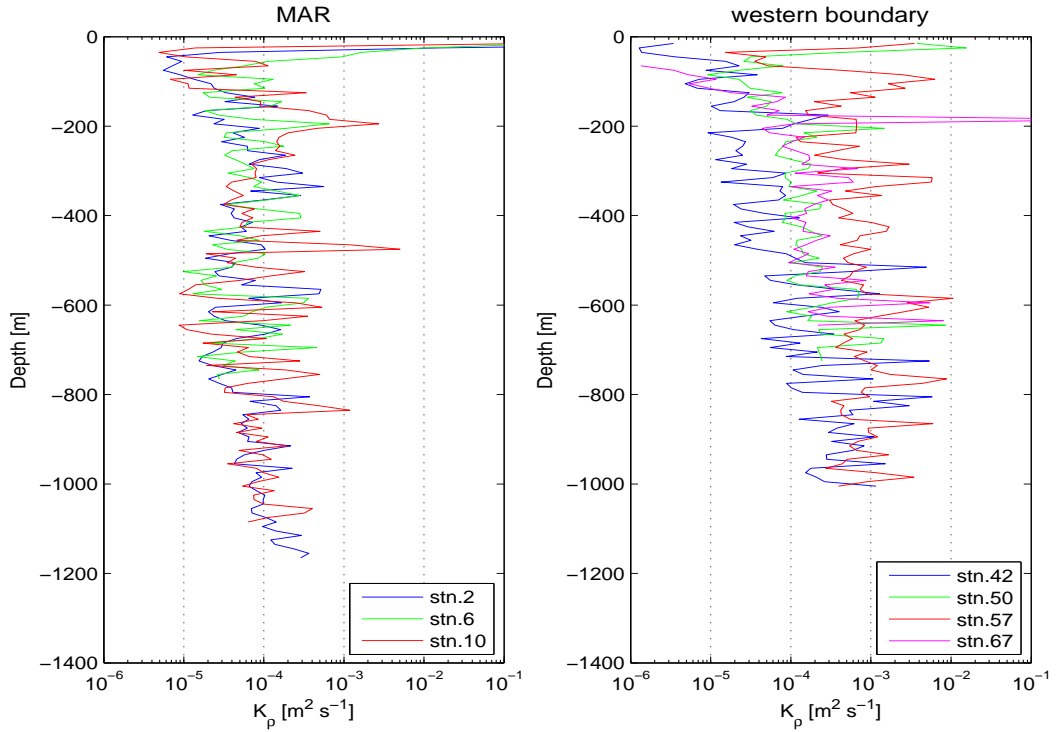
$$\Delta K_\rho = K_\rho \left[\left(\frac{\Delta \Gamma}{\Gamma} \right)^2 + \left(\frac{\Delta \varepsilon}{\varepsilon} \right)^2 + \left(\frac{\Delta N^2}{N^2} \right)^2 \right]^{1/2} \quad (3.12)$$

here Δ denote the absolute uncertainties. $\Delta \Gamma$ is set to be a constant value of 0.05; $\Delta \varepsilon$ and ΔN^2 are the standard deviations of the variables from individual profiles in each box using a bootstrap method (Efron, 1979, see section 3.3 for detail). For stations with repeated LADCP/CTD casts, we also calculate the standard deviations of K_ρ from individual profiles as the uncertainties in every sub-profile (shown by vertical bars). The disparities between these two estimates are mostly within 1 order of magnitude, accordingly we could suppose that the fine scale parameterization is consistent with the direct measurements of MSS profiles, although with some slight overprediction at the western boundary region.

3. DATA AND METHOD



(a)



(b)

Figure 3.9: 10 - m averaged ε (upper) and inferred K_ρ (lower) at eachstation (left: over MAR; right: in western boundary region). ε and K_ρ at stn. 57 denote averages of stn. 57, 61 - 65, and those at stn. 67 are averages of stn. 67 - 69.

3.3 Errors and uncertainties

In the process of measurements and data analysis, noise and uncertainties are unavoidable. The instrument noise mentioned in the section of 3.2.2 includes noise contained in the raw data due to other acoustic sources besides the ADCP, interference between instruments, reflections from moving targets, and bottom returns from previous pings (Visbeck, 2002), and errors from the processing of raw data to derive the velocity profiles. The former source is straightforward, inevitable, and can be qualified by instruments' built-in quality controls and additional manual monitoring (to remove large outliers). The later one, arising from the processing of raw data, can be optimized with optimal choice of instrument hardware and parameter setting.

3.3.1 Pre-process of ADCP data and instrument noise

In the pre-processing of LADCP data, an individual full-ocean-depth velocity profile results from successive overlapping velocity profiles. The measured velocity U_{ADCP} consists of three parts:

$$U_{\text{ADCP}} = U_{\text{ocean}} + U_{\text{ctd}} + U_{\text{noise}} \quad (3.13)$$

here U_{ocean} is the current velocity to be determined, U_{ctd} the motion of instrument package with the CTD sensor, U_{noise} the background noise due to measurement noise and non-homogeneous flow in a depth cell. For the entire measurement cast, the time integral of U_{ctd} over the cast duration T equals the horizontal ship displacement DX_{ship} :

$$DX_{\text{ship}} = X_{\text{ship}}^T - X_{\text{ship}}^0 = \overline{U_{\text{ship}}} T = \int_0^T U_{\text{ctd}} dt \quad (3.14)$$

where the displacement of the ship is inferred from the ship navigation of high accuracy GPS. The processing of LADCP data in this work follows Visbeck (2002) with a linear inverse method. The equation 3.13 can be considered as

a set of linear equations of the form:

$$\mathbf{d} = \mathbf{G}\mathbf{u} + \mathbf{n} \quad (3.15)$$

here the vector \mathbf{d} represents the data vector containing all U_{ADCP} within the water column, \mathbf{G} a coefficient matrix expressing the dynamics of Eq. 3.13 and \mathbf{n} the noise due to imperfect measurements in \mathbf{d} and the imperfect prediction of the true velocity field in $\mathbf{G}\mathbf{u}$. The vector \mathbf{u} is the combination of the motion of instrument package U_{ctd} and unknown velocity profile:

$$\mathbf{u} = \begin{bmatrix} U_{ctd} \\ U_{ocean} \end{bmatrix} \quad (3.16)$$

The number of velocity observations $n_{\mathbf{d}}$ is given by the number of pings n_{ping} times the number of depth cells per ping n_{cell} times the number of instruments (ADCPs) used n_{ADCP} ($= 2$): $n_{\mathbf{d}} = n_{ping} \cdot n_{cell} \cdot n_{ADCP}$. The number of unknowns $n_{\mathbf{u}}$ is a sum of the number of U_{ctd} which equals the number of pings n_{ping} , and the number of desired ocean velocities $n_{ocean} = H / \Delta z$ with H the depth of total profile and Δz the resolution. In the dataset of this work, Δz were all chosen to be equal to the ADCP bin length of 10 m. Normally $n_{\mathbf{d}}$ exceeds $n_{\mathbf{u}}$, thus the system is a overdetermined problem and can be solved using the least squares method by minimizing the objective function

$$J = (\mathbf{G}\mathbf{u} - \mathbf{d})^T (\mathbf{G}\mathbf{u} - \mathbf{d}) \quad (3.17)$$

The solution of Eq. 3.17 is

$$\mathbf{u} = [\mathbf{G}^T \mathbf{G}]^{-1} \mathbf{G}^T \mathbf{d} \quad (3.18)$$

Note that the LADCP measurements alone can give only a baroclinic velocity profile (the depth varying part) relative to the moving device itself (Visbeck, 2002). Therefore, external informations such as bottom track and smoothness constraints are necessary to improve the estimates of ocean velocity profile. The most important one is the barotropic constraint (the depth-average part of velocity profile), which prescribes the time average of unknown instrument motion using Eq. 3.14. Adding the barotropic term to the system of Eq. 3.15:

Namely, for a multiplication product $y = a \cdot x_1 \cdot x_2 \cdots x_N$ (a is an arbitrary constant), the relative error is the result of sum of all the relative errors of the measured variables:

$$\frac{\Delta y}{y} = \left[\left(\frac{\Delta x_1}{x_1} \right)^2 + \left(\frac{\Delta x_2}{x_2} \right)^2 + \cdots + \left(\frac{\Delta x_N}{x_N} \right)^2 \right]^{1/2} \quad (3.22)$$

This is how the uncertainty of K_ρ is inferred, since K_ρ is the multiplication of buoyancy frequency, dissipation rate, mixing efficiency in the estimation and other constant parameters, as shown in Eq. 3.12. (Lindberg, 2009)

3.3.3 Bootstrap method

In statistical theory, there are two essential prerequisites: (1) the data obeys normal (Gaussian) distribution; (2) the theoretical properties of the measurement can be analyzed mathematically, i.e. an analytical expression exists to connect the model and data statistical properties. However, in oceanographic measurements, data and model are often nonlinear, so it is not possible to satisfy the second limitation. Besides, in most case of this work, there is only one set of observations, thus it is also hard to assert that the small-samples obey the Gaussian distribution. Therefore, the estimation of standard deviations are generally calculated applying a nonparametric statistical method, the Bootstrap method.

The bootstrap method is a technique of resample. An artificial data sets with identical size to the original set is generated by selection of points from the original set, with each component chosen randomly. As a consequence, any record can be drawn more than once, once, or not at all. Then the procedure of reconstruction is repeated again and again, to get certain numbers of groups of artificial data sets (2000 in this work). Statistics are computed on each sample and the standard deviation is computed accordingly. The method is based on the idea that one can repeat a particular experiment by constructing multiple data sets from the one measured data set. Due to the confinement of small-sized data sets, variations and standard deviations in this work are basically

3. DATA AND METHOD

calculated using bootstrap method.

Chapter 4

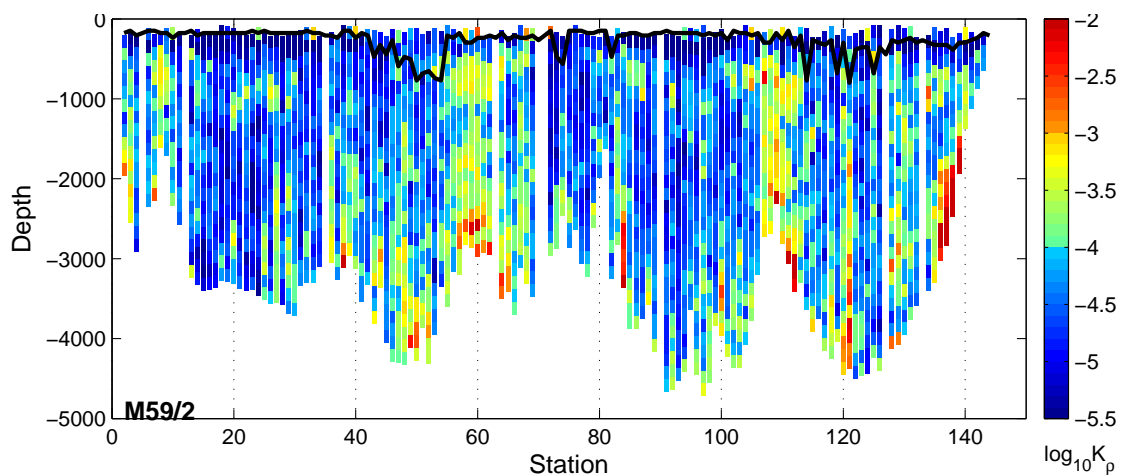
Observations

With the variances of strain and horizontal velocity shear, the diapycnal diffusivity of our measurements in the subpolar North Atlantic is calculated accordingly using Eq. (3.7). As is shown by the parameterization, K_ρ in this region is generally larger than the background diffusivity $O(10^{-5} \text{ m}^2 \text{ s}^{-1})$ for the open ocean and varies with regions and depths.

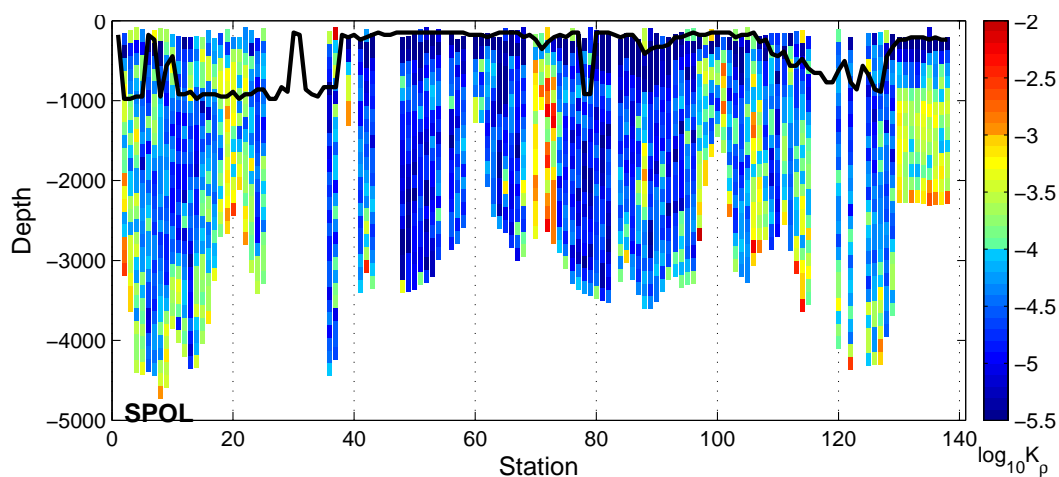
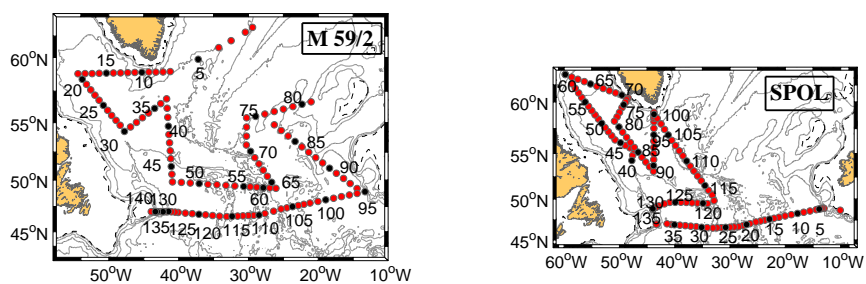
4.1 Estimations of diapycnal diffusivity

To get a direct impression, estimations of K_ρ in each sub-profile of all nine cruises are listed first. In the analysis, K_ρ is computed for each 320 m half-overlapped vertical bins in available profiles. The results are shown in Fig. 4.1. K_ρ of each cruise is plotted along the track, i.e. station by station; the overlapped sub-profiles are displayed as adjacent vertical bars. For convenience, the boxes of sub-profiles are displayed as 160 m long in vertical direction in the figure, centered at their actual central depths. K_ρ is plotted according to their logarithm as shown by the colorbar in Fig. 4.1, ranging from $10^{-5.5}$ to $10^{-2} \text{ m}^2 \text{ s}^{-1}$ with step length of $10^{0.1} \text{ m}^2 \text{ s}^{-1}$, values out of this range are shown as boundary values accordingly for convenience. Note that the following figures displaying K_ρ shares the same colorbar.

4. OBSERVATIONS



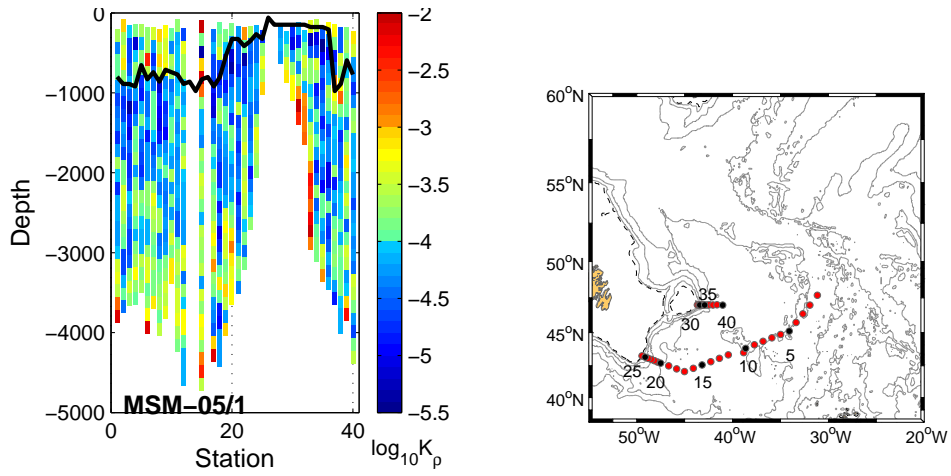
(a) cruise M59/2



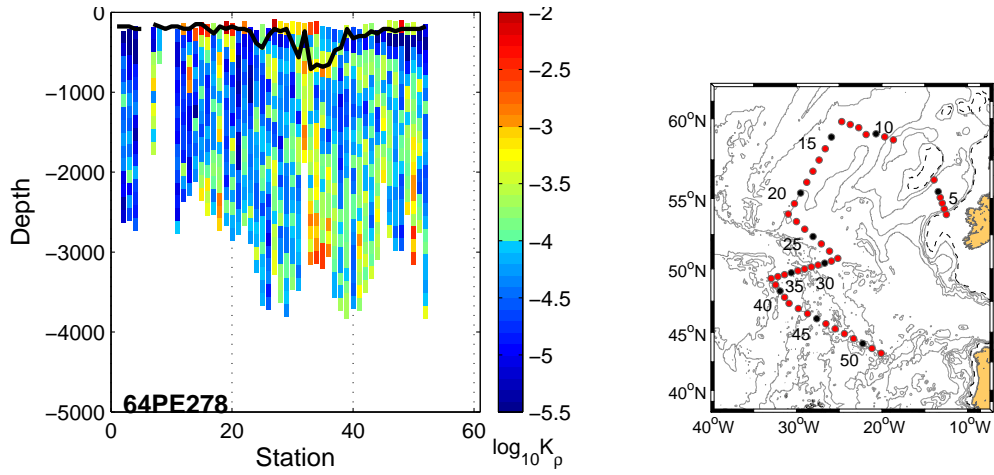
(b) cruise SUBPOLAR

Figure 4.1: K_p estimates in sub-profiles along each cruise track. Black lines denote the lower boundary of mixed layer.

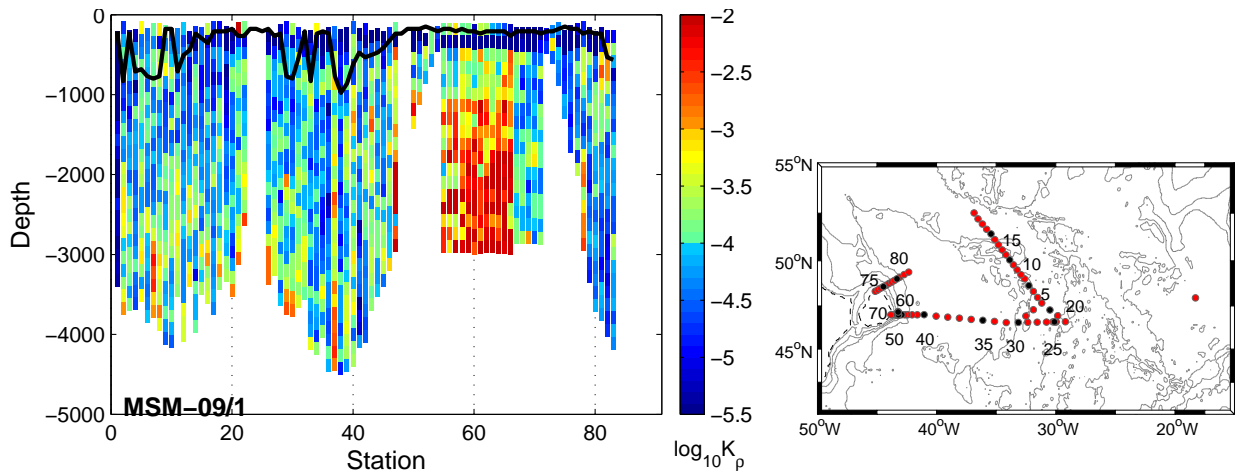
4. OBSERVATIONS



(c) cruise MSM-05/1



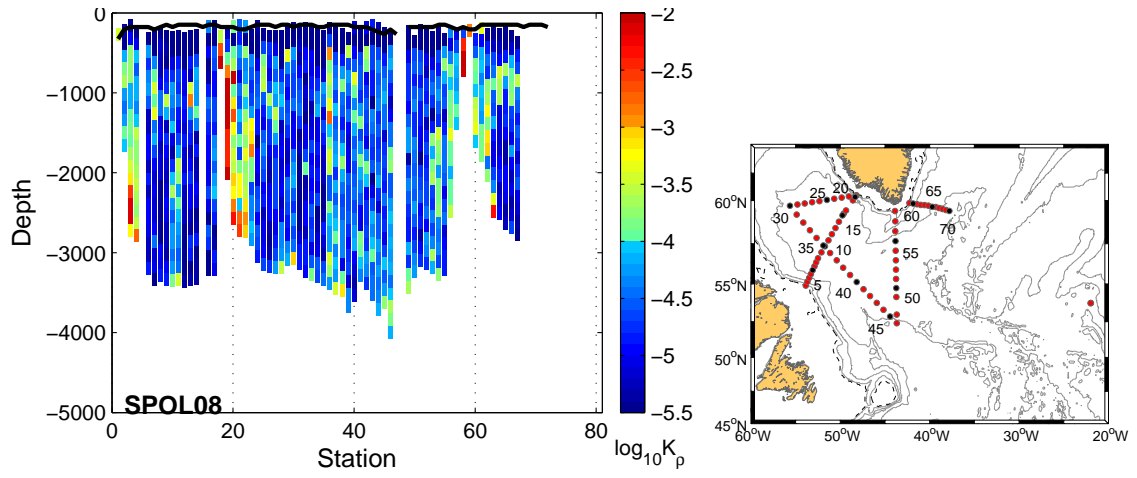
(d) cruise 64PE278



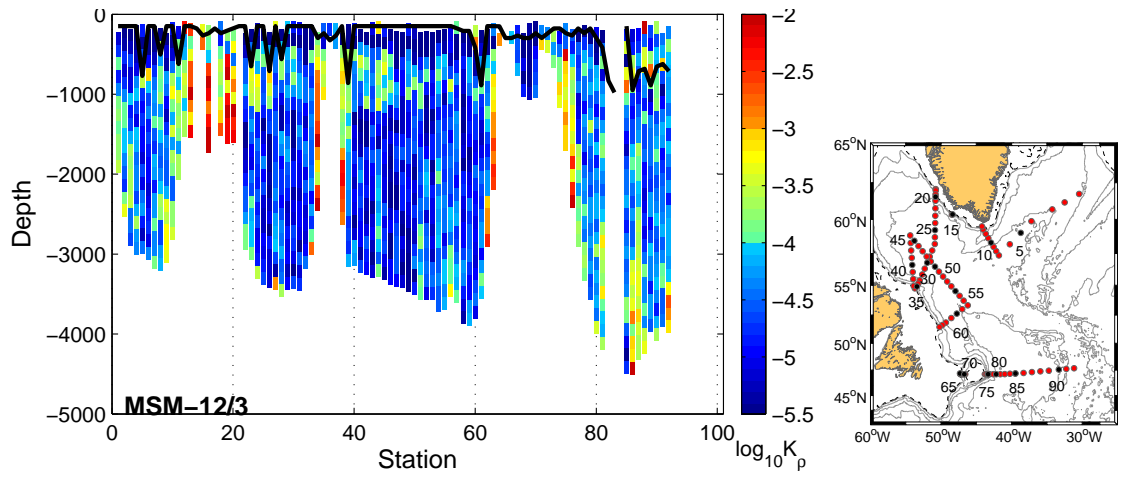
(e) cruise MSM-09/1

Figure 4.1: (continued)

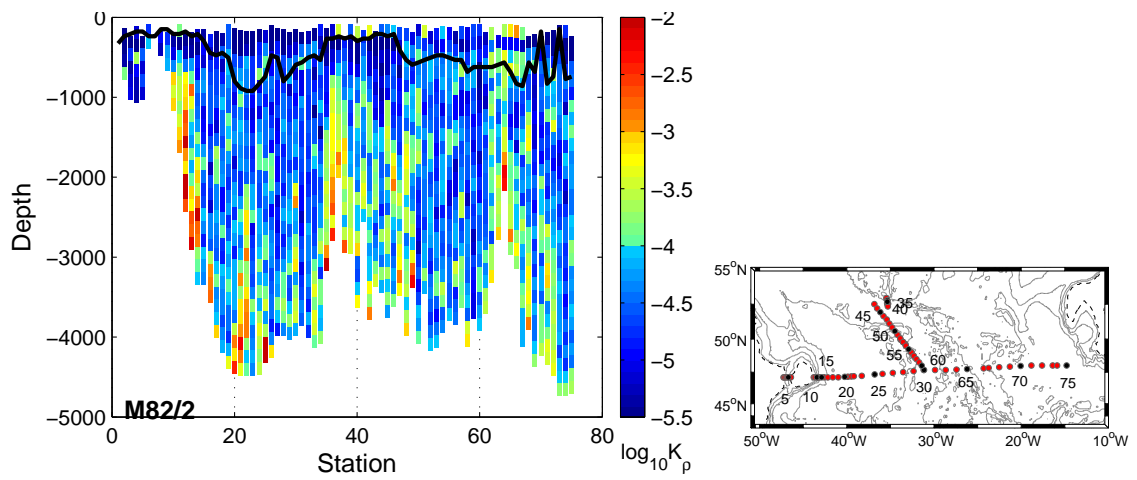
4. OBSERVATIONS



(f) cruise SUBPOLAR08



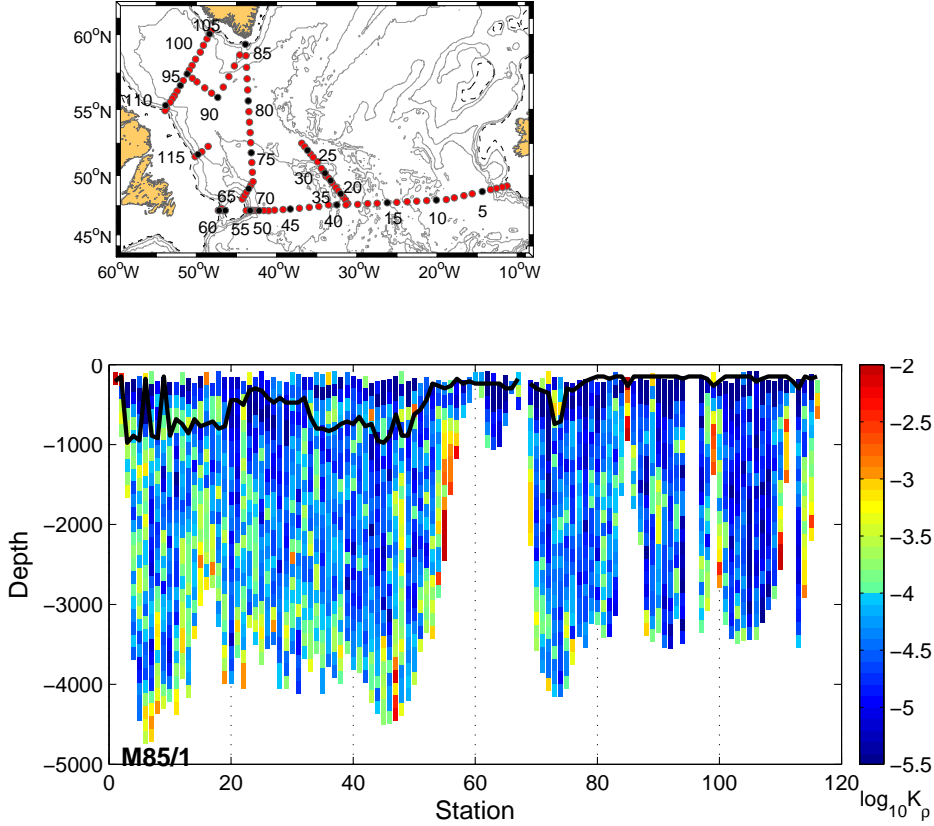
(g) cruise MSM-12/3



(h) cruise M82/2

Figure 4.1: (continued)

4. OBSERVATIONS



(i) cruise M85/1

Figure 4.1: (continued)

The diapycnal diffusivities shown in Fig. 4.1 are all the original estimates of each sub-profiles. K_ρ close to the background value of $O(10^{-5}) \text{ m}^2 \text{ s}^{-1}$ can be seen in the Labrador Sea (e.g. station (stn.) 50 - 65 in Fig. 4.1b; stn. 25 - 35 in Fig. 4.2f), mostly in the whole water column over plain topography (e.g. stn. 55 - 60 in Fig. 4.2g) and in the intermediate layer with large water depth (e.g. stn. 85 - 100 in Fig. 4.1a). Enhancement of K_ρ with one or two magnitudes can be seen in the lowest sub-profiles when the topography varies frequently; it is more obvious in linear sections (e.g. stn. 110 - 140 in Fig. 4.1a; stn. 5 - 20 in Fig. 4.1b). Strong mixing appears at boundary region with high values exceeding $10^{-3} \text{ m}^2 \text{ s}^{-1}$ (e.g. Fig. 4.2c, stn. 30 - 35). Note that stn. 55 - 66 were yoyo stations, so the high values of K_ρ actually correspond to stations at one location. Besides, K_ρ in the east basin is generally smaller

than that in the Newfoundland Basin.

The adjacent sub-profiles in the same profile can differ as large as one order of magnitude. The high variations may be due to the spikes in the observations of density field from which the strains are computed, which is unavoidable. Moreover, in regions with weak stratification and energetic regimes, the computed diffusivity may be overestimated since the actual mixing is not that efficient as supposed by the parameterization (3.7) as indicated in section 3.2.4. The sharp density changes may contaminate the strain and consequently the estimates of diapycnal diffusivity. In the following analysis, only sub-profiles under the mixed layer are considered.

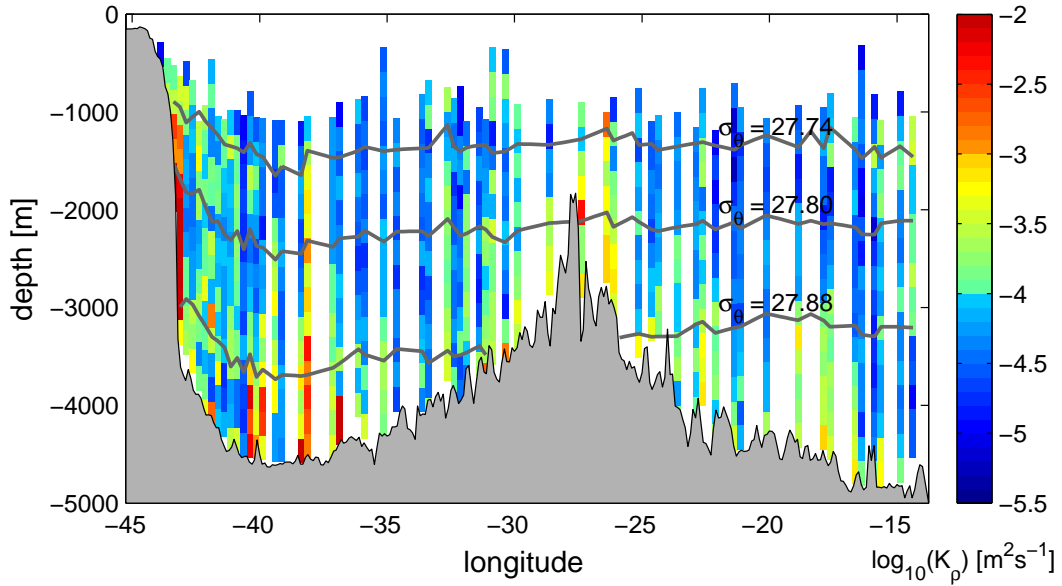
4.2 Structures of diffusivity in 2 vertical sections

In the subpolar region of the North Atlantic, K_ρ in this study is generally larger than the background diffusivity $O(10^{-5} \text{ m}^2 \text{ s}^{-1})$ for the open ocean. It varies with regions and depths. In Figure 4.2, the distributions of K_ρ along two vertical sections are displayed to verify the magnitude and variability of K_ρ . The terrain shown by gray shadings in Fig. 4.2 is based on the 1-minute ETOPO database (from U.S. National Geophysical Data Center). The locations of these two sections are shown by gray shading in Figure 3.2.

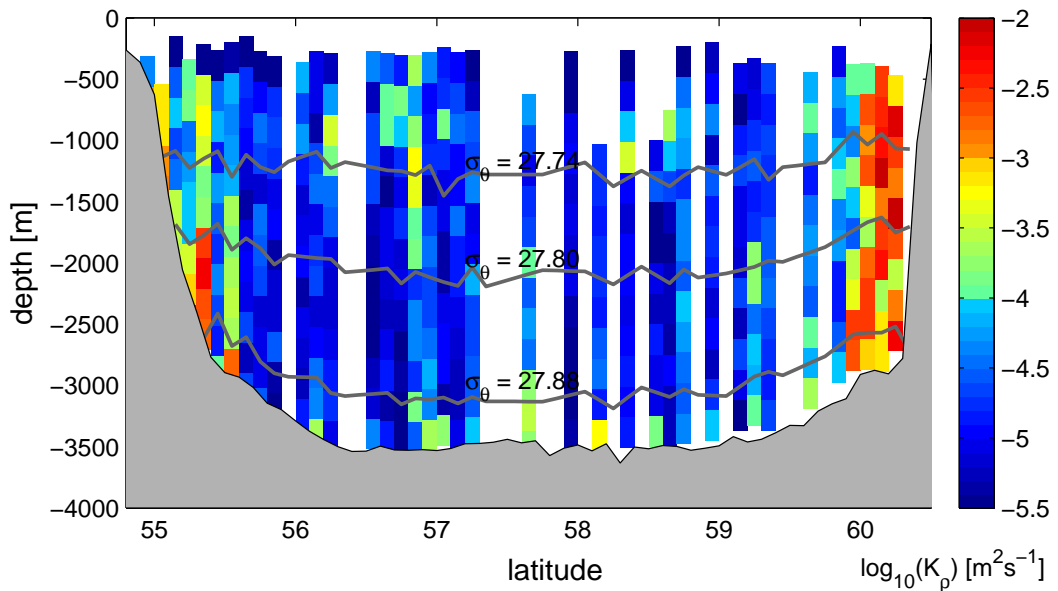
The transatlantic section a (Fig. 4.2a) is along 47°N , starting from the Flemish Cap at the western edge, across the Mid-Atlantic Ridge to round 12°W . All profiles within 1° of this section were firstly binned into 0.25° longitude sub-sections and then averaged into 250m adjacent boxes from bottom to top in the vertical direction. The average is under the assumption of a steady state, that is, K_ρ varies only spatially, but not temporally. Walter *et al.* (2005) also estimated diffusivities using the similar parameterization to this work, but with only measurements during single cruise (M59/2). They derived a vertical structure of K_ρ along transatlantic section at 48°N (their Fig. 2), close to section a in this work. The average of K_ρ over cruises in this work shows a similar pattern to that from the single cruise: diffusivity near the seafloor is enhanced by one or two orders of magnitude compared to higher up in the water column, especially over strongly varying topography such as the MAR; in the western boundary region, around the core of the energetic North Atlantic Current (NAC) and Deep Western Boundary Current (DWBC), K_ρ is significantly enhanced throughout the whole water column with high values exceeding $10^{-3} \text{ m}^2 \text{ s}^{-1}$. But the thickness of the layer with $K_\rho > 10^{-4} \text{ m}^2 \text{ s}^{-1}$ is slightly different from that from Walter *et al.* (2005): it is around 750m in both western and eastern basins and could reach 1000 - 2000 m over the MAR, thinner than that suggested by Walter *et al.* (2005) in the eastern basin. The values of K_ρ at lowest part in the eastern basin is around one order of magnitude smaller than the estimate of Walter *et al.* (2005).

Section b (Fig. 4.2b) is across the Labrador Sea from southwest to northeast, including all stations within 1° away from the central line in the east-west direction. K_ρ is averaged similar to section a, but with 0.1° intervals of sub-section. Along the Labrador Sea section, the terrain change is smoother than the trans-Atlantic section; K_ρ away from the boundaries generally varies between $10^{-5} \text{ m}^2 \text{ s}^{-1}$ and $10^{-4} \text{ m}^2 \text{ s}^{-1}$. Enhancement is found mainly over the continental slopes. High values of $O(10^{-3}) \text{ m}^2 \text{ s}^{-1}$ are observed throughout the whole water column at the northeast end of this section, where the West Greenland Current flows through the southmost point of Greenland into Labrador Sea. The magnitude of K_ρ at around 60°N , 49°W (the right end in Fig. 4.2b) is the same as the estimation by Stöber *et al.* (2008, their Fig. 4f) inferred also from CTD/LADCP measurements. Strong mixing is also found at depth at the southwest end of section b, where deep Labrador current flows southeastward along the Grand Bank of Newfoundland, and decays upward.

4. OBSERVATIONS



(a) along 47°N (plotted in the east - west direction)



(b) Labrador Sea section (plotted in the north - south direction)

Figure 4.2: The vertical distribution of the diapycnal diffusivity. K_p shown here is below the pycnocline. Gray lines indicate the depths of isopycnals defined by $\sigma_\theta = 27.74, 27.80$ and 27.88 .

4.3 Horizontal distribution of diffusivity

To examine the horizontal distribution of diapycnal diffusivity, K_ρ estimated from shear variance was mapped onto three isopycnal surfaces and the seafloor boundary (Figure 4.3). Isopycnal surfaces rather than depth levels were chosen corresponding to the interfaces between the main constituents of North Atlantic Deep Water (NADW), to estimate the transformation rates between different water masses. To be strict, the isopycnal surfaces should be a layer with identical neutral density of water, but the potential densities were used as an indicator instead. The computation was simplified but the resulting depths of isopycnal surfaces are similar to those inferred from neutral densities. The selected surfaces with potential density $\sigma_\theta = 27.74, 27.80, 28.88$ kg m^{-3} are the consequent interfaces between the upper Labrador Sea Water (uLSW), the classical Labrador Sea Water (LSW), the Gibbs Fracture Zone Water (GFZW) and the Denmark Strait Overflow Water (DSOW) respectively (following Stramma *et al.*, 2004). The depths of isopycnal surfaces were derived from the density field observed by CTD. The sub-profiles with central depths closest to the inferred values were selected and estimates of K_ρ of these sub-profiles were used as diffusivity on the isopycnal surfaces. Similar work was done by Walter *et al.* (2005), but with only CTD/LADCP measurements during cruise M59/2. The distribution over the seafloor was derived from the estimates of subprofiles centered within 250 m to the bottom. Diffusivity values in all profiles were binned into $1^\circ \times 1^\circ$ boxes and averaged separately. The mean values on the intermediate interfaces are shown in Table 5.1.

At locations with water depths less than 1000 m, high values exceeding 10^{-3} $\text{m}^2 \text{s}^{-1}$ are detected in shallow layer, such as offshore of southwest Greenland, to the east of Flemish Cap, over Mid Atlantic Ridge (Fig. 4.3a). Depths of different isopycnal surfaces at these locations may be in the same sub-profile (i.e. the deviation in between is less than 320 m), thus estimates of K_ρ on different isopycnals share the same values. In the upper layer, the isopycnal surface $\sigma_\theta = 27.74$ kg m^{-3} overlaps partially with the mixed layer, resulting in some large values. For instance in the box at around (57°N , 41°W), the

4. OBSERVATIONS

water depths is about 3500m, and the mean values of K_ρ on $\sigma_\theta = 27.74 \text{ kg m}^{-3}$ is obviously larger than that on the lower layers. This is due to the contamination by sharp density changes below the mixed layer. K_ρ in the box at around (47°N, 40°W) on $\sigma_\theta = 27.74 \text{ kg m}^{-3}$ is much higher than the surroundings, it was also found in the work of Walter *et al.* (2005). This location is on the pathway of North Atlantic Current, therefore it should be influenced by the surface current.

In the deep layers, K_ρ generally increases with depth. The depths of isopycnal surface $\sigma_\theta = 27.80 \text{ kg m}^{-3}$ are generally around 2500m in abyssal ocean (water depth exceeding 4000m), much shallower at ocean boundaries, reaching the bottom over the MAR, and around 2000m in the Labrador Sea. This can also be seen in Fig. 4.2, where the gray lines indicate the depth of isopycnal surfaces in two typical sections. Diffusivity in the inner Labrador Sea on this layer is in the magnitude of $O(10^{-5} \text{ m}^2 \text{ s}^{-1})$ (Fig. 4.3b). Enhancement of 1-2 orders of magnitude can be found near the western boundary, over the MAR and to the south of Greenland. Similar pattern of distribution was supposed from modal estimation due to the tidal energy dissipation and eddy energy dissipation by Saenko *et al.* (2012) at around 2200m, but estimation from hydrographic observations in this work shows larger values over MAR and at boundary regions.

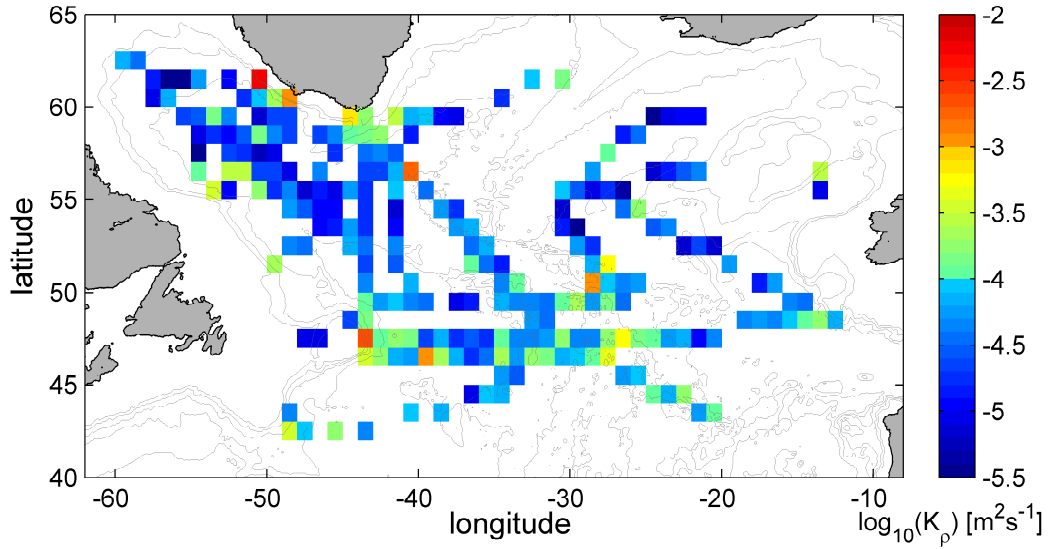
The isopycnal surface $\sigma_\theta = 27.88 \text{ kg m}^{-3}$ overlaps with the bottom layer (within 250m over the seafloor) in some areas, especially nearby the MAR. So the boxes with K_ρ estimates on $\sigma_\theta = 27.88 \text{ kg m}^{-3}$ (Fig. 4.4c) are less than that over the seafloor (Fig. 4.4d). K_ρ along the western boundary, from south of Flemish Cap to around 56°N, is enhanced in and near the core of the DWBC. The values in the Newfoundland basin and east basin are comparable to those of Walter *et al.* (2005), but K_ρ in the inner Labrador Sea in this work is around one magnitude smaller. A hot spot appears at around (54°N, 25°W), observed only in cruise M59/2. The buoyancy frequency is checked at corresponding stations, and the stratification at depth of $\sigma_\theta = 27.88 \text{ kg m}^{-3}$ (around 3200m deep) is extremely weak. The average of K_ρ in this box may be dominated by the high diffusivity value at one station. The mean values of

4. OBSERVATIONS

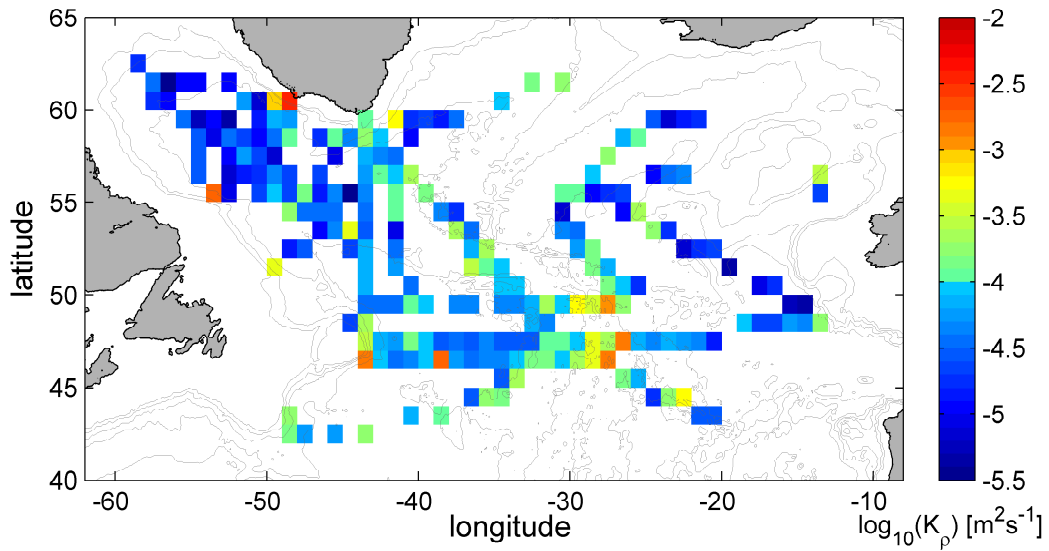
K_ρ over the whole interfaces of $\sigma_\theta = 27.80, 27.88 \text{ kg m}^{-3}$ are listed in the table 5.1 in Section 5.4.

Bottom K_ρ (referred to as K_b in the following), is universally high (Fig. 4.4d). The mean value over the bottom is $(1.0 \pm 0.3) \times 10^{-3} \text{ m}^2 \text{ s}^{-1}$, one order of magnitude than the average value estimated by Kunze *et al.* (2006, their Fig. 15) referring from WOCE legs in the Atlantic; the median value also reaches $1.7 \times 10^{-4} \text{ m}^2 \text{ s}^{-1}$. The elevations seems to be more prominent over rough terrain. The magnitudes and spatial distribution of K_ρ is similar to the prediction by Decloedt and Luther (2010) obtained from their roughness diffusivity model (their Fig. 7, bottom), denoting great possibility of its dependence on the roughness of underlied bottom. The correlation between the seafloor roughness and the magnitude of K_b is further discussed later in section 5.2.1.

4. OBSERVATIONS



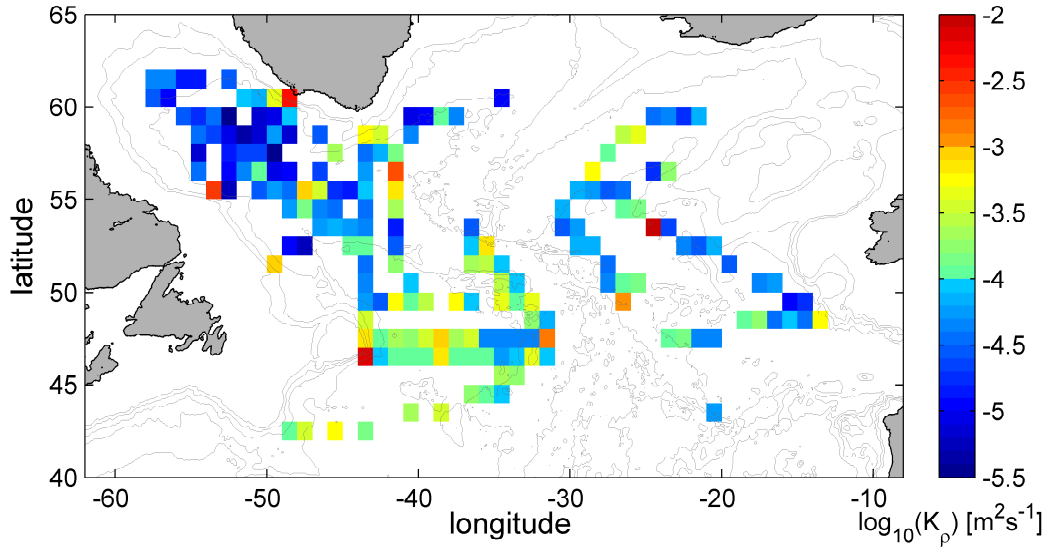
(a) Spatial distribution of K_ρ on isopycnal surface $\sigma_\theta = 27.74 \text{ kg m}^{-3}$



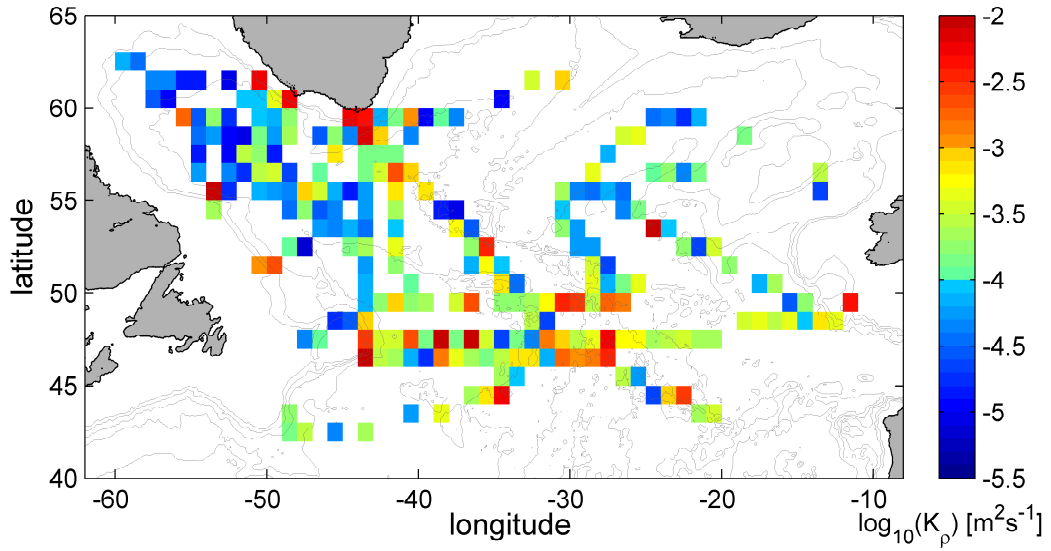
(b) Same as Fig. 4.3a, but on isopycnal surface $\sigma_\theta = 27.80 \text{ kg m}^{-3}$

Figure 4.3

4. OBSERVATIONS



(c) Same as Fig. 4.3a, but on isopycnal surface $\sigma_\theta = 27.88 \text{ kg m}^{-3}$



(d) K_ρ over seafloor

Figure 4.3: (continued)

Chapter 5

Discussion

5.1 Distribution of diffusivities

Estimations of K_ρ in the subpolar North Atlantic were shown along two vertical sections (in section 4.2) and on isopycnal surfaces corresponding to interfaces between major components of NADW (in section 4.3). As shown in relative figures, the strength of K_ρ varies distinctively with hydrographic and bathymetric conditions. Small diffusivities in the magnitude of $O(10^{-5}) \text{ m}^2 \text{ s}^{-1}$ are found in most water column in the Labrador Sea, except for the lowest layer close to the seafloor and over slope in the boundary regions. K_ρ in the surface layer of the Labrador Sea in this work is about one magnitude smaller than the estimations by Walter *et al.* (2005, upper figure of their Fig. 1) similar to this work and by Whalen *et al.* (2012, their Fig. 2a, 2b) inferred from argo float records. The difference is mainly because that we exclude estimations above the lower boundary of mixed layer where the sharpe change of density field results in small shear/strain variance ratio and consequently anomalous large diffusivity according to the fine-scale parameterization. Diffusivity below the Labrador Sea water layer at mid depth varies mainly between 10^{-5} and $10^{-4} \text{ m}^2 \text{ s}^{-1}$, similar to the result of Walter *et al.* (2005, middle one of their Fig. 1).

High values exceeding $10^{-4} \text{ m}^2 \text{ s}^{-1}$ can be seen everywhere close to the rough topography. Former estimations of abyssal diffusivity in large scale of the North Atlantic were quite few. Bottom diffusivity K_b offshore of southern

Greenland is comparable with the average value of K_ρ over the deepest 500m estimated with constant shear/strain ratio by Lauderdale and Bacon (2008, their Fig. 1); K_b in east basin is slightly larger than the estimate of Kunze *et al.* (2006, their Fig. 11). The overall pattern of K_b is similar to the distribution in abyssal layer given by Walter *et al.* (2005). Strong mixing at the mid-depth mainly concentrate in several regions: to the south of Greenland, over the Mid-Atlantic Ridge, at the western boundary (Fig. 4.3b, 4.4c). Hot spots exceeding $10^{-3} \text{ m}^2 \text{ s}^{-1}$ are found in these regions. The possible reasons of these high values are discussed in the following section.

5.2 Possible mechanisms of the enhanced mixing

The strength of turbulent diffusivity was supposed to be dependent on environmental parameters, such as latitude (Garrett, 2003; Hibiya and Nagawasa, 2004), rough topography (e.g. Kunze and Toole, 1997; Ledwell *et al.*, 2000; St.Laurent *et al.*, 2001), barotropic tides (e.g. Garrett and St. Laurent, 2002; Simmons *et al.*, 2004; Garrett and Kunze, 2007), geostrophic flows (e.g. Lauderdale and Bacon, 2008; Nikurashin and Ferrari, 2010a) and meso-scale eddies (e.g. Gnanadesikan, 1999; Marshall and Garabato, 2008; Polzin, 2008). The possible sources of the enhanced mixing in the research area are examined in this section. Since the latitudinal dependence of K_ρ has already been included in the parameterization 3.7, the latitudinal correction term $j(f, N)$ are removed in regional average to exclude the related effect.

5.2.1 Rough topography

The bathymetry in the northern North Atlantic is rougher than other oceans, K_ρ around $O(10^{-4} \text{ m}^2 \text{ s}^{-1})$ and higher is found everywhere in deep layers (Fig. 4.4c, 4.4d), especially over the MAR and boundary regions where the terrain varies rapidly. Internal tides are generated when barotropic tides flow

over the steep topography and radiate away (Simmons et al. 2004); energy is transferred to small scales via the subsequent instability or breaking or non-linear wave-wave interaction (see section 2.3). High values near the seafloor are mainly because of the interaction with topography. Internal tides have also been found over gentle topography, however, direct measurements of internal tides are concentrated on abrupt topography (Garrett and Kunze, 2007).

Recent studies generally agree that the level of the enhancement of diapycnal mixing close to the seafloor relies on the roughness of terrain; the functional dependence is presumed to be exponential (Kunze *et al.*, 2006) or high order polynomial (Declodt and Luther, 2010). To investigate the relationship between bottom roughness and diffusivity in the area of interest, the bottom diffusivity K_b is compared with the seafloor roughness $r(H)$. Here K_b is the diffusivity in lowest bin of each profile and $r(H)$ is simply defined as the standard deviation of seafloor height H within 32×32 km² square boxes (around 11% area of a $1^\circ \times 1^\circ$ box at 45° N) surrounding the locations of each profile. The square boxes instead of boxes framed by meridian and parallel lines are used to keep the ranges identical for each profile and the specific value is following the work of Kunze *et al.* (2006). The seafloor height used in this work is from Smith and Sandwell's 1-minute topography data (<http://topex.ucsd.edu/>).

A scatter plot between K_b and $r(H)$ is displayed in Fig. 5.1. To eliminate the influence of latitude, K_b was normalized by the latitudinal correction function $j(f, N)$ (Eq. 3.3). Extremely large values ($> 10^{-1}$ m² s⁻¹) were ignored as outliers; consequently, 654 profiles are inspected.

If only the influence of roughness is considered, an empirical fit could be made for K_b :

$$K_b = K_{b0} \left[\frac{r(H)}{r_0(H)} \right]^a \times j(f, N) \quad (5.1)$$

Here $r_0(H)$ is an assigned value of the median roughness for dimensional consistency, $K_{b0} = 9.6 \times 10^{-5}$ m² s⁻¹, $a = 0.95$. The form of empirical fit chosen in this work draws on the experience of Kunze *et al.* (2006): the latitudinal

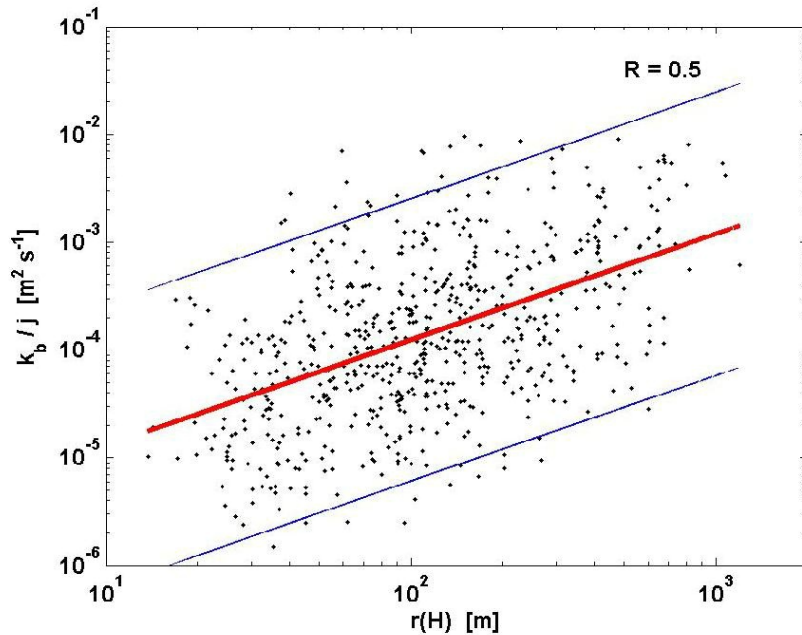


Figure 5.1: Bottom diffusivity K_b versus local seafloor roughness $r(H)$. K_b is scaled by the latitudinal correction term, j -function. The red line indicates an empirical fit; blue lines confine the 95% confidence intervals of the fit. The correlation coefficient between K_b/j and $r(H)$ is $R = 0.5$.

dependence is listed separately, and K_b is treated to increase exponentially with normalized seafloor roughness, but the tidal term and height dependence are not considered here. The coefficient a is about twice as large as than from Kunze *et al.* (note $\text{var}(H) = [r(H)]^2$), indicating a higher dependence of K_b on seafloor roughness from our estimation. Decloedt and Luther (2010) also supposed a fit between K_b and $r(H)$, but it is twofold: for small roughness, K_b obeys a least-squares third-order polynomial fit of $r(H)$; for large roughness, K_b remains constant with a value of $1.8 \times 10^{-3} \text{ m}^2 \text{ s}^{-1}$. But according to the analysis in this work, K_b over topography of large roughness varies over 2 orders of magnitude. In general, the rougher the seafloor, the higher the diffusivity. Normalized K_b increases with $r(H)$ nearly linear, as shown in Eq. 5.1. The correlation coefficient between these two variables is 0.5, thus the dependent relationship can be considered to be significant.

In the whole water column, the influence of seafloor roughness is most

5. DISCUSSION

obvious near the bottom, as is already self-evident in the figures of horizontal distribution and vertical sections of K_ρ . On the other hand, the influence of rough bottom could stretch several hundreds or even thousand of meters above the seafloor. The vertical structure of K_ρ is further discussed in section 5.3.

5.2.2 Geostrophic currents

The estimation of diapycnal diffusivity at the intermediate depth (on the isopycnal surface of $\sigma_\theta = 27.80 \text{ kg m}^{-3}$) was overlapped to the map of major currents in the subpolar North Atlantic (Fig. 5.2). High values of diffusivity exceeding $10^{-3} \text{ m}^2 \text{ s}^{-1}$ are observed in the boundary current regions, for instance, off Flemish Cap (around 47°N , 43°W , Fig. 4.2a) near the core of North Atlantic Current (NAC) and Deep North Atlantic Current; south of Greenland (Fig. 4.4c, 4.4d), in the route of East Greenland Current (EGC) and West Greenland Current (WGC); in the core of Labrador Current off shore of Labrador and Newfoundland.

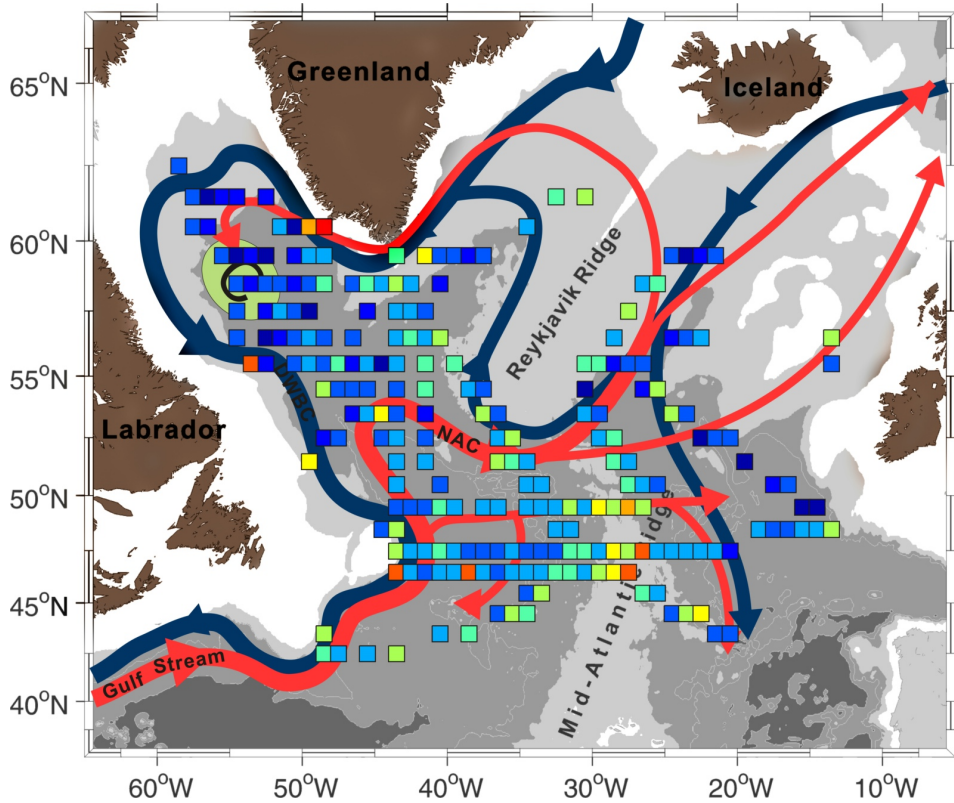


Figure 5.2: Combination of K_ρ on isopycnal surface of $\sigma_\theta = 27.80 \text{ kg m}^{-3}$ (colored boxes) and major currents in the subpolar North Atlantic. The illustration of currents is based on the diagram of Rhein *et al.* (2011); the colorbar of K_ρ is the same as Fig. 4.3.

5. DISCUSSION

These currents are quite strong: the horizontal velocity can reach up to 1 m s^{-1} in the core of DWBC; current speed of Labrador Current is about $0.3\text{-}0.5 \text{ m s}^{-1}$ (Reynaud *et al.*, 1995); the inter-annual maximum of EGC is $0.2\text{-}0.3 \text{ m s}^{-1}$ (Dickson and Brown, 1994). As a matter of course, people may wonder, is it the shear instability that causes the elevation of diffusivity in these areas?

The Kelvin-Helmholtz instability (shear instability) seems to be a reasonable candidate. It can arise when there is velocity shear in continuous fluid, i.e., is driven by sheared flows, where small-scale perturbations draw kinetic energy from the mean flow. However, a necessary condition for velocity shear to overcome the tendency of a stratified fluid to remain stratified and trigger turbulence mixing is that the bulk Richardson number $Ri = N^2/(du/dz)^2 < 0.25$. Otherwise the turbulent mixing across the stratification is generally suppressed. The buoyancy frequencies in the current regions mentioned above are generally $O(10^{-6}) \text{ s}^2$, therefore the velocity shear should at least larger than $2 \times 10^{-3} \text{ s}^{-1}$. According to the LADCP measurements, the velocity shear is way too small. For instance, to the east of Flemish Cap, one of the strongest site of DWBC, the velocity shear is generally in the magnitude of $O(10^{-4})\text{s}^{-1}$. It can reach to $1 \times 10^{-3} \text{ s}^{-1}$ close to the core of DWBC, but are not strong enough for the frequent occurrence of shear instability.

The enhancement of K_ρ along routines of the boundary currents may due to the interaction of currents with small scale topography. Nikurashin and Ferrari (2010a) showed in their theoretical study that internal waves generate when geostrophic currents flow over bottom topography and radiate away in the form of lee waves; meanwhile, the feedback of internal waves on the geostrophic flows generate inertial oscillations close to the topography. Both result in enhanced wave breaking and vertical mixing. They applied the linear lee wave theory to the southeast Pacific and showed great consistency of energy flux into lee waves and associated mixing with observations (Nikurashin and Ferrari, 2010b). Internal waves generated by geostrophic flows can be considered as an alternative mechanism to support enhanced abyssal mixing (Nikurashin and Ferrari, 2010a).

5.2.3 Eddies

In mid- and high latitudes, geostrophic eddies are thought to dominant the kinetic energy (Ferrari and Wunsch 2009). It is suggested by Polzin (2008) that wave-eddy coupling is a significant source of internal wave energy. He pointed out that the internal waves with growing horizontal and vertical wavenumber magnitude tend to be captured within eddy strain field and eventually dissipate. Energy exchanges between internal wavefield and mesoscale eddy field were estimated by Brown and Owens (1981). According to the analysis of Saenko *et al.* (2012) based on ocean general circulation models (OGCMs), tidal energy dissipation could lead to diffusivities up to $2 \times 10^{-3} \text{ m}^2 \text{ s}^{-1}$ at boundary regions. The energy transferred to the internal wave fields from the meso-scale eddies is likely to be another candidate for the enhanced dissipation and diapycnal mixing (Saenko *et al.*, 2012).

To infer the possible connection with eddies, the depth-integrated energy dissipation rate is compared with the eddy kinetic energy. The integrated dissipation $E = \rho_0 \int_{-H}^{z_0} \varepsilon(z) dz$ was computed through the whole water column. Here $\rho_0 = 1027$, kg m^{-3} ε was first averaged in $1^\circ \times 1^\circ$ boxes and integrated correspondingly from bottom (H is water depth) to the upper limit $z_0 = -250$ m to exclude the mixed layer. The eddy kinetic energy (EKE) was computed following Gille et al. 2000: $E_k = \langle \vec{v}^2 \rangle$, where \vec{v} is the geostrophic horizontal velocity derived from altimeter product - Maps of Sea Level Anomalies (MSLA, <http://www.aviso.oceanobs.com/en/>) using the geostrophic relation:

$$\langle \vec{v}^2 \rangle = \frac{g^2}{f^2} \langle (\nabla \eta)^2 \rangle \quad (5.2)$$

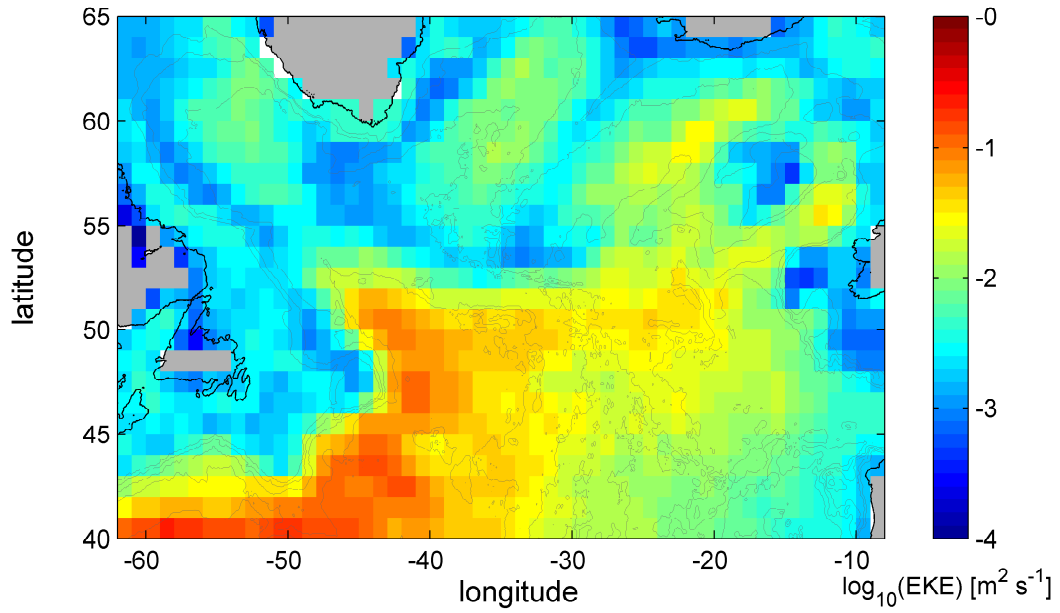
where g is local gravity, η is the sea surface height, $(\nabla \bullet)$ the horizontal gradient in a Cartesian coordinate system, $\langle \bullet \rangle$ denotes the spatial average in $1^\circ \times 1^\circ$ boxes. The data of sea surface height used here are combined from up to four satellites at a given time (*Jason-2/ Jason-1/ Envisat* from 2009 or between October 2002 and September 2005, the association *Jason-1/ Topex/Poseidon/ ENVISAT/ GFO*) with frequency of 6 months, and are computed with respect to a seven-year mean. Since the cruises were carried out in several years, the dataset of η is from the up-to date dataset between 2003 and 2011. $\nabla \eta$

was computed for each data point and the time-mean was removed, then the time variance was computed. Data are low-pass filtered to eliminate high-wavenumbers. Then we compute the median variance in boxes. Note that the E_k computed here is a scaling of energy rather than a precise estimate (5.3a).

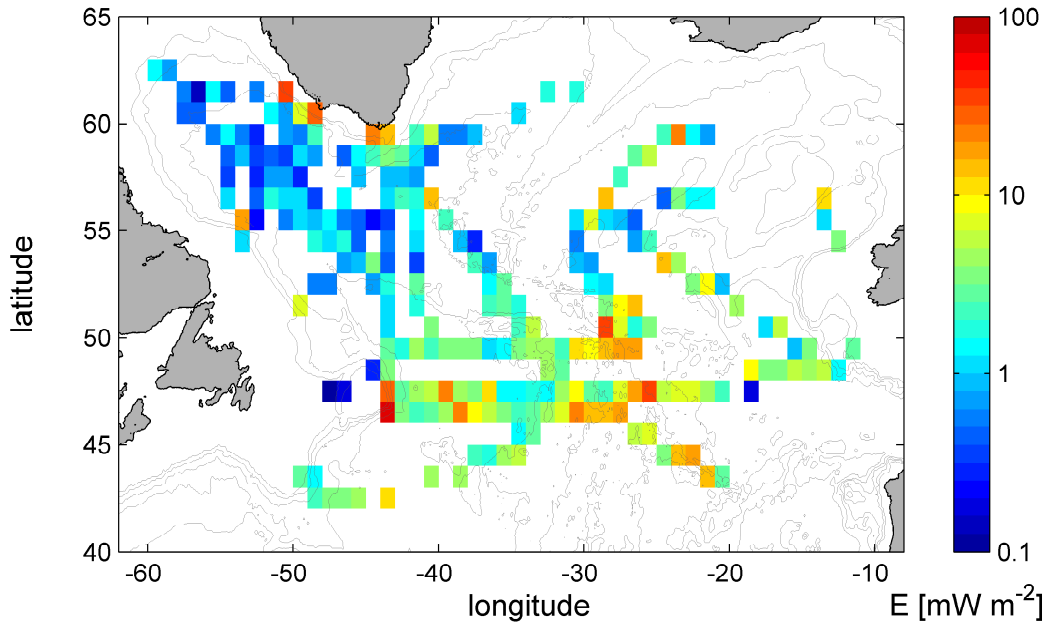
The geostrophic eddy field arises from the instability of the strong, large-scale North Atlantic Current, close to which the energy level of eddies tends to be highest. For instance, to the east of Newfoundland, and around the Charlie-Gibbs Fracture Zone. The vigorous EKE in the southern part of the research area is coinciding with the elevated depth-integrated dissipation rate. The intense mesoscale eddy energy could be another cause of the elevated diffusivity values, especially in mid-depth ocean.

Although the estimations of dissipation rate are relatively sparse, a qualitative agreement between the horizontal distributions of E_k (Fig. 5.3a) and E (Fig. 5.3b) can be observed. To make it more discernible, the integrated dissipation rate is binned with respect to EKE and seafloor roughness (Fig. 5.4) as Whalen *et al.* (2012, their Fig. 3d). Instead of their usage of median values between 250m-1000m as dissipation levels, we applied the integration of dissipation rate of the whole water column in this work. It plays a similar role in representing the strength of dissipation and mixing, but demonstrates the energy loss in the whole depth. As is found by Whalen *et al.*, a trend shows that the integrated dissipation rate E increases with both the increase of seafloor roughness and that of the EKE. It is clear that the rough terrain plays a substantial role in elevating the local energy dissipation; for locations with extremely rough seafloor, mixing is dominated by the terrain.

5. DISCUSSION



(a) Eddy kinetic energy E_k



(b) Integrated energy dissipation rates E over whole water columns, averaged in $1^\circ \times 1^\circ$ boxes.

Figure 5.3

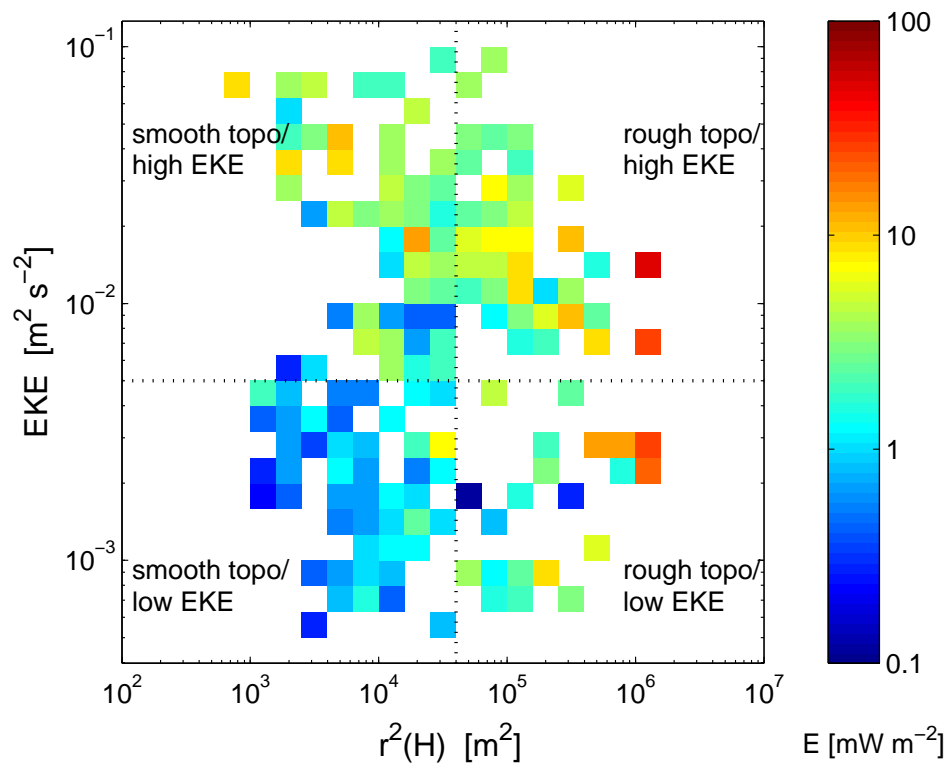


Figure 5.4: Dissipation rate integrated over the whole water column varied with seafloor roughness and eddy kinetic energy.

5.3 Vertical structure of K_ρ and shear/strain variance ratio

The study of vertical structure of diapycnal diffusivity is essential for model assimilation. In practice, K_ρ is often set to decay exponentially from the bottom upward (e.g. St. Laurent *et al.*, 2002; Simmons *et al.*, 2004; Saenko *et al.*, 2012), however, the vertical distribution of K_ρ is not identical everywhere in the global ocean. The bathymetry of world ocean is heterogeneous, likewise the hydrographic and meteorologic conditions are quite diverse, therefore it is impossible to infer a general distribution for global ocean. Nevertheless, we can examine the variations in an averaged sense for comparison with that used in the models and further modification and consumption. In this work, the whole region of the subpolar North Atlantic is separated into four regions (blue shading in Fig. 3.2); the vertical structures of K_ρ and ε are studied separately and then as a entity.

Mean values of K_ρ , R_ω , N^2 and ε at different depths over each region (Fig. 5.5) and the entire area of interest (Fig. 5.7) are calculated in every $1^\circ \times 1^\circ$ box and then averaged horizontally according to the height above seafloor h into 250 m adjacent vertical boxes. The buoyancy frequency generally increases with the height above seafloor (Fig. 5.7c), but the stratification varies from region to region. The maximum of N^2 in the Labrador Sea appears in the intermediate layer, and that in the Irminger Sea decreases somehow just over the seafloor. The dissipation rate in the Labrador Sea varies between $10^{-10} - 10^{-9} \text{ W kg}^{-1}$, decreases from the bottom into the intermediate layer and then increases somehow until the surface. The vertical structure of diapycnal diffusivity, which is affected by both the pattern of dissipation rate and that of the ocean stratification according to the finescale parameterization, decreases from $10^{-4} \text{ m}^2 \text{ s}^{-1}$ close to the seafloor to around $10^{-5} \text{ m}^2 \text{ s}^{-1}$ near the pycnocline with some elevation in between. The values of K_ρ in the Irminger Sea and East Basin basically decreases with the increase of height above seafloor, it varies between $O(10^{-4})$ and $O(10^{-5}) \text{ m}^2 \text{ s}^{-1}$. The dissipation rate in these two regions varies between $O(10^{-10})$ and $O(10^{-9}) \text{ W kg}^{-1}$.

5. DISCUSSION

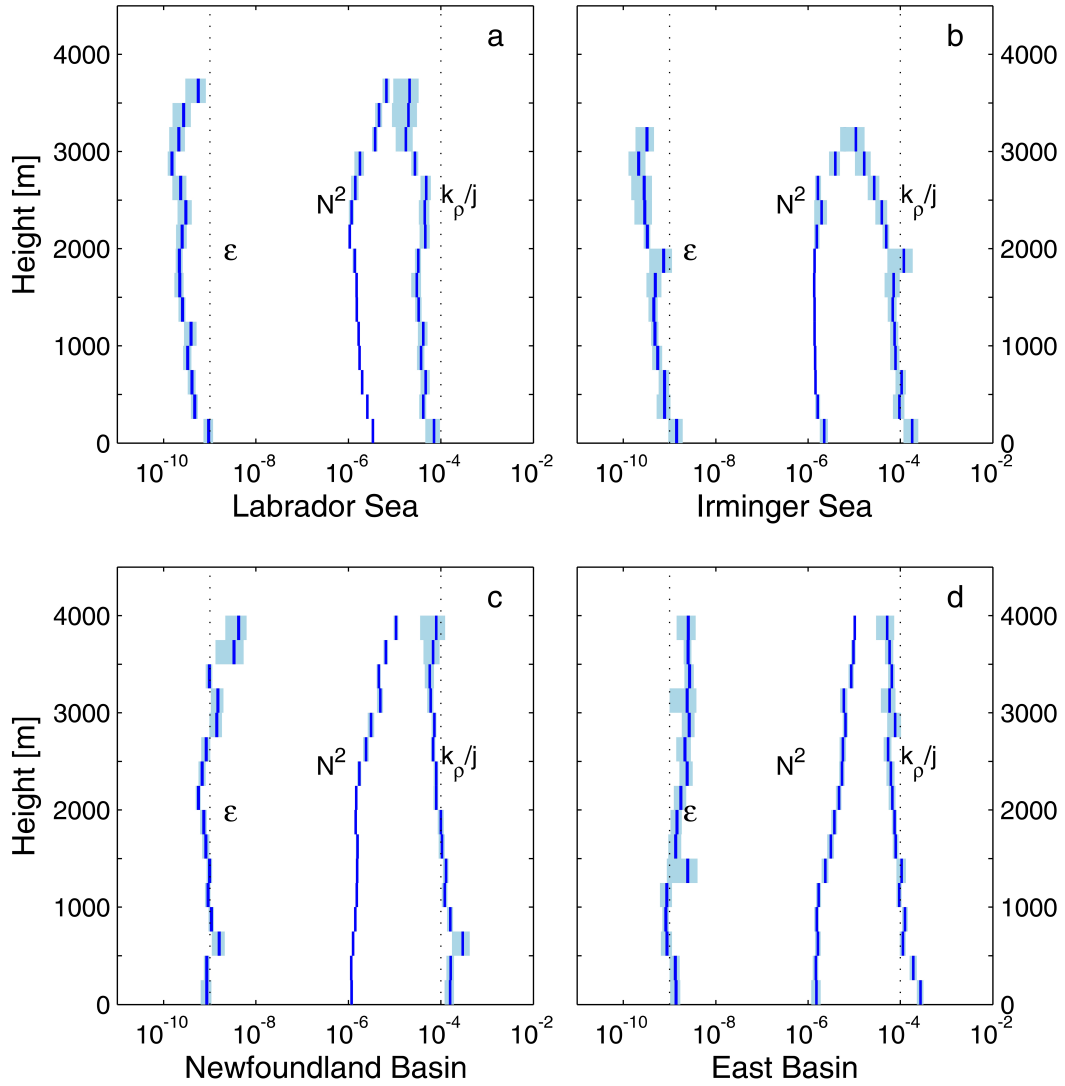


Figure 5.5: Vertical structure of diapycnal diffusivity, dissipation rate and buoyancy frequency in four regions. Blue shadings indicate the standard deviations computed using Bootstrap method.

The generation of turbulence and dissipation of energy in the Newfoundland Basin are influenced by the NAC and DWBC, thus the horizontal mean value of ε reaches its maximum in the surface layer near the pycnocline and is elevated several hundreds of meters above seafloor.

Moreover, the $1^\circ \times 1^\circ$ boxes with estimates are grouped into four classes with reference to the EKE and seafloor roughness (see Fig. 5.4), i.e., smooth

5. DISCUSSION

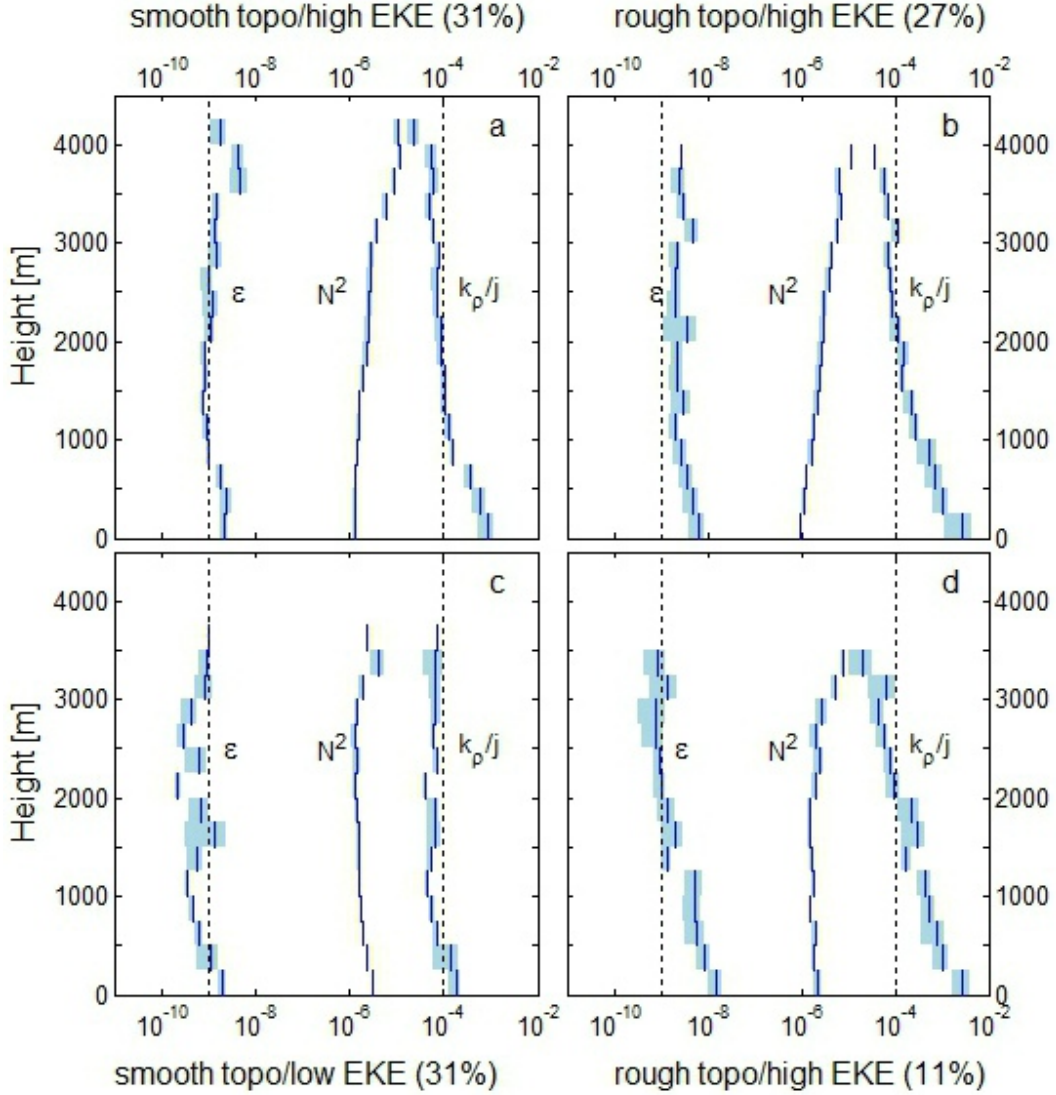


Figure 5.6: Similar to Fig. 5.5, but grouped according to strengths of seafloor roughness and eddy kinetic energy. Percentages indicate the proportion of each group to the total number of $1^\circ \times 1^\circ$ boxes.

topo/low EKE; smooth topo/high EKE; rough topo/low EKE and rough topo/high EKE. The boundaries of seafloor roughness and EKE are $r^2(H) = 6 \times 10^4 \text{ m}^2$ and $E_k = 5 \times 10^{-3} \text{ m}^2 \text{ s}^2$. Vertical structures of averaged K_ρ , ϵ and N^2 are displayed in Fig. 5.6. For the group of low EKE and low roughness (Fig. 5.6c), K_ρ does not vary much with height above seafloor; averaged values of all layers are in the magnitude of $10^{-4} \text{ m}^2 \text{ s}^{-1}$. For the group with equivalent roughness but high EKE (Fig. 5.6a), K_ρ close to seafloor increases with the

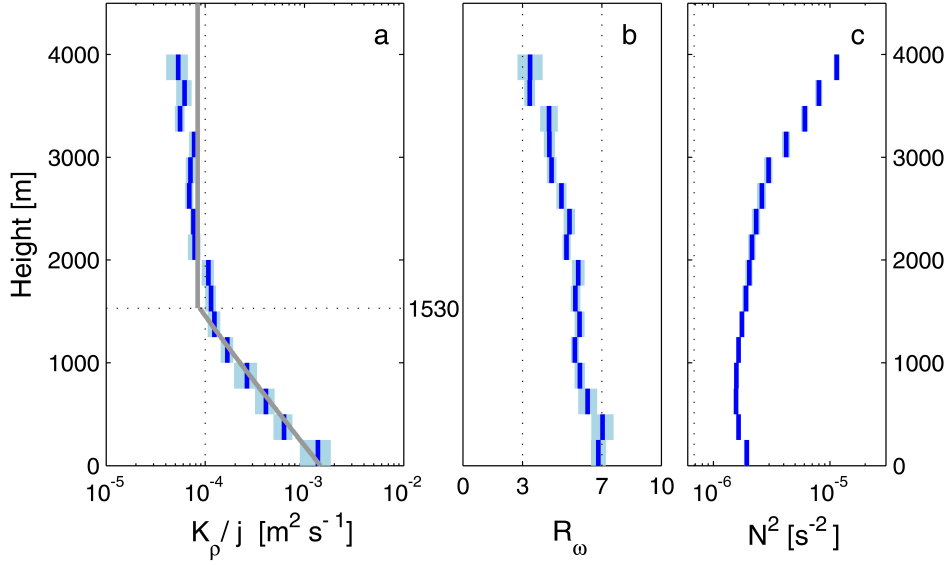


Figure 5.7: Vertical structures of diapycnal diffusivity, shear/strain variance ratio and buoyancy frequency in the whole SPNA.

decrease of distance, indicating that the surface originated meso-scale eddies indeed contribute to abyssal mixing. For groups with rough seafloor (Fig. 5.6b, d), averaged K_ρ in the lowest 250m exceed $10^{-3} \text{ m}^2 \text{ s}^{-1}$; but surface values with higher EKE are larger.

In the whole area of the subpolar North Atlantic, the shear/strain variance ratio R_ω decreases monotonically with the increase of height above the seafloor, with its averaged values of each 250m sub-layer varies between 3 and 7. The structure of K_ρ is more complicated: within about 1500 m above the seafloor, K_ρ decreases exponentially with h (the horizontal axes is in logarithm space), and then tends to be a constant in the upper. An empirical fit was made for the decay of K_ρ with h :

$$K_\rho = K_{00} + K_1 \frac{\exp(ah_0)}{\exp(ah)} \times j(f, N) \quad (5.3)$$

here $K_{00} = 5 \times 10^{-6} \text{ m}^2 \text{ s}^{-1}$ is the background diffusivity, $K_1 = 7.6 \times 10^{-5} \text{ m}^2 \text{ s}^{-1}$, $a = 1.9 \times 10^{-3}$, $h_0 = 1530 \text{ m}$ is the upper bound of the decay trend. The vertical decay scale for turbulence in the subpolar North Atlantic is larger than the range of between 300 and 1000 m proposed by St. Laurent *et al.* (2002),

5. DISCUSSION

due to the dissimilar topographic properties. Above 1530 m over seafloor, K_ρ tends to be a constant value of $(8.1 \pm 0.4) \times 10^{-5} \text{ m}^2 \text{ s}^{-1}$. The uncertainty here is the standard deviation calculated using Bootstrap method.

5.4 Transformation between water masses

The diapycnal mixing gives rise to transport of water across surfaces of equal density, associated with mixing between adjacent water masses comprising the North Atlantic Deep Water. Under the approximation of a vertical advection-diffusion balance model 2.9 (see section 2.2), vertical motion of water can be derived roughly through the estimates of vertical velocity of water:

$$w = K_\rho \frac{\rho_z}{\rho_{zz}}$$

where ρ_z and ρ_{zz} are the derivatives of potential density of the first and second orders. Vertical velocity of water w inferred from this model is always positive, indicating upwelling of water masses. If the area of interface between two adjacent water masses is multiplied with corresponding w , transformation rate between these two water masses can be derived. The SPNA was again gridded into $1^\circ \times 1^\circ$ boxes horizontally, density field and vertical motion on isopycnal surfaces were computed in each single box. Then the boxes were grouped into four regions for convenience (as shown by blue shadings in Fig. 3.2). In the observation blanks, density of seawater is referred from World Ocean Atlas 2009 datasets (WOA09), and w is set to be the mean in the region. The transformation rate R , or specifically, diapycnal volume flux across interface layer is derived:

$$R = \sum_{i=1}^n w \cdot a$$

here n is the number of boxes in the region and a denotes the area in each box. The transformation rates of LSW / GFZW (across isopycnal surface $\sigma_\theta = 27.80 \text{ kg m}^{-3}$) and GFZW / DSOW ($\sigma_\theta = 27.88$) in each region and the whole SPNA are listed in Table 5.1.

This estimate of transformation rate is a rough evaluation. The result is sensitive to the accuracies of the estimation of diffusivity and the density field, neither of which is fully determined. The transformation rate is somehow underestimated in the Labrador Sea due to the lack of observations in the predominant transformation region offshore from the flank of the deep Labrador

5. DISCUSSION

Table 5.1: Mean diffusivity, vertical velocity and water transformation rates of LSW / GFZW ($\sigma_\theta = 27.80 \text{ kg m}^{-3}$) and GFZW / DSOW ($\sigma_\theta = 27.88 \text{ kg m}^{-3}$) in various regions.

Area	σ_θ (kg m^{-3})	Mean K_ρ ($\times 10^{-4} \text{ m}^2 \text{ s}^{-1}$)	Mean w ($\times 10^{-7} \text{ m s}^{-1}$)	R (Sv)
Labrador Sea	27.80	1.6 ± 0.7	2.0 ± 0.8	0.21 ± 0.11
	27.88	2.1 ± 0.8	2.6 ± 1.1	0.39 ± 0.17
Irminger Sea	27.80	1.0 ± 0.2	1.4 ± 0.4	0.17 ± 0.04
	27.88	2.9 ± 1.6	5.8 ± 3.6	0.42 ± 0.17
Newfoundland Basin	27.80	1.4 ± 0.3	2.5 ± 0.5	0.44 ± 0.15
	27.88	3.4 ± 0.9	6.6 ± 1.7	1.03 ± 0.47
East Basin	27.80	1.5 ± 0.3	2.3 ± 0.6	0.74 ± 0.15
	27.88	3.6 ± 2.1	5.1 ± 3.0	1.64 ± 0.36
total	27.80	1.4 ± 0.2	2.2 ± 0.3	1.56 ± 0.45
	27.88	6.2 ± 3.7	5.0 ± 1.1	3.48 ± 1.17

Current. The resulting transformation rate between LSW and deep water is much smaller relative to the value of 0.7 Sv given by Brandt *et al.* (2007) from buoyancy loss with an eddy-resolving model. However, the net transformation from deep layer to LSW in the entire SPNA is larger than supposed by the work of Lumpkin *et al.* (2008), in which the transformation was evaluated to be opposite. The deep transformation is stronger due to the elevated mixing, almost triple of the values on the upper interface layer. It is comparable to the estimate of Lumpkin and Speer (2003) with a box inverse model, around 2.5 Sv, corresponding to the sum of transformation rate on interface between Lower Deep and Bottom layers in overflow and subpolar boxes in their work (Lumpkin and Speer, 2003, Fig. 4). A vertical flux of 1 – 3 Sv inner lower deep water was supposed by Lumpkin *et al.* (2008), slightly smaller than that between GFZW and DSOW estimated in this work.

Chapter 6

Summary and outlook

The diapycnal diffusivity K_ρ in the subpolar North Atlantic was estimated from a fine-scale parameterization with combined CTD/LADCP measurements carried out during 9 large hydrographic cruises from 2003 to 2011. Supposing the strength and structure do not vary temporally, K_ρ was mapped in the SPNA regions. An average value in the magnitude of $10^{-4} \text{ m}^2 \text{ s}^{-1}$ was derived, one order of magnitude larger than the background value in open ocean inferred by former studies using various methods. That means, the diffusivity in the SPNA is generally higher and diapycnal mixing is stronger than other ocean areas.

The general vertical structure of K_ρ was analysed in this work. Unlike the simple exponential-decay-upward structure that is widely used in model simulations, the vertical structure derived in this study is two fold: within the lowest 1500 m, K_ρ decays exponentially with height above seafloor; for upper layers K_ρ is constrained close to a constant around $(8.1 \pm 0.4) \times 10^{-4} \text{ m}^2 \text{ s}^{-1}$. Within around 320 m over the seafloor, diffusivity averaged into $1^\circ \times 1^\circ$ boxes spans 3 magnitudes; values larger than $10^{-4} \text{ m}^2 \text{ s}^{-1}$ are found nearly everywhere in the SPNA. The topography in this area is generally rough, relatively smooth seafloor exists only in the Labrador Sea, where the bottom diffusivities at some boxes are in the magnitude of $O(10^{-5} \text{ m}^2 \text{ s}^{-1})$. The enhanced mixing close to the seafloor is basically due to the interactions of tidal flow or geostrophic currents with the sharply varied topography. Internal tides and lee waves are generated in this process, and tend to dissipate locally. Energy

6. SUMMARY AND OUTLOOK

is transferred from low wavenumber regime to high wavenumber bands, supporting the turbulence and resulting mixing. A correlation between seafloor roughness and the strength of bottom diffusivity was studied, and a dependence of diffusivity on the roughness was testified again by this study: the more the topography varies, the higher the diffusivity.

In mid-depth layers, K_ρ varies from place to place. High values are mainly at several locations: south of Greenland, at western boundary region (east of Grand Banks), over Mid-Atlantic Ridge, and some places in the Newfoundland Basin. Along the center of MAR, the thickness of the layer with $K_\rho > 10^{-4} \text{ m}^2 \text{ s}^{-1}$ could reach 1000 - 2000 m, including the whole water column at places, such as at 48°N. In the energetic western boundary region, high values exceeding $10^{-3} \text{ m}^2 \text{ s}^{-1}$ are found over the whole water column at the continental slope. The intensive mixing is probably due to the intensified interaction of the current with bottom topography. Moreover, highly elevated diffusivity is found to be consistent with the pathway of deep currents, such as the East Greenland Current to the southwest of Greenland, along the deep Labrador Current north of Grand Banks. The mixing in the Labrador Sea is relatively weaker, mainly in the magnitude of $10^{-5} \text{ m}^2 \text{ s}^{-1}$.

Dissipation in the SPNA was integrated over the water column, and a great consistency was found between the strengths of integrated dissipation and eddy kinetic energy. It suggests that intensive meso-scale eddies may be another supplier of energy for dissipation and turbulent diffusivity.

Furthermore, an approximate estimation of the net transformation rates between adjacent components of NADW was made using the vertical advection - diffusion balance model. The values of 1.6 Sv and 3.5 Sv were derived respectively for the conversions between Labrador Sea Water / Gibbs Fracture Zone Water / Denmark Strait Overflow Water in the entire subpolar North Atlantic. The former rate is larger than the transformation inferred by earlier studies, and the latter is slightly smaller. The utilisation of fine-scale measurements to deduce transformations among water masses provide a supplement other than the buoyancy-loss method, but requires high accuracy of density

field, and more CTD/LADCP measurements.

While the profiles presented in this study can present the main distribution and vertical structure of the turbulent mixing in the subpolar North Atlantic, plenty of blanks still exist over the Reykjavik Ridge, near the boundary of the Eastern Atlantic and southeast of Grand Banks in Newfoundland Basin. More widespread ARGO float with continuous CTD records can fill the gaps to some extent, but the measurements are confined within the upper layer (around 2000 m) and relies solely on the density field. More and thorough hydrographic surveys are in the pipeline, more detailed distribution in the subpolar North Atlantic is expected in the near future.

The applicability of the fine structure parameterization was examined through the comparison to microstructure measurements. The microscale profiles provide a direct measurement of dissipation, but the simultaneous measurements to that of CTD/LADCP were quite rare. The existing MSS profiles are concentrated to the west of MAR near the Charlie-Gibbs fracture zone and Faraday fracture zone, and off Flemish Cap. Both locations are characterized by sharp topography or intensified flows, connected to strong mixing and elevated dissipation. More microstructure measurements are still needed at locations with universality. Moreover, comparison with the strain-based parameterization may be another way to quantify the parameterization used in this work.

Bibliography

- [1] M. H. Alford. Internal Swell Generation: The Spatial Distribution of Energy Flux from the Wind to Mixed Layer Near-Inertial Motions. *Journal of Physical Oceanography*, 31(8):2359–2368, Aug. 2001.
- [2] A. S. Bower, M. S. Lozier, S. F. Gary, and C. W. Böning. Interior pathways of the North Atlantic meridional overturning circulation. *Nature*, 459(7244):243–7, May 2009.
- [3] P. Brandt, A. Funk, L. Czeschel, C. Eden, and C. W. Böning. Ventilation and Transformation of Labrador Sea Water and Its Rapid Export in the Deep Labrador Current. *Journal of Physical Oceanography*, 37(4):946–961, Apr. 2007.
- [4] M. G. Briscoe. Preliminary results from the trimoored internal wave experiment (IWEX). *Journal of Geophysical Research*, 80(27):3872–3884, Sept. 1975.
- [5] E. D. Brown and W. B. Owens. Observations of the Horizontal Interactions between the Internal Wave Field and the Mesoscale Flow. *Journal of Physical Oceanography*, 11(11):1474–1480, Nov. 1981.
- [6] F. Bryan. Parameter Sensitivity of Primitive Equation Ocean General Circulation Models. *Journal of Physical Oceanography*, 17(7):970–985, July 1987.
- [7] T. Decloedt and D. S. Luther. On a Simple Empirical Parameterization of Topography-Catalyzed Diapycnal Mixing in the Abyssal Ocean. *Journal of Physical Oceanography*, 40(3):487–508, Mar. 2010.

BIBLIOGRAPHY

- [8] R. R. Dickson and J. Brown. The production of North Atlantic Deep Water: Sources, rates, and pathways. *Journal of Geophysical Research*, 99(C6):12319, 1994.
- [9] R. Ferrari and C. Wunsch. Ocean Circulation Kinetic Energy: Reservoirs, Sources, and Sinks. *Annual Review of Fluid Mechanics*, 41(1):253–282, Jan. 2009.
- [10] J. Fischer and M. Visbeck. Deep Velocity Profiling with Self-contained ADCPs. *Journal of Atmospheric and Oceanic Technology*, 10(5):764–773, Oct. 1993.
- [11] N. Fofonoff. Spectral characteristics of internal waves in the ocean. *Deep sea research*, 16:58–71, 1969.
- [12] A. E. Gargett. The scaling of turbulence in the presence of stable stratification. *Journal of Geophysical Research*, 93(C5):5021, 1988.
- [13] A. E. Gargett. Do we really know how to scale the turbulent kinetic energy dissipation rate ϵ due to breaking of oceanic internal waves? *Journal of Geophysical Research*, 95(C9):15971–15974, 1990.
- [14] C. Garrett. Oceanography: Mixing with latitude. *Nature*, 422(6931):477–478, Apr. 2003.
- [15] C. Garrett and F. Gerdes. Hydraulic control of homogeneous shear flows. *Journal of Fluid Mechanics*, 475:163–172, Feb. 2003.
- [16] C. Garrett and E. Kunze. Internal Tide Generation in the Deep Ocean. *Annual Review of Fluid Mechanics*, 39(1):57–87, Jan. 2007.
- [17] C. Garrett and L. Laurent. Aspects of deep ocean mixing. *Journal of oceanography*, 58(1):11–24, 2002.
- [18] C. Garrett and W. Munk. Space-Time scales of internal waves. *Geophysical Fluid Dynamics*, 3(1):225–264, Jan. 1972.
- [19] C. Garrett and W. Munk. Space-time scales of internal waves: A progress report. *Journal of Geophysical Research*, 80(3):291–297, Jan. 1975.

BIBLIOGRAPHY

- [20] C. Garrett and W. Munk. Internal Waves in the Ocean. *Annual Review of Fluid Mechanics*, 11(1):339–369, Jan. 1979.
- [21] T. Gerkema and J. Zimmerman. *An introduction to internal waves*. Lecture notes, Royal Nioz, Texel, 2008.
- [22] S. T. Gille, M. M. Yale, and D. T. Sandwell. Global correlation of mesoscale ocean variability with seafloor roughness from satellite altimetry. *Geophysical Research Letters*, 27(9):1251–1254, 2000.
- [23] A. Gnanadesikan. A simple predictive model for the structure of the oceanic pycnocline. *Science (New York, N.Y.)*, 283(5410):2077–2079, Mar. 1999.
- [24] A. Gordon. The role of thermohaline circulation in global climate change. Technical Report 914, 1991.
- [25] M. C. Gregg. Diapycnal mixing in the thermocline: A review. *Journal of Geophysical Research*, 92(C5):5249–5286, 1987.
- [26] M. C. Gregg. Scaling turbulent dissipation in the thermocline. *Journal of Geophysical Research*, 94(C7):9686–9698, 1989.
- [27] M. C. Gregg and E. Kunze. Shear and strain in Santa Monica Basin. *Journal of Geophysical Research*, 96(C9):16709–16719, 1991.
- [28] M. C. Gregg, T. B. Sanford, and D. P. Winkel. Reduced mixing from the breaking of internal waves in equatorial waters. *Nature*, 422(6931):513–515, Apr. 2003.
- [29] T. Hibiya and M. Nagasawa. Latitudinal dependence of diapycnal diffusivity in the thermocline estimated using a finescale parameterization. *Geophysical Research Letters*, 31(1):L01301, 2004.
- [30] T. Hibiya, M. Nagasawa, and Y. Niwa. Latitudinal dependence of diapycnal diffusivity in the thermocline observed using a microstructure profiler. *Geophysical Research Letters*, 34(24):L24602, Dec. 2007.

BIBLIOGRAPHY

- [31] R. Hummels, M. Dengler, and B. Bourlès. Seasonal and regional variability of upper ocean diapycnal heat flux in the Atlantic cold tongue. *Progress in Oceanography*, 111:52–74, Apr. 2013.
- [32] G. Ivey, K. Winters, and J. Koseff. Density Stratification, Turbulence, but How Much Mixing? *Annual Review of Fluid Mechanics*, 40(1):169–184, Jan. 2008.
- [33] S. R. Jayne. The Impact of Abyssal Mixing Parameterizations in an Ocean General Circulation Model. *Journal of Physical Oceanography*, 39(7):1756–1775, July 2009.
- [34] D. Kieke, M. Rhein, L. Stramma, W. M. Smethie, J. L. Bullister, and D. a. LeBel. Changes in the pool of Labrador Sea Water in the subpolar North Atlantic. *Geophysical Research Letters*, 34(6):L06605, Mar. 2007.
- [35] D. Kieke, M. Rhein, L. Stramma, W. M. Smethie, D. a. LeBel, and W. Zenk. Changes in the CFC Inventories and Formation Rates of Upper Labrador Sea Water, 19972001. *Journal of Physical Oceanography*, 36(1):64–86, Jan. 2006.
- [36] H. Ku. Notes on the use of propagation of error formulas. *Journal of Research of the National Bureau of Standards-C. Engineering and Instrumentation*, 70C(4):75–79, 1966.
- [37] T. Kuhlbrodt, A. Griesel, M. Montoya, A. Levermann, M. Hofmann, and S. Rahmstorf. On the driving processes of the Atlantic meridional overturning circulation. *Reviews of Geophysics*, 45(2):RG2001, Apr. 2007.
- [38] E. Kunze, M. G. Briscoe, and A. J. Williams III. Interpreting Shear and Strain Fine Structure From a Neutrally Buoyant Float. *Journal of Geophysical Research*, 95(C10):18111–18125, 1990.
- [39] E. Kunze, E. Firing, J. M. Hummon, T. K. Chereskin, and A. M. Thurnherr. Global Abyssal Mixing Inferred from Lowered ADCP Shear and CTD Strain Profiles. *Journal of Physical Oceanography*, 36(8):1553–1576, Aug. 2006.

BIBLIOGRAPHY

- [40] E. Kunze, L. K. Rosenfeld, G. S. Carter, and M. C. Gregg. Internal Waves in Monterey Submarine Canyon. *Journal of Physical Oceanography*, 32(6):1890–1913, June 2002.
- [41] E. Kunze and T. B. Sanford. Abyssal Mixing: Where It Is Not. *Journal of Physical Oceanography*, 26(10):2286–2296, Oct. 1996.
- [42] E. Kunze and J. M. Toole. Tidally Driven Vorticity, Diurnal Shear, and Turbulence atop Fieberling Seamount. *Journal of Physical Oceanography*, 27(12):2663–2693, Dec. 1997.
- [43] J. Lauderdale and S. Bacon. Intensified turbulent mixing in the boundary current system of southern Greenland. *Geophys. Res. . . .*, 35:1–6, 2008.
- [44] J. Ledwell, E. Montgomery, K. Polzin, St. Laurent LC, R. Schmitt, and J. Toole. Evidence for enhanced mixing over rough topography in the abyssal ocean. *Nature*, 403(6766):179–182, Jan. 2000.
- [45] J. R. Ledwell, A. J. Watson, and C. S. Law. Evidence for slow mixing across the pycnocline from an open-ocean tracer-release experiment. *Nature*, 364(6439):701–703, Aug. 1993.
- [46] R. Lumpkin and K. Speer. Large-Scale Vertical and Horizontal Circulation in the North Atlantic Ocean. *Journal of Physical Oceanography*, 33(9):1902–1920, Sept. 2003.
- [47] R. Lumpkin, K. G. Speer, and K. P. Koltermann. Transport across 48N in the Atlantic Ocean. *Journal of Physical Oceanography*, 38(4):733–752, Apr. 2008.
- [48] J. MacKinnon. Using Global Arrays to Investigate Internal-Waves and Mixing. In *Proceedings of OceanObs’09: Sustained Ocean Observations and Information for Society*, volume 2, pages 627–637. European Space Agency, Dec. 2010.
- [49] C. Mann. The termination of the Gulf Stream and the beginning of the North Atlantic Current. *Deep Sea Research and Oceanographic Abstracts*, 14(3):337–359, June 1967.

BIBLIOGRAPHY

- [50] J. Marotzke. Boundary Mixing and the Dynamics of Three-Dimensional Thermohaline Circulations. *Journal of Physical Oceanography*, 27(8):1713–1728, Aug. 1997.
- [51] J. Marshall, H. Jones, R. Karsten, and R. Wardle. Can Eddies Set Ocean Stratification? *Journal of Physical Oceanography*, 32(1):26–38, Jan. 2002.
- [52] C. H. McComas. Equilibrium Mechanisms within the Oceanic Internal Wave Field. *Journal of Physical Oceanography*, 7(6):836–845, Nov. 1977.
- [53] C. H. McComas and F. P. Bretherton. Resonant interaction of oceanic internal waves. *Journal of Geophysical Research*, 82(9):1397–1412, 1977.
- [54] C. H. McComas and P. Müller. The Dynamic Balance of Internal Waves. *Journal of Physical Oceanography*, 11(7):970–986, July 1981.
- [55] C. H. McComas and P. Müller. Time Scales of Resonant Interactions Among Oceanic Internal Waves. *Journal of Physical Oceanography*, 11(2):139–147, Feb. 1981.
- [56] J. N. Moum and T. R. Osborn. Mixing in the Main Thermocline. *Journal of Physical Oceanography*, 16(7):1250–1259, July 1986.
- [57] P. Müller, G. Holloway, F. Henyey, and N. Pomphrey. Nonlinear interactions among internal gravity waves. *Reviews of Geophysics*, 24(3):493–536, 1986.
- [58] W. Munk. Internal waves and small-scale processes. In *Evolution of physical oceanography*, chapter part 2, ch, pages 264–290. The MIT Press, 264290., 1981.
- [59] W. Munk and C. Wunsch. Abyssal recipes 2-energetics of tidal and wind mixing. *Deep Sea Research Part I: Oceanographic Research Papers*, 45(12):1977–2010, 1998.
- [60] W. H. Munk. Abyssal recipes. *Deep Sea Research and Oceanographic Abstracts*, 13(4):707–730, Aug. 1966.

BIBLIOGRAPHY

- [61] J. D. Nash, M. H. Alford, E. Kunze, K. Martini, and S. Kelly. Hotspots of deep ocean mixing on the Oregon continental slope. *Geophysical Research Letters*, 34(1):L01605, Jan. 2007.
- [62] M. Nikurashin and R. Ferrari. Radiation and Dissipation of Internal Waves Generated by Geostrophic Motions Impinging on Small-Scale Topography: Theory. *Journal of Physical Oceanography*, 40(5):1055–1074, May 2010a.
- [63] M. Nikurashin and R. Ferrari. Radiation and Dissipation of Internal Waves Generated by Geostrophic Motions Impinging on Small-Scale Topography: Application to the Southern Ocean. *Journal of Physical Oceanography*, 40(9):2025–2042, Sept. 2010b.
- [64] T. R. Osborn. Estimates of the Local Rate of Vertical Diffusion from Dissipation Measurements. *Journal of Physical Oceanography*, 10(1):83–89, Jan. 1980.
- [65] T. R. Osborn and C. S. Cox. Oceanic fine structure. *Geophysical Fluid Dynamics*, 3(1):321–345, Jan. 1972.
- [66] J. Pedlosky. *Ocean Circulation theory*. Springer-Verlag, 1996.
- [67] J. L. Pelegrí and G. T. Csanady. Diapycnal mixing in western boundary currents. *Journal of Geophysical Research*, 99(C9):18275–18304, 1994.
- [68] P. Physics, U. Kingdom, and N. O. Centre. A Conjecture on the Role of Bottom-Enhanced Diapycnal Mixing in the. pages 1607–1613, 2008.
- [69] R. S. Pickart, N. G. Hogg, and W. M. Smethie. Determining the Strength of the Deep Western Boundary Current Using the Chlorofluoromethane Ratio. *Journal of Physical Oceanography*, 19(7):940–951, July 1989.
- [70] K. Polzin, E. Kunze, J. Hummon, and E. Firing. The Finescale Response of Lowered ADCP Velocity Profiles. *Journal of Atmospheric and Oceanic Technology*, 19(2):205–224, Feb. 2002.

BIBLIOGRAPHY

- [71] K. L. Polzin. Mesoscale EddyInternal Wave Coupling. Part I: Symmetry, Wave Capture, and Results from the Mid-Ocean Dynamics Experiment. *Journal of Physical Oceanography*, 38(11):2556–2574, Nov. 2008.
- [72] K. L. Polzin, J. M. Toole, J. R. Ledwell, and R. W. Schmitt. Spatial Variability of Turbulent Mixing in the Abyssal Ocean. *Science*, 276(5309):93–96, Apr. 1997.
- [73] K. L. Polzin, J. M. Toole, and R. W. Schmitt. Finescale Parameterizations of Turbulent Dissipation. *Journal of Physical Oceanography*, 25(3):306–328, Mar. 1995.
- [74] H. Prandke and A. Stips. Test measurements with an operational microstructure-turbulence profiler: Detection limit of dissipation rates. *Aquatic Sciences*, 60(3):191–209, 1998.
- [75] M. Prange, G. Lohmann, and A. Paul. Influence of Vertical Mixing on the Thermohaline Hysteresis: Analyses of an OGCM. *Journal of Physical Oceanography*, 33(8):1707–1721, Aug. 2003.
- [76] C. R. Rehmann and J. R. Koseff. Mean potential energy change in stratified grid turbulence. *Dynamics of Atmospheres and Oceans*, 37(4):271–294, May 2004.
- [77] T. H. Reynaud, A. J. Weaver, and R. J. Greatbatch. Summer mean circulation of the northwestern Atlantic Ocean. *Journal of Geophysical Research*, 100(C1):779, 1995.
- [78] M. Rhein. Short cruise report RV MERIAN : cruise MSM09-1. Technical report, 2008.
- [79] M. Rhein, J. Fischer, W. M. Smethie, D. Smythe-Wright, R. F. Weiss, C. Mertens, D.-H. Min, U. Fleischmann, and A. Putzka. Labrador Sea Water: Pathways, CFC Inventory, and Formation Rates. *Journal of Physical Oceanography*, 32(2):648–665, Feb. 2002.
- [80] M. Rhein, D. Kieke, H. Sabine, A. Roessler, C. Mertens, I. Yashayaev, R. Meissner, B. Klein, W. B. Claus, S. Hüttl-Kabus, and C. W. Böning.

BIBLIOGRAPHY

- Deep water formation, the subpolar gyre, and the meridional overturning circulation in the subpolar North Atlantic. *Deep Sea Research Part II: Topical Studies in Oceanography*, 58(17-18):1819–1832, Sept. 2011.
- [81] T. Rossby. The North Atlantic Current and surrounding waters: At the crossroads. *Reviews of Geophysics*, 34(4):463–481, 1996.
- [82] O. A. Saenko. The Effect of Localized Mixing on the Ocean Circulation and Time-Dependent Climate Change. *Journal of Physical Oceanography*, 36(1):140–160, Jan. 2006.
- [83] O. A. Saenko and W. J. Merryfield. On the Effect of Topographically Enhanced Mixing on the Global Ocean Circulation. *Journal of Physical Oceanography*, 35(5):826–834, May 2005.
- [84] O. a. Saenko, X. Zhai, W. J. Merryfield, and W. G. Lee. The Combined Effect of Tidally and Eddy-Driven Diapycnal Mixing on the Large-Scale Ocean Circulation. *Journal of Physical Oceanography*, 42(4):526–538, Apr. 2012.
- [85] J. Schafstall, M. Dengler, P. Brandt, and H. Bange. Tidal-induced mixing and diapycnal nutrient fluxes in the Mauritanian upwelling region. *Journal of Geophysical Research*, 115(C10):C10014, Oct. 2010.
- [86] F. A. Schott, R. Zantopp, L. Stramma, M. Dengler, J. Fischer, and M. Wibaux. Circulation and Deep-Water Export at the Western Exit of the Subpolar North Atlantic. *Journal of Physical Oceanography*, 34(4):817–843, Apr. 2004.
- [87] L. H. Shih, J. R. Koseff, G. N. Ivey, and J. H. Ferziger. Parameterization of turbulent fluxes and scales using homogeneous sheared stably stratified turbulence simulations. *Journal of Fluid Mechanics*, 525(August 2004):193–214, Feb. 2005.
- [88] H. L. Simmons, S. R. Jayne, L. C. St. Laurent, and A. J. Weaver. Tidally driven mixing in a numerical model of the ocean general circulation. *Ocean Modelling*, 6(3-4):245–263, Jan. 2004.

BIBLIOGRAPHY

- [89] K. Speer, S. R. Rintoul, and B. Sloyan. The Diabatic Deacon Cell*. *Journal of Physical Oceanography*, 30(12):3212–3222, Dec. 2000.
- [90] L. St. Laurent and C. Garrett. The Role of Internal Tides in Mixing the Deep Ocean. *Journal of Physical Oceanography*, 32(10):2882–2899, Oct. 2002.
- [91] L. C. St. Laurent, J. M. Toole, and R. W. Schmitt. Buoyancy Forcing by Turbulence above Rough Topography in the Abyssal Brazil Basin*. *Journal of Physical Oceanography*, 31(12):3476–3495, Dec. 2001.
- [92] U. Stöber. *mixing and energy flux estimates from hydrographic measurements in the deep western boundary current of the north atlantic*. PhD thesis, 2009.
- [93] U. Stöber, M. Walter, C. Mertens, and M. Rhein. Mixing estimates from hydrographic measurements in the Deep Western Boundary Current of the North Atlantic. *Deep Sea Research Part I: Oceanographic Research Papers*, 55(6):721–736, June 2008.
- [94] H. Stommel. A survey of ocean current theory. *Deep Sea Research (1953)*, 4(January):149–184, Jan. 1957.
- [95] H. Stommel. The abyssal circulation. *Deep Sea Research (1953)*, 5(1):80–82, Jan. 1958.
- [96] H. Stommel and A. Arons. On the abyssal circulation of the world ocean II. An idealized model of the circulation pattern and amplitude in oceanic basins. *Deep Sea Research (1953)*, 6(August):217–233, Jan. 1960.
- [97] H. Stommel and A. Arons. On the abyssal circulation of the world ocean I. Stationary planetary flow patterns on a sphere. *Deep Sea Research (1953)*, 6(February):140–154, Jan. 1960.
- [98] H. Stommel, A. B. Arons, and A. J. Faller. Some Examples of Stationary Planetary Flow Patterns in Bounded Basins. *Tellus*, 10(2):179–187, May 1958.

BIBLIOGRAPHY

- [99] L. Stramma, D. Kieke, M. Rhein, F. Schott, I. Yashayaev, and K. P. Koltermann. Deep water changes at the western boundary of the sub-polar North Atlantic during 1996 to 2001. *Deep Sea Research Part I: Oceanographic Research Papers*, 51(8):1033–1056, Aug. 2004.
- [100] H. Sun and E. Kunze. Internal Wave-Wave Interactions. Part I: The Role of Internal Wave Vertical Divergence. *Journal of Physical Oceanography*, 29(11):2886–2904, Nov. 1999.
- [101] S. Sun and R. Bleck. Thermohaline Circulation Studies with an Isopycnic Coordinate Ocean Model. *Journal of Physical Oceanography*, 31(9):2761–2782, Sept. 2001.
- [102] L. D. Talley and M. S. McCartney. Distribution and Circulation of Labrador Sea Water. *Journal of Physical Oceanography*, 12(11):1189–1205, Nov. 1982.
- [103] A. M. Thurnherr. The Finescale Response of Lowered ADCP Velocity Measurements Processed with Different Methods. *Journal of Atmospheric and Oceanic Technology*, 29(4):597–600, Apr. 2012.
- [104] J. M. Toole, R. W. Schmitt, and K. L. Polzin. Estimates of diapycnal mixing in the abyssal ocean. *Science (New York, N.Y.)*, 264(5162):1120–1123, May 1994.
- [105] H. M. van Aken, H. van Haren, and L. R. Maas. The high-resolution vertical structure of internal tides and near-inertial waves measured with an ADCP over the continental slope in the Bay of Biscay. *Deep Sea Research Part I: Oceanographic Research Papers*, 54(4):533–556, Apr. 2007.
- [106] M. Visbeck. Deep Velocity Profiling Using Lowered Acoustic Doppler Current Profilers: Bottom Track and Inverse Solutions*. *Journal of Atmospheric and Oceanic Technology*, 19(5):794–807, May 2002.
- [107] M. Walter, C. Mertens, and M. Rhein. Mixing estimates from a large-scale hydrographic survey in the North Atlantic. *Geophysical Research Letters*, 32(13):L13605, 2005.

BIBLIOGRAPHY

- [108] C. B. Whalen, L. D. Talley, and J. a. MacKinnon. Spatial and temporal variability of global ocean mixing inferred from Argo profiles. *Geophysical Research Letters*, 39(18):L18612, Sept. 2012.
- [109] F. Wolk, H. Yamazaki, L. Seuront, and R. G. Lueck. A New Free-Fall Profiler for Measuring Biophysical Microstructure. *Journal of Atmospheric and Oceanic Technology*, 19(5):780–793, May 2002.
- [110] L. Wu, Z. Jing, S. Riser, and M. Visbeck. Seasonal and spatial variations of Southern Ocean diapycnal mixing from Argo profiling floats. *Nature Geoscience*, 4(6):363–366, May 2011.
- [111] C. Wunsch. Oceanography. What is the thermohaline circulation? *Science (New York, N.Y.)*, 298(5596):1179–1181, Nov. 2002.
- [112] C. Wunsch and R. Ferrari. Vertical mixing, energy, and the general circulation of the oceans. *Annual Review of Fluid Mechanics*, 36(1):281–314, Jan. 2004.
- [113] K. Wyrтки. The oxygen minima in relation to ocean circulation. *Deep Sea Research and Oceanographic Abstracts*, 9(1-2):11–23, Jan. 1962.
- [114] X. Zhai, H. L. Johnson, and D. P. Marshall. Significant sink of ocean-eddy energy near western boundaries. *Nature Geoscience*, 3(9):608–612, Aug. 2010.

Acknowledgements

In the very last days of my PhD project, I would like to express my sincere gratitude to:

my supervisor, Prof. Dr. Monika Rhein, who accepted me as a PhD-student and is always nice to me, although I was really in a mess at times;

my mentors, Maren Walter and Christian Mertens, who provided me unre-served help throughout the entire PhD project; they had hard jobs themselves, but they were always patient and attentive, always ready for help ;

Prof. Dr. Richard Greatbatch from GEOMAR, Kiel; as a member of my thesis committee meeting and reviewer of this thesis, he helped me a lot in academics and writing;

Dr. Marcus Dengler from GEOMAR, Kiel, for his help in dealing with Microscale Structure measurements and useful suggestions for data processing;

my dear colleagues at the Department of Oceanography; the atmosphere in this group is always so nice, positive and active. Special thanks to Uwe Stöber for the guide in data processing; Achim Roessler, who picked me up when I arrived for the first time and I always remember the comfort from him when I was down to the trough;

China Scholarship Council (CSC), for the financial support for the work and living in Germany;

BIBLIOGRAPHY

Bremen International Graduate School for Marine Sciences (GLOMAR), for the multitudinous interesting and useful courses, workshops from which I have learned a lot, and the support to participate in international conferences;

my dear friends, for their never ending patience, kindness and support, especially Nicole, Charlie, Yi, Yuting, Yufang, Rong; I enjoy the good times with you, and it was so nice to have you;

finally, and most importantly, my parents; they encourage me all the time and gave me these wings to fly; I love you.